12-2016

Synthesis, design, and fabrication techniques for reconfigurable microwave and millimeter-wave filters

Mark D. Hickle
Purdue University

PURDUE UNIVERSITY
GRADUATE SCHOOL
Thesis/Dissertation Acceptance

This is to certify that the thesis/dissertation prepared

By Mark Hickle

Entitled

Synthesis, Design, and Fabrication Techniques for Reconfigurable Microwave and Millimeter-Wave Filters

For the degree of Doctor of Philosophy

Is approved by the final examining committee:

Dimitrios Peroulis
Chair

Dan Jiao

Saeed Mohammadi

Byunghoo Jung

To the best of my knowledge and as understood by the student in the Thesis/Dissertation Agreement, Publication Delay, and Certification Disclaimer (Graduate School Form 32), this thesis/dissertation adheres to the provisions of Purdue University's "Policy of Integrity in Research" and the use of copyright material.

Approved by Major Professor(s): Dimitrios Peroulis

Approved by: Venkataramanan Balakrishnan 11/30/2016

Head of the Departmental Graduate Program Date

SYNTHESIS, DESIGN, AND FABRICATION TECHNIQUES FOR RECONFIGURABLE MICROWAVE AND MILLIMETER-WAVE FILTERS

A Dissertation

Submitted to the Faculty
of
Purdue University
by
Mark D. Hickle

In Partial Fulfillment of the
Requirements for the Degree
of
Doctor of Philosophy

December 2016

Purdue University
West Lafayette, Indiana

TABLE OF CONTENTS

LIST OF TABLES

LIST OF FIGURES

Figure Page

Figure Page

Figure Page

Figure Page

Figure Page

Figure Page

Figure Page

Figure Page

ABSTRACT

Hickle, Mark D. Ph.D., Purdue University, December 2016. Synthesis, Design, and Fabrication Techniques for Reconfigurable Microwave and Millimeter-Wave Filters. Major Professor: Dimitrios Peroulis.

As wireless communication becomes increasingly ubiquitous, the need for radio receivers which can dynamically adjust to their operating environment grows more urgent. In order to realize reconfigurable receivers, tunable RF front-end components are needed. This dissertation focuses on the theory, design, and implementation of reconfigurable microwave and millimeter-wave filters for use in such receivers.

First, a theoretical framework is developed for absorptive bandstop filters, a new class of bandstop filters which overcomes some of the limitations of traditional tunable bandstop filters caused by the use of lossy tunable resonators. This theory is used in conjunction with silicon-micromachining fabrication technology to realize the first ever tunable bandstop filter at W-Band frequencies, as well as a state-of-the-art Ka-band tunable bandstop filter.

The problem of bandwidth variation in tunable filters is then addressed. Widely-tunable filters often suffer from variations in bandwidth, excluding them from many applications which require constant bandwidth. A new method for reducing the bandwidth variation of filters using low-loss evanescent-mode cavity resonators is presented, and this technique is used to realize up to 90% reduction of bandwidth variation in octave-tunable bandstop filters.

Lastly, a new differential coupling structure for evanescent-mode cavity resonators is developed, enabling the design of fully-balanced and balanced-to-unbalanced (balun) filters. An octave-tunable 3-pole bandpass balun filter using this coupling structure is presented. The balun filter has excellent amplitude and phase balance, resulting in common-mode rejection of greater than 40 dB across its octave tuning range.

1. INTRODUCTION

1.1 Motivation

Why do we need reconfigurable microwave filters? This is an important question which must be answered before embarking on a journey of research and discovery into tunable filters. After all, microwave engineers have been designing communication systems for a number of decades using static filters with good success, and tunable filters tend to have worse performance than their static counterparts while being much more complex and expensive. There are many ways to answer this question, but all center around two facts: the number of devices in the world which communicate wirelessly is increasing at an unprecedented rate, and the usable radio spectrum is a fixed and limited natural resource. These facts have driven the development of software-defined and cognitive radios, which use software to implement many traditionally-hardware blocks such as mixers, filters, and demodulators, and can dynamically adjust their operating parameters such as center frequency, bandwidth, modulation type, etc. to optimally use the available radio spectrum.

The simplest practical architecture for a software-defined or cognitive radio is shown in Fig. 1.1(a), in which signals from the antenna are amplified by a wideband low-noise amplifier (LNA), down-converted by a mixer (though even this step is optional if high-frequency analog-to-digital converters (ADCs) are available at the RF frequency), then digitized for channel selection and demodulation. A receiver architecture such as this allows large amounts of flexibility as it can operate on numerous frequencies, limited only by the bandwidths of the antenna, LNA, mixer, and ADC, which are generally very wideband when compared to the RF preselect filters which most receivers use. This leaves the receiver vulnerable to jamming signals which can cause the LNA to saturate,

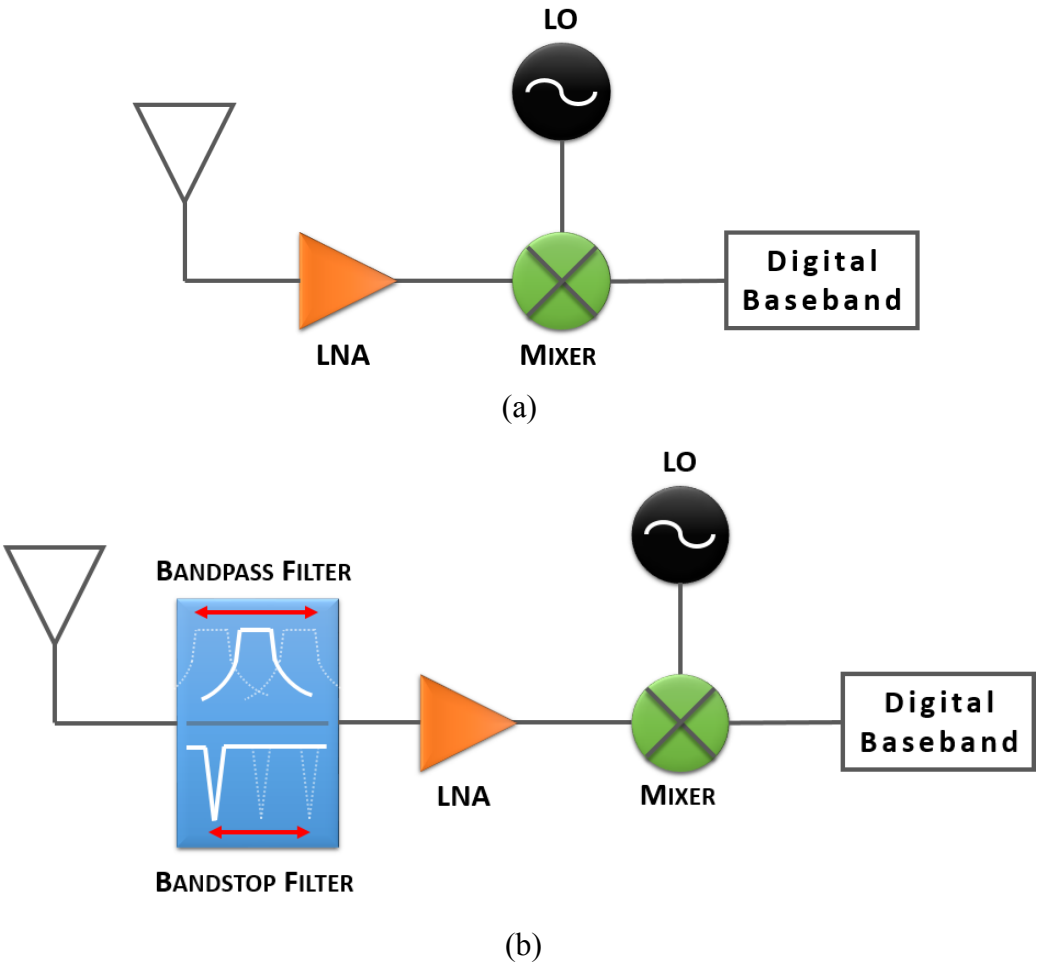

Fig. 1.1. (a) Receiver chain for a simple software-defined radio. (b) Receiver chain for a software-defined radio utilizing a tunable bandpass or bandstop filter between the antenna and LNA.

however, limiting the usefulness of such receivers and precluding them from use in spectral environments which contain strong interfering signals.

In order to achieve the same functionality while addressing the problem of interfering signals, a tunable filter can be inserted into the receiver chain in front of the LNA, as shown in Fig. 1.1(b). Tunable bandpass filters offer a potential solution, as they can dynamically preselect a certain band of frequencies while rejecting interferers at other frequencies. This filtering scheme would prove useful if the receiver only needs to receive signals in a single band at a time, and / or there are many interfering signals which need to be simultaneously suppressed. However, if the receiver needs to receive signals on multiple bands simultaneously, and / or there is only one strong interfering

signal, then a tunable bandstop filter might prove to be more useful as it can highly attenuate a narrow band of frequencies while passing all other frequencies with minimal loss. Other more highly reconfigurable types of filters could also be used, such as bandpass-to-bandstop switchable filters, bandpass filters with tunable bandwidths and / or transmission zeros, etc.

1.2 Overview of Tunable Filter Technologies

A multitude of different technologies have been used in the past half of a century to realize tunable filters. The following sections will give an overview of these technologies.

1.2.1 Ferrimagnetic Filters

Perhaps the oldest variety of tunable filters are those which utilize ferrite materials as tuning elements, dating back to at least the 1950's [1]. Yttrium-Iron-Garnet (YIG) is the most common magnetic material used in such resonators. A single-crystal of YIG machined into a sphere acts as a microwave resonator, and the resonant frequency can be tuned by applying a magnetic bias field. By coupling multiple of these YIG resonators together, a frequency-tunable filter can be realized. YIG resonators have very high quality factors (typically 1,000-2,000) and can be tuned over very wide frequency ranges (often more than an octave). They possess a number of drawbacks, however. Due to the hysteretic properties of the ferrite materials which comprise YIG resonators, they suffer severe hysteresis effects in their frequency-tuning characteristics. This necessitates complex control algorithms, which increase the overall size and complexity of the filters and slows their tuning speeds. A large current is required to generate the magnetic bias field, which results in high power consumption (typically several watts) and precludes these filters from use in battery-powered devices. Despite all of the drawbacks, many commercially-available YIG-tuned filter modules exist [2]–[4].

1.2.2 Varactor-Tuned Filters

Tunable filters which use variable-capacitance varactor diodes as tuning elements have been researched since the 1980's [5], [6]. Varactor diodes are semiconductor

junction devices in which the junction capacitance can be controlled by an applied reverse bias voltage. Varactors can achieve wide capacitance tuning ratios, up to 10:1 [7]. The tuning speed of varactors is very fast, often on the order of 10's of nanoseconds. The quality factor of a varactor is determined by its effective series resistance, which stems from the losses in the semiconductor material. Typical semiconductor materials used are silicon and gallium-arsenic (GaAs). Filters using varactors as tuning elements have been implemented using lumped-element resonators [8]–[12], microstrip resonators [5], [6], [13]–[24], and substrate-integrated cavity resonators [25]–[29]. Due to the relatively high semiconductor losses in varactors, the quality-factor of varactor-tuned filters is usually dominated by the Q of the varactor, and is usually limited to 50-100 at frequencies from 0.5 to 4 GHz. The power handling and linearity of such filters is also quite limited due to the non-linear nature of the varactor diodes.

1.2.3 RF MEMS Tunable Filters

A more recent approach to realize reconfigurable filters uses Radio-Frequency Microelectromechanical Systems (RF MEMS) as tuning elements. RF MEMS components use micron-scale (1 – 1000 μm) movable mechanical components to achieve reconfigurability. Examples include ohmic-contact switches, in which a thin metal beam creates metal-to-metal contact between two signal paths, and varactors, in which thin, deflectable beams are used to create variable-gap parallel plate capacitors. RF MEMS devices avoid the use of semiconductors in signal paths, which in turn reduces both losses and non-linearities in the device. This allows RF-MEMS-tuned filters to have very high performance when compared to varactor-tuned filters, with quality factors often ranging from 100-300. The increased performance comes at the expense of slow speed (typical 10's of microseconds), limited reliability, and high cost of fabrication and packaging. Many examples of RF MEMS tunable filters can be found in [30]–[38].

1.2.4 Evanescent-Mode Cavity Filters

Evanescent-mode cavity resonators are below-cutoff sections of waveguide loaded with capacitive tuning elements. The basic structure of such a cavity resonator is shown in Fig. 1.2, which consists of a rectangular metal cavity loaded with a central metal post.

The post is connected to the bottom of the cavity, but a small gap (on order of 1 to 20 μm) is left between the top of the post and the ceiling of the cavity. A parallel-plate capacitance is formed between the top of the post and the ceiling of the cavity, lowering the frequency of the resonator and making the resonant frequency very sensitive to the gap between the post and the ceiling. If the ceiling of the cavity is moveable by utilizing an actuator such as a piezoelectric disc or an electrostatically-actuated membrane, then the gap and thus the frequency of the resonator can be tuned. Because there are no dielectric or semiconductor losses or non-linearities, the resonators have very high quality factors, ranging from 300-1,500. Wide tuning ranges can also be realized, with up to two octaves being demonstrated [39]. Many excellent examples of tunable filters have been demonstrated using this technology [39]–[83]

The drawbacks of evanescent-mode cavity resonator-based filters include relatively large size at low frequencies compared to lumped element filters, slow tuning speed compared to varactor-tuned filters (tens of microseconds to several milliseconds, depending on the actuator used) and potentially complex control algorithms if piezoelectric discs (which suffer from hysteresis issues) are used. Most of the research contained in this dissertation utilizes these resonators because of their extremely high performance compared to other types of tunable resonators.

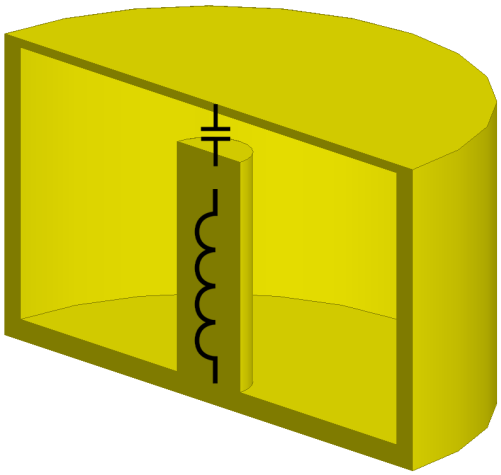

Fig. 1.2. Cross section view of an evanescent-mode cavity resonator.

1.3 Dissertation Overview

This dissertation is organized into chapters as follows:

- Chapter 2 presents a detailed theoretical and practical analysis of absorptive bandstop filters, a relatively new class of bandstop filter which overcomes some of the limitations of traditional reflective bandstop filters by allowing the filter to achieve theoretically infinite stopband attenuation despite the use of finite-quality-factor resonators, which usually limits the amount of achievable stopband rejection in traditional reflective bandstop filters. This chapter fills in many of the knowledge gaps associated with this type of filter by investigating and optimizing the sensitivity of the filters to process variations, the tradeoffs between selectivity and tuning range, the relative benefits and drawbacks of higher-order absorptive filters, and presents a clear design procedure for realizing such filters. Several absorptive filters realized with varactor-tuned microstrip resonators are designed and implemented to demonstrate the design process and design tradeoffs. The filters are able to achieve greater than 90 dB of stopband rejection despite using low-Q (< 100) resonators
- Chapter 3 demonstrates widely tunable, high-isolation Ka- and W-band bandstop filters realized with evanescent-mode resonators. These filters combine the theory and design principles developed in Chapter 2 with the high-quality-factors and wide tunability afforded by silicon-micromachined evanescent-mode cavity resonators to realize large notch depths of up to 70 dB, with 3-dB bandwidths as narrow as 1.5% and out-of-band insertion loss of less than 3.25 dB. Two filters are presented, which have 22 to 43 GHz and 75 to 103 GHz tuning ranges. These filters are fabricated using all-silicon technology, and are tuned with low-power electrostatic actuators which have bias voltages of less than 90V. The demonstrated filters have the potential to enable robust millimeter-wave communication systems which can operate in the presence of large interfering signals.
- Chapter 4 presents a novel switched-frequency filter utilizing commercially-available RF MEMS switched-capacitor bank as a tuning element. The filter has

two passbands, located at 0.95 GHz and 2.45 GHz, which can both be activated or deactivated independently. The filter uses an intrinsic switching topology, in which deactivation of one of the passbands is achieved by detuning some of the filter's resonators. This technique allows the filter bank to achieve < 20 dB of off-state isolation for each band, while maintaining low on-state passband insertion since no lossy switching elements (such as solid-state microwave switches) are in the direct signal path, as is the case in traditional switched filter banks. This chapter represents the winning entry of the 2015 RF MEMS Tunable Filter student design competition at the 2015 International Microwave Symposium.

- Chapter 5 presents a new bandwidth compensation method which allows high-Q evanescent-mode cavity resonator-based filters to be implemented with nearly constant absolute or fractional bandwidth, in contrast to traditional widely-tuned evanescent-mode filters which experience large variations in bandwidth across their center frequency's tuning range. This bandwidth compensation method consists of coupling each resonator in the filter to the source-to-load through-line with two coupling elements, separated by a length of transmission line. This induces a frequency variation into the coupling coefficient which, if designed correctly, compensates the positive frequency dependence inherent to the coupling elements to either provide a constant coupling coefficient for constant fractional bandwidth filters, or a negatively-sloped coupling coefficient for constant absolute bandwidth filters. The method is demonstrated with octave tunable filters, and it is shown that this new method can reduce the absolute bandwidth variation over an octave tuning range by up to 95% compared to the traditional coupling method.
- Chapter 6 introduces for the first time a method for implementing tunable balanced-to-unbalanced (balun) filters using evanescent-mode cavity resonators. To date very few tunable balun filters (that is, microwave filters which have a single-ended input and a differential output) have been demonstrated, due to the difficulty in maintaining good amplitude and phase balance between the differential output ports across a wide tuning range. This chapter develops a differential external coupling mechanism for evanescent-mode cavity resonators

which behaves very nearly like an ideal balun attached to the output of the filter. A 3-pole 3.2 to 6.1 GHz tunable balun filter is demonstrated using this coupling method. The filter maintains < 0.2 dB of amplitude imbalance and < 0.9^{o} of phase imbalance across its entire tuning range. This is better performance than any other tunable balun filters demonstrated to date. Morever, at its best tuning state with respect to amplitude/phase imbalance (center frequency of 6.2 GHz), the filter has less than 0.024 dB of amplitude imbalance and less than 0.2^{o} of phase imbalance, which is better than existing state-of-the-art static balun filters.

- Chapter 7 presents a new broadband external coupling structure for tunable bandstop filters utilizing evanescent-mode cavity resonators. The typical method for realizing external coupling in these filters uses a large slot in the ground plane of the source-to-load transmission line, but this introduces parasitics which severely degrade the upper passband of the filter. The coupling method presented in this chapter is a modification of the work in [56], extending it so that it works at higher frequencies and can be realized using a much simpler fabrication process. This new coupling structure is used to realize a 3 to 6 GHz tunable bandstop filter whose 3-dB passband extends up to 28.5 GHz. This is the widest fractional upper passband (ratio of the 3-dB upper passband to the lowest tuned resonator frequency) reported for any filter with a center frequency greater than 2 GHz.
- Chapter 8 summarizes the major contributions of dissertation and presents future work. A frequency-tunable fully-differential bandpass filter is proposed as an extension of the work in Chapter 6. It is shown that utilizing the differential coupling structure from Chapter 6 at both the input and output of the filter creates a fully-differential filter which has greater than 80 dB of common-mode rejection in its passband.

2. THEORY AND DESIGN OF FREQUENCY-TUNABLE ABSORPTIVE BANDSTOP FILTERS

2.1 Introduction

One of the main attractive features of cognitive radio transceivers is their ability to dynamically adjust operation parameters such as center frequency, bandwidth, and modulation type, in order to optimally utilize the available spectrum [84]. Such transceivers often maximize frequency flexibility by utilizing very wideband RF front ends, but this leaves the receiver prone to jamming signals which can saturate the receiver and block the desired signals of interest. These jamming signals can come from a variety of intentional or unintentional sources, and are often dynamic, unpredictable, and can be many orders of magnitude stronger than the signals of interest. Tunable bandstop filters, which have the ability to dynamically suppress a narrow band of frequencies while maintaining a wide passband, offer a potential solution to this problem and, as a result, have garnered much research interest in recent years. One particular drawback of tunable bandstop filters, however, is that tunable resonators in compact form-factors tend to have low unloaded quality factors (Q_U). Since the amount of attenuation that a typical bandstop filter can achieve is limited when low-quality-factor resonators are used, many of the published tunable bandstop filters fail to provide the high levels of rejection that are needed in cognitive radio applications.

A bandstop filter utilizing evanescent-mode cavity resonators is presented in [56]. Its maximum attenuation only ranges from 15-35 dB with a 1.2% to 3.2% fractional bandwidth. In [85] a varactor-tuned micostrip bandstop filter is demonstrated with 37-40 dB of stopband attenuation for a fractional bandwidth of 10%-14 %. Stopband rejection of 7-27 dB with a fractional bandwidth of 1.6%-3.6% is presented in [26], which is a bandstop filter implemented with varactor-tuned substrate-integrated evanescent-mode

cavity resonators. Other notable examples of tunable bandstop filters can be found in [12], [86], [87].

A new class of bandstop filter which partially overcomes the aforementioned problems caused by low-quality-factor resonators was recently introduced in [23], [88], [89]. This type of filter achieves its stopband attenuation not by reflecting incident signals as traditional reflective bandstop filters do, but by utilizing two signal paths which are 180^{o} out of phase and result in destructive interference over a narrow bandwidth. This allows the filter to achieve very large (theoretically infinite) attenuation in its stopband, regardless of the constituent resonators' unloaded quality factors. This kind of filter is called an "absorptive bandstop filter" because it realizes increased stopband attenuation by absorbing a portion of the incident signals which would otherwise be reflected. The concept has been utilized by several authors since, and has been demonstrated in technologies such as microstrip [18], [24], lumped elements [8], [11], and evanescent-mode cavities [45], [53], [82], [90]. Despite the many excellent examples of absorptive bandstop filters which have been published, several aspects of this class of filter have not yet been investigated. For example, none of the aforementioned papers have discussed how to predict or optimize the tuning range over which a tunable absorptive bandstop filter can achieve very large stopband attenuation. Additionally, there has been no discussion of how to design an absorptive bandstop filter to meet a certain bandwidth requirement, no analysis of the design tradeoffs which must be made when designing such filters, and no step-by-step design procedure other than an iterative manual optimization process.

In response to these and other knowledge gaps, this chapter seeks to present a detailed analysis of absorptive bandstop filters which furthers knowledge of this class of filter. A theoretical foundation for optimizing the tuning range over which absorptive bandstop filters can achieve (ideally) infinite attenuation is developed, along with design principles to increase their robustness to process variations. The tradeoffs between selectivity and tuning range, and the impact of non-ideal effects such as coupling dispersion, transmission-line length variation, and parasitic coupling are examined and design principles are developed to mitigate these effects.

First, the topology of an absorptive bandstop filter is presented, and relevant equations are derived in detail. The tradeoffs between various performance metrics such as bandwidth, tuning range, and sensitivity are examined, and practical design considerations are presented. A comparison of the relative benefits and drawbacks of higher-order versus lower-order filters is made. Lastly, a step-by-step design procedure is presented, and several varactor-tuned microstrip absorptive bandstop filters are designed, fabricated, and measured to validate the theory and design principles presented in this chapter.

2.2 Design Principles of absorptive Filters

2.2.1 Analysis of a Two-Pole Absorptive Bandstop Filter

A schematic representation of a two-pole absorptive bandstop filter is shown in Fig. 2.1(a). This circuit was first disclosed in [23], [89], and the following analysis in Section II.A bears similarities to that in [23], [24] but is included here for the completeness of this chapter and to introduce the different notation and terminology used in this chapter.

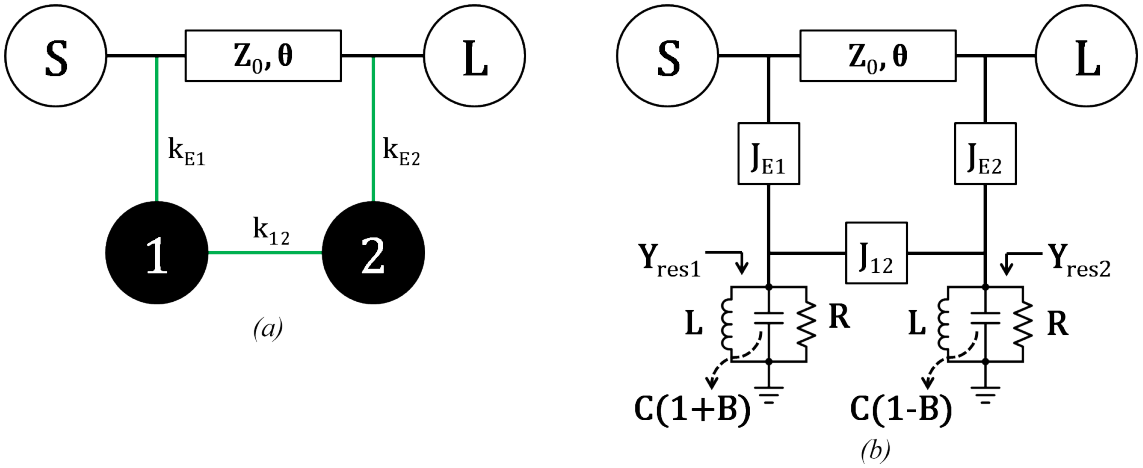

Fig. 2.1. (a) Schematic representation of a two-pole absorptive bandstop filter. (b) Equivalent circuit of (a). Source-to-load coupling is implemented by a transmission line of characteristic impedance Z_0 and electrical length θ, resonator coupling elements are implemented by admittance inverters, and resonators are represented as parallel RLC resonators.

The filter consists of two resonators coupled to a source-to-load transmission line of length θ with coupling coefficients $k_{E1,2}$, and coupled to each other with coupling

coefficient k_{12}. Though represented as shunt-parallel RLC resonators in Fig. 2.1(b), the resonators can be implemented as any resonators which have parallel RLC equivalent circuits near resonance. The coupling elements are implemented as admittance inverters scaled by the resonator and system characteristic impedances as defined in [91], and the source-to-load coupling is assumed to be an ideal TEM transmission line. With the sign convention used in this analysis, positive coupling provides a +90° insertion phase whereas negative coupling yields a -90° insertion phase. The source and load impedances are assumed in this analysis to be identical to the characteristic impedance of the transmission line. The expressions in Fig. 2.1 are defined as follows:

$$Y_{res1,2} = \frac{1}{Z_R}\left(\frac{1}{Q_U} + p \pm jB\right) \tag{2.1}$$

$$p = j\left(\frac{\omega}{\omega_0} - \frac{\omega_0}{\omega}\right) \tag{2.2}$$

$$J_{12} = k_{12}/Z_R \tag{2.3}$$

$$J_{E1,2} = k_{E1,2}/\sqrt{Z_0 Z_R} \tag{2.4}$$

$$Z_R = \sqrt{L/C} \tag{2.5}$$

$$\omega_0 = 1/\sqrt{LC} \tag{2.6}$$

$$Q_U = \frac{R}{\omega_0 L} = \omega_0 RC \tag{2.7}$$

$Y_{res1,2}$ represents the admittance of each resonator, and is simply the parallel combination the inductor, capacitor, and resistor which comprise each resonator, slightly rearranged and reduced using the definitions for the frequency variable (2.2), the resonators' impedances (2.5), and the resonators' unloaded quality factors (2.7). The capacitors are differentially tuned by a factor of 1±B, which allows for asynchronous tuning of the resonators if B is chosen to be nonzero. The frequency-invariant reactance B in equation (2.1) which appears as a result of this differential capacitance tuning is only approximate – in reality the reactance would have frequency dependence, but in the narrowband case it can be approximated as constant. Equations (2.2) and (2.5)-(2.7) are derived from [92]

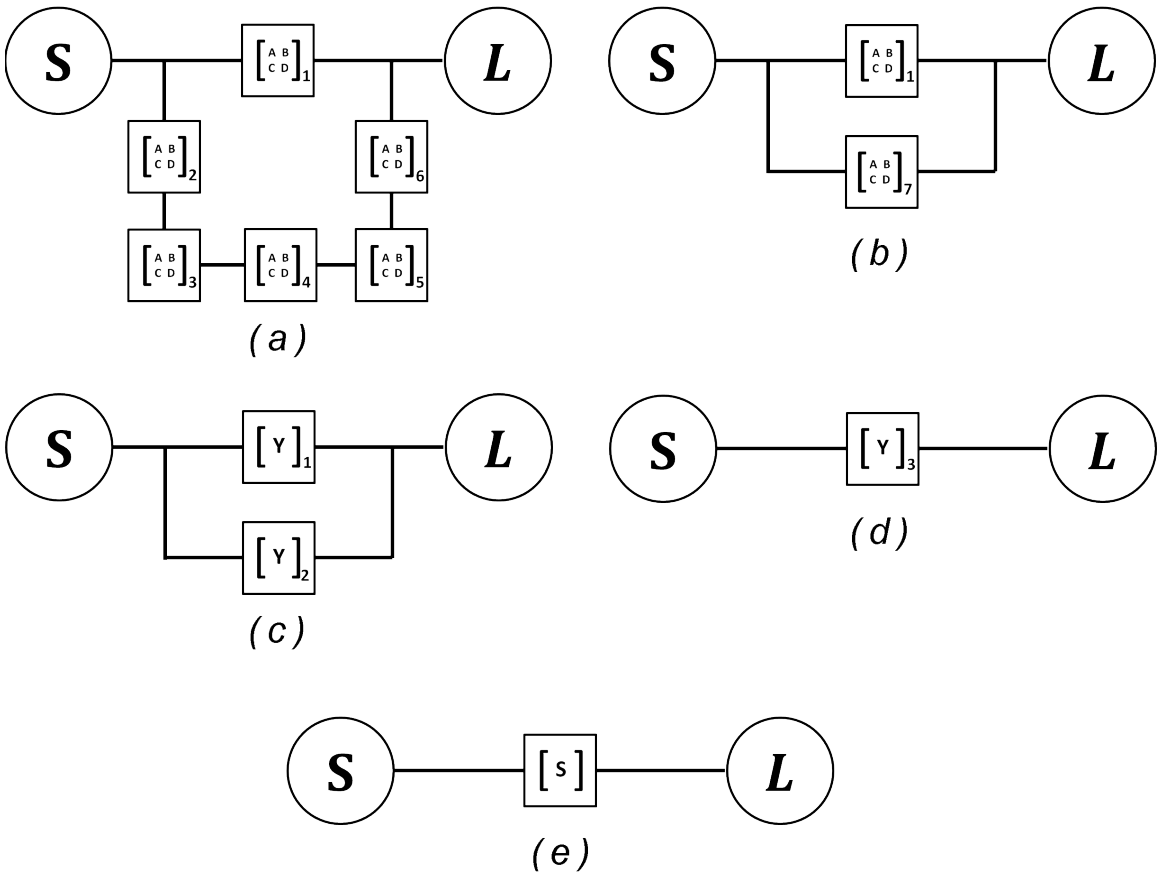

Fig. 2.2. Step-by-step process for calculating the S-parameters of the circuit in Fig. 2.1.

To obtain the transmission and reflection coefficients (S_{21} and S_{11}) of the circuit in Fig. 2.1(b), all components are first converted into their representative ABCD matrices (Fig. 2.2(a)) using the expressions in equations (2.8)-(2.23) [92], [93].

$$A_1 = \cos(\theta) \quad (2.8) \qquad A_{3,5} = 1 \quad (2.9)$$

$$B_1 = jZ_0\sin(\theta) \quad (2.10) \qquad B_{3,5} = 0 \quad (2.11)$$

$$C_1 = j/Z_0\sin(\theta) \quad (2.12) \qquad C_{3,5} = Y_{res1,2} \quad (2.13)$$

$$D_1 = \cos(\theta) \quad (2.14) \qquad D_{3,5} = 1 \quad (2.15)$$

$$A_{2,6} = 0 \quad (2.16) \qquad A_4 = 0 \quad (2.17)$$

$$B_{2,6} = -j/J_{E1,2} \quad (2.18) \qquad B_4 = -j/J_{12} \quad (2.19)$$

$$C_{2,6} = -j \cdot J_{E1,2} \quad (2.20) \qquad C_4 = -j \cdot J_{12} \quad (2.21)$$

$$D_{2,6} = 0 \quad (2.22) \qquad D_4 = 0 \quad (2.23)$$

The elements in the bottom branch of the circuit (the resonators and coupling elements) are cascaded together by multiplying their ABCD matrices (Fig. 2.2(b)). The resulting matrix is converted into its equivalent Y-parameter matrix (Fig. 2.2(c)), which is then added to the Y-parameter matrix of the transmission line due to their parallel configuration (Fig. 2.2(d)). The resulting Y-parameter matrix is converted into its equivalent S-Parameter matrix [93] (Fig. 2.2(e)). The resulting transmission and reflection coefficients are given in (2.25)-(2.27). Inspection of (2.25) shows that $S_{21} = 0$ at the filter's center frequency ($\omega = \omega_0$, or alternatively $p = 0$) when

$$\frac{1}{{Q_U}^2} + B^2 + {k_{12}}^2 + k_{12}k_{E1}k_{E2}\sin\theta = 0. \tag{2.24}$$

The filter has theoretically infinite attenuation even with finite-Q_U resonators if this equation is satisfied, and thus it is the governing equation for absorptive bandstop filters.

The mechanism by which absorptive bandstop filters achieve infinite attenuation can be seen by examining the poles and zeros of S_{21}. For simplicity, the highpass prototype equivalent of (2.25) is used, which can be obtained by redefining (2.2) as $p = j\omega$. Equations for the poles and zeros can be found in [24]. Fig. 2.3 shows the poles and zeros

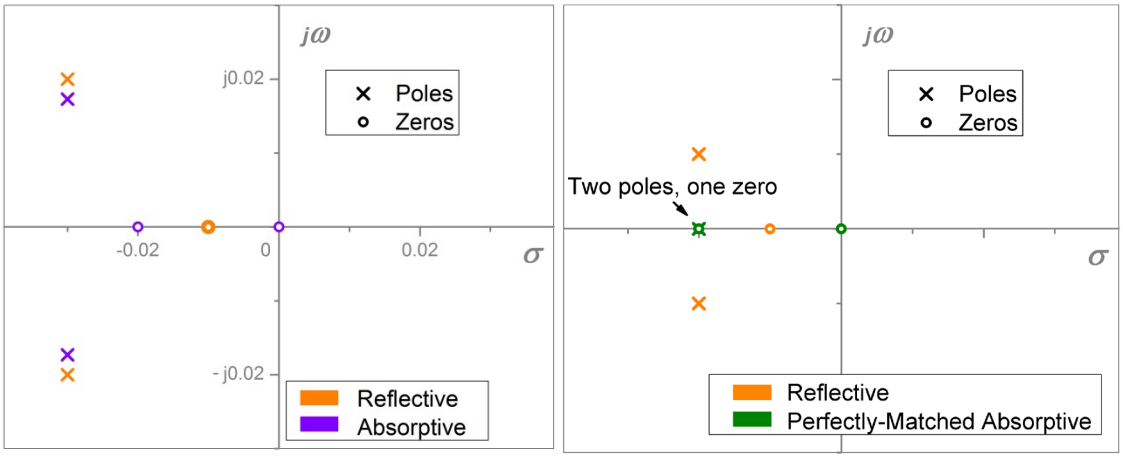

(a) *(b)*

Fig. 2.3. Poles and zeros of S_{21} for *(a)* reflective and absorptive bandstop filters, and *(b)* reflective and perfectly-matched absorptive bandstop filters. In the case of the perfectly-matched absorptive bandstop filter, a pole and a zero cancel each other out, leaving a single pole/zero pair which corresponds to an ideal 1st order bandstop filter.

$$S_{21} = \frac{e^{-j\theta}\left(p^2 + \frac{2}{Q}p + B^2 + {k_{12}}^2 + \frac{1}{Q_U^2} + k_{12}k_{E1}k_{E2}\sin\theta\right)}{p^2 + \frac{4 + \left({k_{E1}}^2 + {k_{E2}}^2\right)Q_U}{2Q_U}p + je^{-j\theta}\,k_{E1}k_{E2}\left(k_{12} + \frac{1}{2}k_{E1}k_{E2}\sin(\theta)\right) + \frac{1}{Q_U^2} + \frac{1}{2Q_U}\left(k_{E1}^2 + k_{E2}^2\right) + B^2 + k_{12}^2 + j\frac{B}{2}\left(k_{E1}^2 - k_{E2}^2\right)} \tag{2.25}$$

$$S_{11} = \frac{-\frac{1}{2}\left(k_{E1}^2 + e^{-2j\theta}\,k_{E2}^2\right)p + \mu}{p^2 + \frac{4 + \left({k_{E1}}^2 + {k_{E2}}^2\right)Q_U}{2Q_U}p + je^{-j\theta}\,k_{E1}k_{E2}\left(k_{12} + \frac{1}{2}k_{E1}k_{E2}\sin(\theta)\right) + \frac{1}{Q_U^2} + \frac{1}{2Q_U}\left(k_{E1}^2 + k_{E2}^2\right) + B^2 + k_{12}^2 + j\frac{B}{2}\left(k_{E1}^2 - k_{E2}^2\right)} \tag{2.26}$$

$$\mu = -je^{-j\theta}k_{12}k_{E1}k_{E2} + \frac{e^{-2j\theta}k_{E2}^2(-2 + 2jBQ + k_{E1}^2Q)}{4Q} - \frac{k_{E1}^2(2 + 2jBQ + k_{E2}^2Q)}{4Q} \tag{2.27}$$

of both a two-pole reflective bandstop filter and a two-pole absorptive bandstop filter. The reflective filter has a double zero which is offset from the $j\omega$ axis due to the use of finite-Q_U resonators, and thus has limited attenuation. The absorptive filter's interresonator coupling, along with the asynchronous tuning of its resonators, splits the zeros, restoring one zero to the origin while moving the other zero to the left in the complex plane. Thus the absorptive filter has infinite attenuation at its center frequency, but has less selectivity than a lossless two-pole bandstop filter which has two zeros at the origin. When $B = 0$, $k_{12} = 1/Q_U$, and $\theta = 90^o$, as in the case of the perfectly-matched absorptive filter, the two poles fall on top of one of the zeros. This cancels a pole/zero pair, leaving one pole and one zero – corresponding to a lossless 1st order bandstop filter.

Many combinations of $k_{E1,2}$, k_{12}, B, Q_U and θ can provide valid solutions to (2.24), and thus it is instructive to examine the bounds placed on each variable, and to see how the choice of each variable affects the filter's transfer function. It should be noted that in the following analysis, the coupling coefficients ($k_{E1,2}$, k_{12}) and quality factor (Q_U) are assumed to be frequency-independent, and the transmission line length (θ) is assumed to be linearly proportional to frequency. While this is not precisely true in practice, this simplification is often sufficiently accurate in narrowband designs and is an important analysis step. Fine tuning and frequency-dependent effects are analyzed in Section III.

2.2.2 Limits on External Coupling

The limits on external coupling (k_{E1} and k_{E2}) can be found by solving (2.24) for k_{E1} and k_{E2}, which yields the following equation:

$$k_{E1}k_{E2} = -\frac{\frac{1}{Q_U^2} + B^2 + k_{12}^2}{k_{12}\sin\theta} \tag{2.28}$$

This equation is similar to equation (8) in [23], with the important exception that it allows k_{E1} and k_{E2} to be different, both in magnitude and in sign. This provides two very useful insights about absorptive bandstop filters. First, it shows that the filter can still

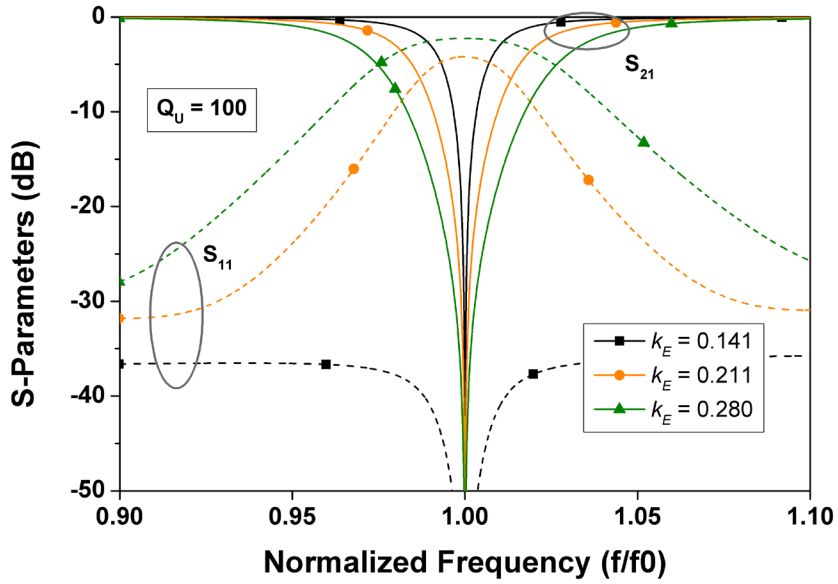

(a)

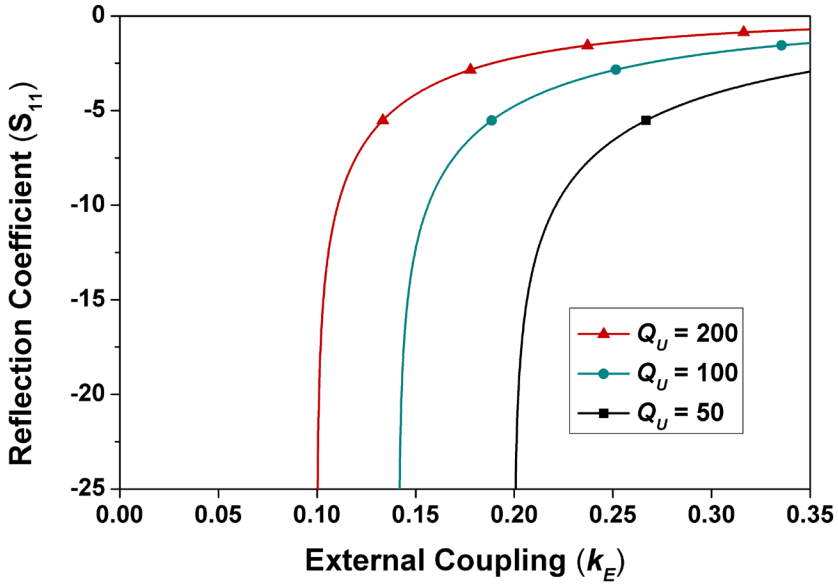

(b)

Fig. 2.4. (a) The effect that k_E has on bandwidth and reflection coefficient. (b) Variation of maximum reflection coefficient (at $\omega = \omega_0$) with k_E. $k_{12} = 1/Q_U$ and $\theta = 90^o$ in both figures. At the minimum value of k_E ($\sqrt{2/Q_U}$), the filter is perfectly matched and has zero reflection coefficient. When k_E is increased beyond its minimum value, the reflection coefficient becomes nonzero and increases with k_E. In each case the filter has infinite attenuation at its center frequency

achieve infinite attenuation even with small variations in external coupling due to manufacturing variations as long as (2.28) can still be satisfied. Second, it shows that the

relative polarities of k_{E1}, k_{E2}, and k_{12} dictate the length of transmission line which must be used.

In order for the signs of both the left- and right-hand sides of (2.28) to be consistent, the sign of the quantity $k_{E1}k_{E2}k_{12}\sin\theta$ must be negative. Therefore if either one or three of the variables k_{E1}, k_{E2}, and k_{12} are negative, then $\sin\theta$ must be positive ($0^o < \theta < 180^o$). However, if all of the aforementioned variables are positive, or two of them are negative, then $\sin\theta$ must be negative ($180^o < \theta < 360^o$). This is a key fact because as shown in Section II.D, the length of source-to-load transmission line is critical when maximizing the tuning range of the filter. A detailed explanation of how to determine the polarities of external and interresonator couplings is presented in Appendix A.

Though they can differ in sign as dictated by the physical coupling structure, the magnitudes of k_{E1} and k_{E2} are usually chosen to be equal for the sake of simplicity (i.e. $k_{E1} = k_E = \pm k_{E2}$). For a given k_{12}, Q_U, and θ, the minimum k_E which will allow ideally infinite attenuation is

$$k_{E,min} = \sqrt{\frac{\frac{1}{Q_U^2} + k_{12}^2}{k_{12}\sin\theta}}, \tag{2.29}$$

which occurs when B = 0. For any value of k_E larger than (2.29), B can be chosen by asynchronously tuning the resonators such that (2.28) is still satisfied. Minimizing (2.29) with respect to k_{12} and θ shows that the absolute minimum possible value for k_E for a given Q_U is

$$k_{E,min}^* = \sqrt{2/Q_U}, \tag{2.30}$$

obtained when $k_{12} = 1/Q_U$, and $\theta = 90^o$. If these values are substituted into (2.24), it can be seen that the filter has zero reflection coefficient, and thus is a perfectly-matched absorptive bandstop filter [23]. When k_E is larger than this absolute minimum value, the reflection coefficient is nonzero, and increases with increasing k_E as shown in Fig. 2.4.

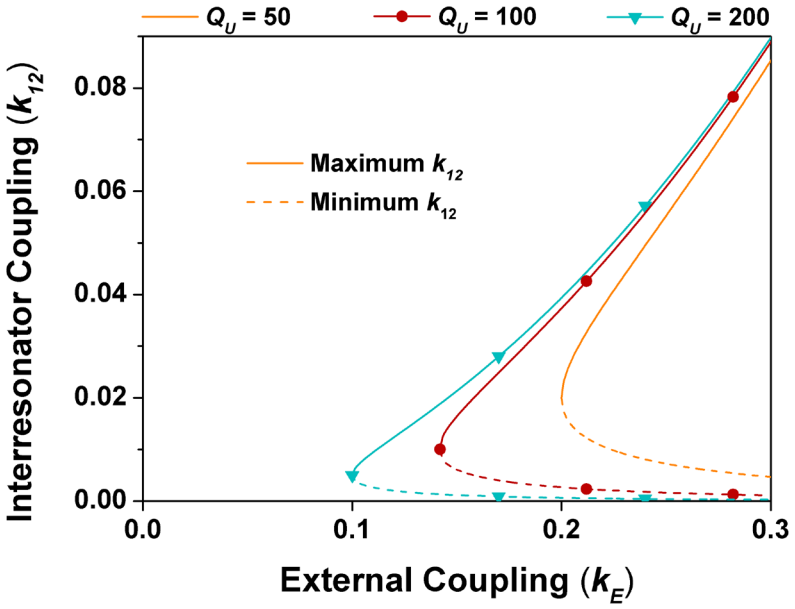

Fig. 2.5. Maximum and minimum allowable values for interresonator coupling (k_{12}) plotted versus external coupling (k_E) and unloaded quality factor (Q_U), obtained from (2.31) with $B = 0$. At the minimum value of k_E ($\sqrt{2/Q_U}$), there is only one permissible value for k12 ($1/Q_U$). A broader range of values for k_{12} can be used when k_E is increased beyond its minimum value, providing design flexibility and decreased sensitivity to process variations.

2.2.3 Limits on Interresonator Coupling

Solving (2.24) for k_{12} yields the following equation:

$$|k_{12}| = \frac{1}{2}\left[{k_E}^2|\sin\theta| \pm \sqrt{({k_E}^2\sin\theta)^2 - \frac{4}{Q_U^2} - 4B^2}\right] \tag{2.31}$$

All solutions for k_{12} come in pairs due to the quadratic nature of the equation. When $B = 0$, the two solutions represent the maximum and minimum allowable values of k_{12} for given k_E, Q_U, and θ. For all values of k_{12} between these extrema, B can be chosen by asynchronously tuning the resonators such that (2.31) is satisfied. Fig. 2.5 shows the maximum and minimum allowable values for k_{12} plotted versus k_E, for several values of Q_U. Note that when k_E is equal to its minimum value (2.30), there is only one possible value for k_{12}, whereas for k_E greater than (2.30) a range of values of k_{12} are possible. This is an important fact for designs which are robust to process variations. If the minimum k_E is chosen, then any slight variation in Q_U, k_{12}, or k_E will not allow infinite attenuation.

This can make the design process particularly challenging, because it is often difficult to accurately predict the unloaded qualify factor of tunable resonators. By choosing k_E larger than its minimum value, however, the design is desensitized to process variations, and small variations in k_E, Q_U, or k_{12} can be compensated by asynchronously tuning the resonators. However, this comes at the expense of decreased selectivity as is seen in Section II.E.

The ability to compensate for variations in k_E, k_{12}, Q_U, and θ by asynchronously tuning the resonators has previously been noted in [23]. However, this analysis shows for the first time the range of values of k_E and k_{12} that can be compensated by asynchronous tuning, and that the design robustness can be increased by increasing the value of k_E.

2.2.4 Tuning Range

Since (2.24) depends on the electrical length of the through-line (θ), which is proportional to frequency, it can only have solutions for a certain range of frequencies. Solving (2.24) for θ with B = 0 yields the minimum and maximum allowable values of θ for a given Q_U, k_{12}, k_{E1}, and k_{E2}:

$$\theta_{min} = \sin^{-1}\left(\frac{\frac{1}{Q_U^2} + B^2 + k_{12}^2}{k_E^2 k_{12}}\right) + n180° \tag{2.32}$$

$$\theta_{max} = 180° - \theta_1 + n360° \tag{2.33}$$

where n is an even integer if the sign of $k_{E1}k_{E2}k_{12}$ is negative, and an odd integer if the sign of $k_{E1}k_{E2}k_{12}$ is negative.

With an ideal, dispersionless transmission line, the electrical length (θ) of the transmission line is linearly proportional to frequency. The ratio of $\theta_{max}/\theta_{min}$ is equivalent to the ratio f_{max}/f_{min}, and this ratio can tell us the tuning range of the filter – that is, the range of center frequencies for which (2.24) can be satisfied. This ratio, designated as the tuning range (TR), is

$$TR = \frac{\theta_{max}}{\theta_{min}}. \tag{2.34}$$

If one seeks to design a widely-tunable absorptive bandstop filter, it is desirable to know how the choice of design parameters affects the tuning range, and how to increase the tuning range. The tuning range increases monotonically with Q_U and k_E, as shown in Fig. 2.6. However, it can be shown that there is an optimal value for k_{12} which maximizes (2.34):

$$k_{12,opt} = 1/Q_U \tag{2.35}$$

This optimal value of k_{12} can be seen in Fig. 2.7, which plots tuning range as a function of k_{12} for different values of k_E. It should be noted that this is the same value of k_{12} which minimizes k_E, as in equation (2.29).

By observing the limits on the numerator and denominator of (2.34), the absolute maximum tuning range can be determined. If k_E is chosen arbitrarily large and a nominally 90^o line is used, then it can be seen that θ_{max} approaches 180^o and θ_{min} approaches 0^o. The maximum tuning range is then $180^o/0^o$ or ∞:1, indicating that if k_E is chosen to be large enough an arbitrarily large tuning range can be achieved. In practice however, the tuning range is limited by how large k_E can practically be realized. If the nominal θ is 270^o, then as k_E becomes infinitely large, θ_{max} approaches 360^o and θ_{min} approaches 180^o. The ideally maximum tuning range is then $360^o/180^o$, or 2:1. This shows that the maximum possible tuning range for a filter with a nominally 270^o through line is one octave, although in practice the finite physically-realizable values of k_E will result in less than a 2:1 tuning range. Though a filter with a 90^o line cannot provide an infinite tuning range when practical coupling values are considered, it will always provide a larger tuning range than a filter utilizing a 270^o through-line for a given k_E, Q_U, and k_{12}. The same procedure shows that further increasing lengths of transmission line result in further decreasing tuning ranges. It is clear that if a wide tuning range is desired, the length of through-line should be chosen as short as possible. A 90^o through line is always preferable from this perspective, but in practice it is not always possible. As explained in Section II.A, the required length of transmission line depends on the relative signs of the coupling elements, and some filter technologies have no flexibility in the sign of the coupling elements or must sacrifice complexity or performance in order to change the coupling sign. In other situations, particularly at high frequencies and in designs on

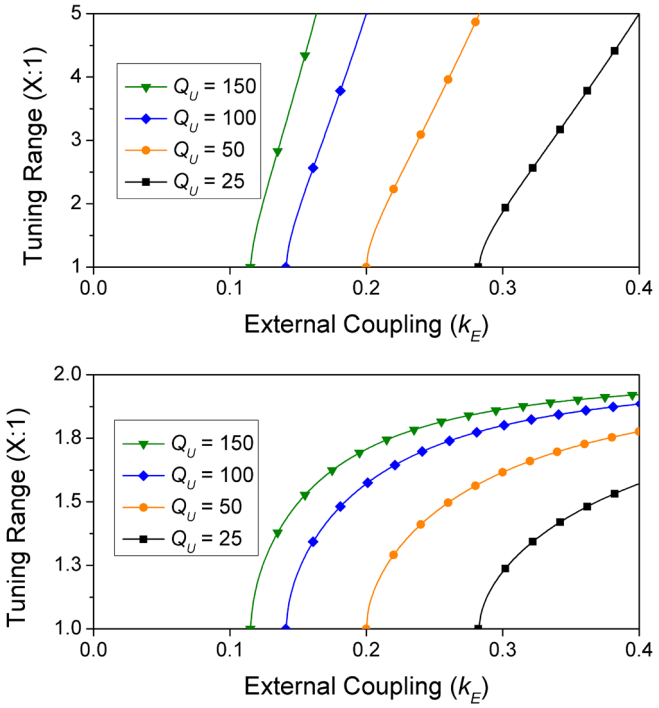

Fig. 2.6. Tuning range plotted versus external coupling with *(a)* a nominally 90° and *(b)* a nominally 270° source-to-load transmission line. Interresonator coupling k_{12} is the $1/Q_U$.

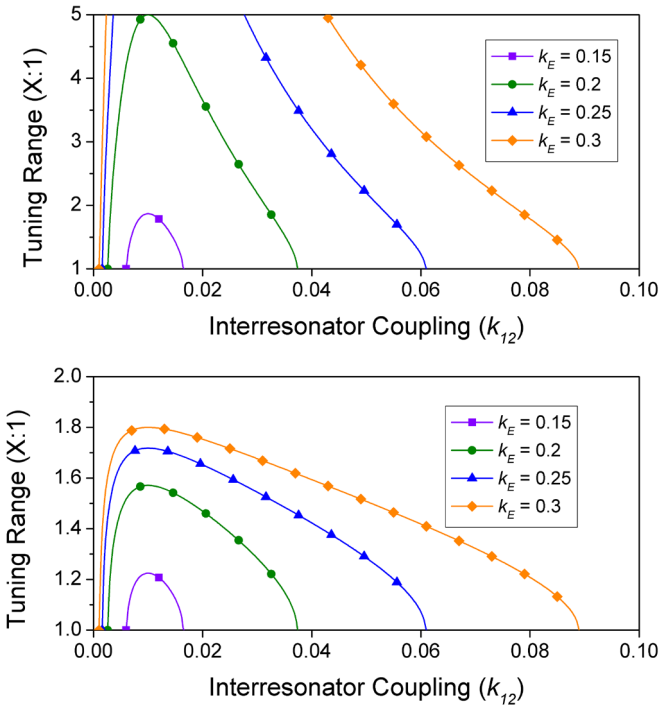

Fig. 2.7. Tuning range plotted versus interresonator coupling with *(a)* a nominally 90° and *(b)* a nominally 270° source-to-load transmission line. $Q_U = 100$

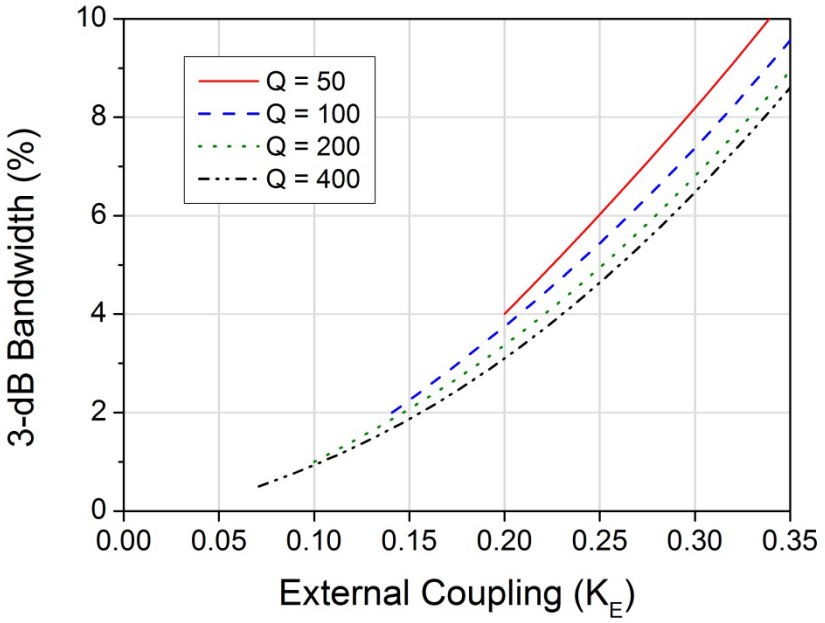

(a)

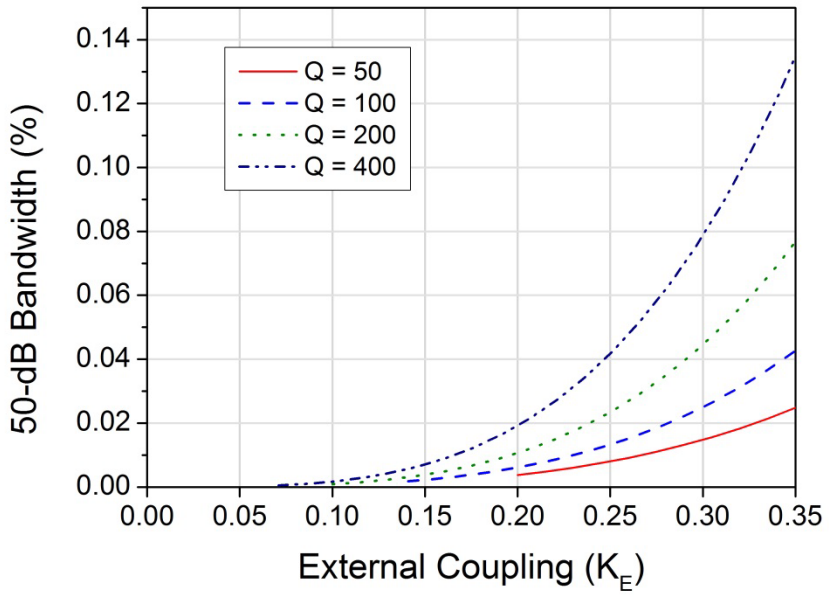

(b)

Fig. 2.8. Dependence of (a) 3-dB and (b) 50-dB fractional bandwidths on external coupling and unloaded quality factor.

high-permittivity substrates, a 90^{o} transmission line might be too short to practically implement between the resonators. Thus, it is necessary to investigate the performance of absorptive filters which utilize nominally 270^{o} through-lines.

2.2.5 Bandwidth

Bandwidth is a critical design parameter of bandstop filters, and thus it is important to determine the dependence of bandwidth on the various filter design variables. The *X*-dB bandwidth of the filter (defined as the bandwidth of the filter at an attenuation level of *X* dB) can be obtained from (2.25):

$$BW = \sqrt{\frac{1}{R}\left[L_A(2+K) - 2 + \frac{1}{2}\sqrt{16+Z}\right]} \tag{2.36}$$

$$Z = (K^2-4)[4(2-L_A) + K(4+K)(1-L_A)]L_A \tag{2.37}$$

$$R = Q_U^2(1-L_A) \tag{2.38}$$

$$K = {k_E}^2 Q_U \tag{2.39}$$

$$L_A = 10^{-\frac{X}{10}} \tag{2.40}$$

The transmission line length θ is set equal to 90° in order to simplify the equations. If $k_E = \sqrt{2/Q_U}$, as in the case of a perfectly-matched absorptive bandstop filter as described in Section II.B, then equation (2.36) reduces to

$$BW = 2/(Q_u\sqrt{10^{\frac{X}{10}} - 1}) \tag{2.41}$$

which identical to the equation for the bandwidth of absorptive bandstop filters derived in [23].

The dependence of 3-dB and 50-dB bandwidths on k_E and Q_U are shown in Fig. 2.8. The bandwidth has a strong dependence on k_E, and a weaker dependence on Q_U. Although high levels of attenuation can be achieved regardless of resonator quality factor, higher selectivity (narrower 3-dB bandwidth and larger 50-dB bandwidth) can be achieved with higher-Q_U resonators.

The dependence of 3-dB bandwidth on the length of the through-line (θ) can be obtained through simulation, and is shown in Fig. 2.9. For a nominally 90° through-line, the bandwidth variation with respect to θ is minimal for realistic values of θ which will

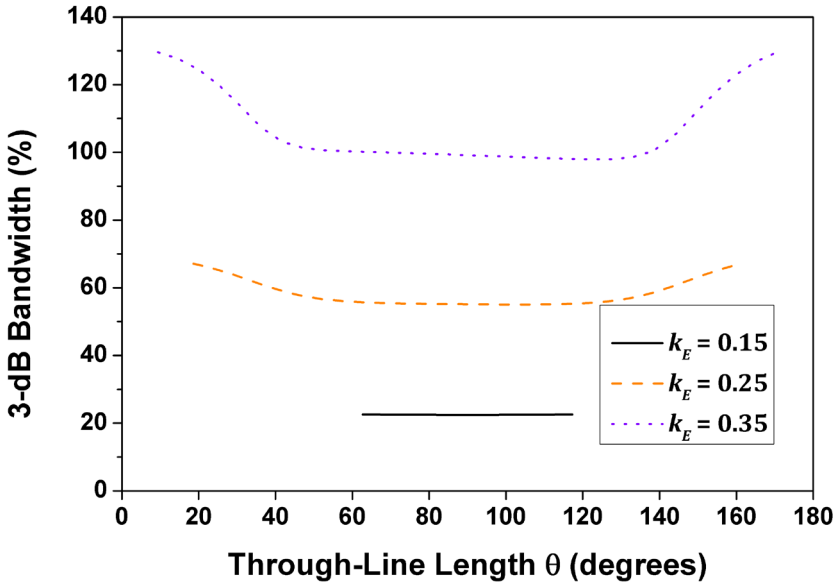

Fig. 2.9. Effect of through-line length (θ) on 3-dB bandwidth. $Q_U = 100$, $k_{12} = 0.01$.

be encountered in a tunable filter. However, when a nominally 270° through-line is used, even a filter with a tuning range of 1.5:1 can experience bandwidth variations of 20% or more. The choice of k_{12} has very little effect on bandwidth, as long as it is chosen according to (2.31).

Because the tuning range and the bandwidth are both strongly dependent on k_E, it is possible to examine the maximum tuning range for a given bandwidth, and vice versa. A plot of bandwidth vs. tuning range for several values of Q_U is shown in Fig. 10. From this graph it can be seen that in order to increase tuning range by increasing k_E, the bandwidth must also be increased. However, if higher Q_U resonators can be used, the same tuning range can be obtained with a smaller bandwidth. This effect is much more prominent for filters with nominally 270° through-lines, which are limited to a maximum possible tuning range of 2:1.

2.2.6 Higher Order Filters

Although a two-pole absorptive bandstop filter is able to achieve large maximum attenuation, it can only do so over a very narrow bandwidth. For example, the two-pole filter in Fig. 2.12(a) only has a 0.14% 50-dB bandwidth for a 3-dB bandwidth of 9.7%. If high attenuation is required over a wider bandwidth, the order of the filter can be

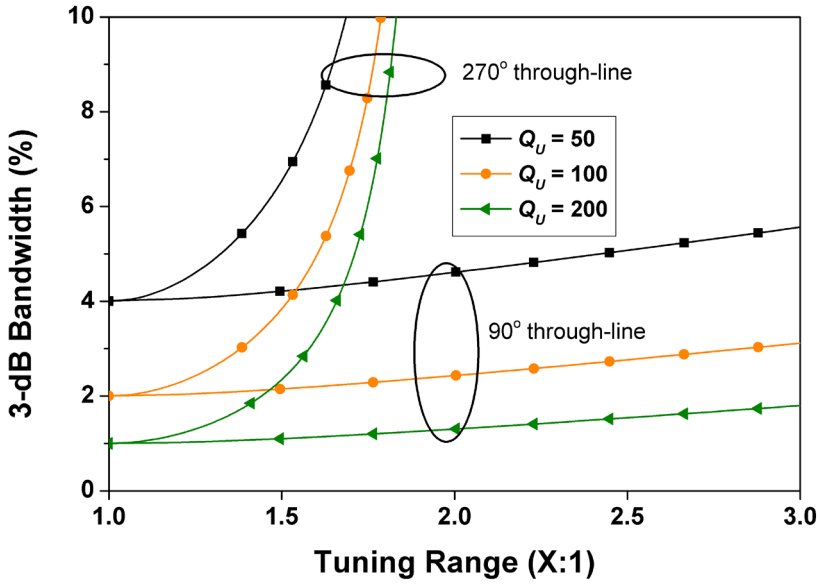

(a)

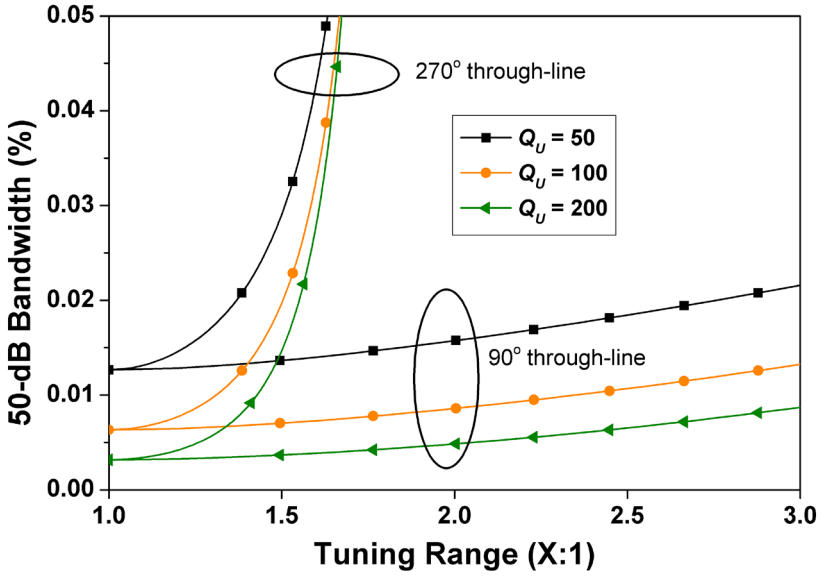

(b)

Fig. 2.10. Relationship between tuning range and minimum *(a)* 3-dB and *(b)* 50-dB fractional bandwidths. Larger tuning ranges require larger values of k_E, which results in wider bandwidths. $|k_{12}| = 1/Q_U$.

increased by cascading two or more two-pole stages. In general 90° transmission lines are required in order to have a symmetric filter transfer function [94], due to the impedance mismatch between the stages. However, in cases where the two-pole stages have very small reflection coefficients (as discussed in Section II.B), the impedance mismatch between stages is less pronounced and the exact length of the inter-stage

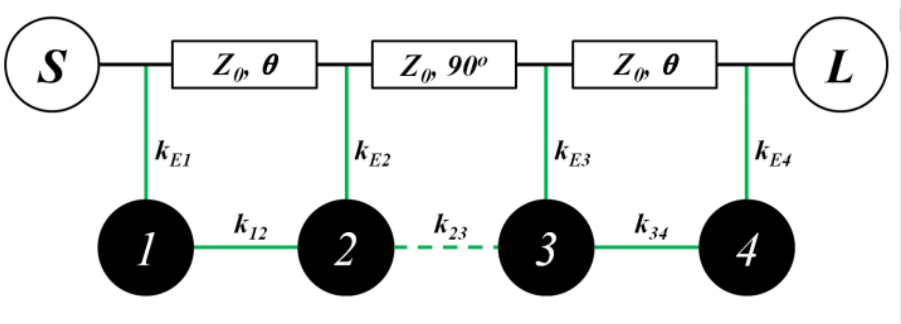

Fig. 2.11. Schematic of a four-pole absorptive filter created by cascading two two-pole sections with a 90° transmission line between sections. Undesired inter-stage coupling is represented with the dashed line (k_{23}).

transmission line becomes less important. For example, in [18], [24], approximately 30° long inter-stage transmission lines are used. The increased selectivity of higher-order filters is shown in Fig. 2.12(a), in which the four-pole filter (purple trace)has a 12× greater 50-dB bandwidth (1.7%) than the two-pole filter, for the same 3-dB bandwidth. This comes at the expense of a smaller tuning range and increased passband insertion loss, however. It can be seen in Fig. 2.12(b) that four- and six-pole filters require smaller external coupling (k_E) values than a two-pole filter for an equivalent 3-dB bandwidth, and this reduces the center-frequency tuning range over which the filter can achieve high attenuation as discussed in Section II.D.

It is critical to prevent coupling between the stages when cascading 2-pole stages to form higher-order filters. Parasitic coupling between the two adjacent resonators of the separate stages (k_{23} in Fig. 2.11) reduces the maximum level of attenuation by a pole-splitting effect. Fig. 2.13 shows the maximum attenuation states of a four-pole filter with various levels of parasitic inter-stage coupling.

2.3 Design of Microstrip Absorptive Bandstop Filters

To verify the preceding design principles and demonstrate a practical design example, four microstrip-based absorptive bandstop filters were designed. All filters were implemented with varactor-tuned, grounded quarter-wave microstrip resonators, chosen for their ease of implementation, ability to achieve wide tuning range, compact size, and

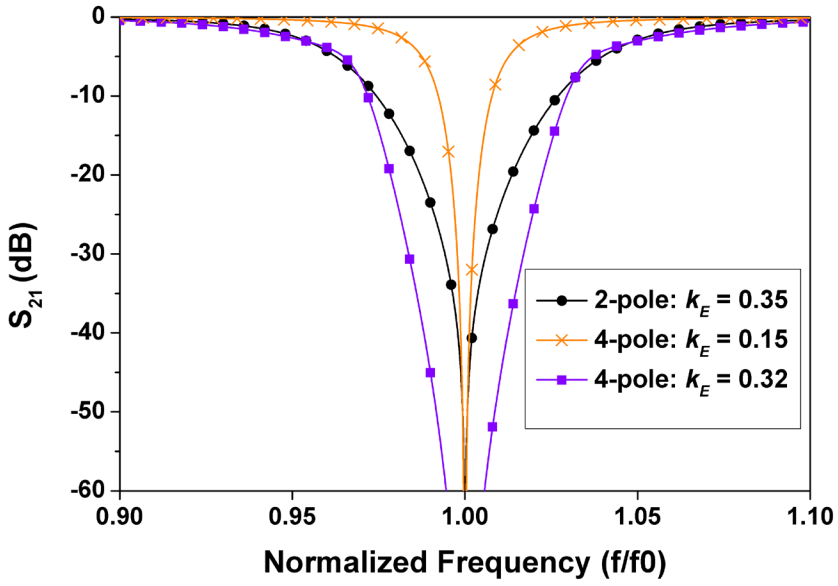

(a)

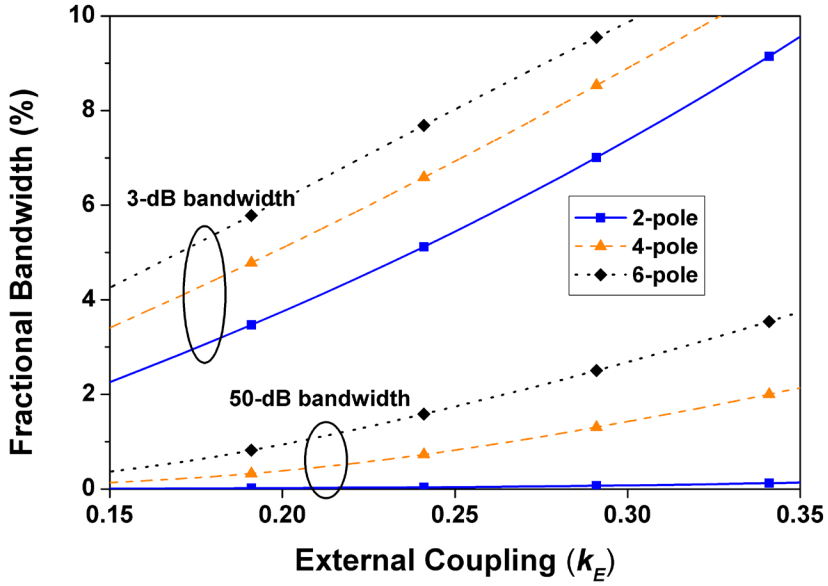

(b)

Fig. 2.12. (a) Comparison of 2-pole filter response with 4-pole response which have equal 3-dB bandwidth (purple trace) and equal 40-dB bandwidth (orange trace). (b) Comparison of bandwidths for 2-pole, 4-pole, and 6-pole filters. $Q_U = 100$, $\theta = 90^o$, and $k_{12} = 1/Q_U$ in both graphs.

wide spurious-free response. All filters were designed to operate over a 1.25 to 2.5 GHz tuning range. Filters A and B were designed to demonstrate that the required length of source-to-load through-line depends on the sign of the couplings as stated in Section II.B, and that using a nominally 90^o through-line results in a wider tuning range than using a

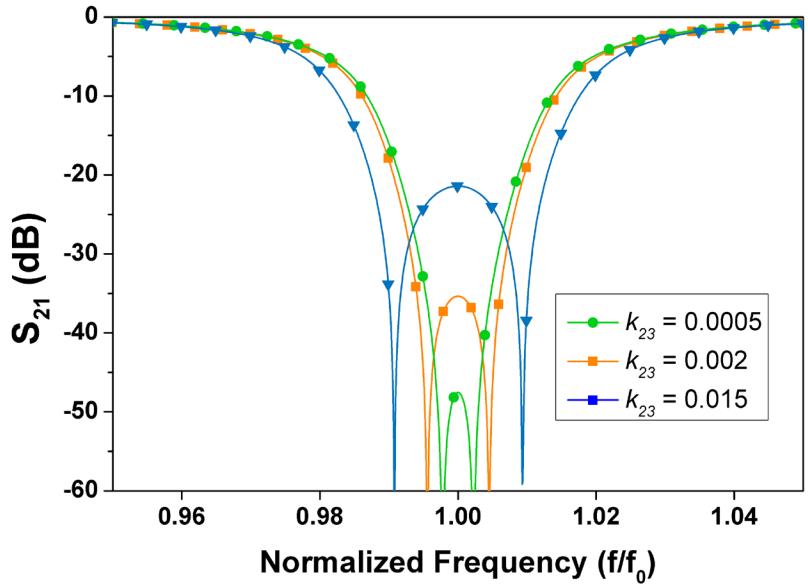

Fig. 2.13. Effect of parasitic inter-stage coupling (k_{23}) on filter performance. Even very small amounts of parasitic coupling can degrade filter performance by limiting the maximum achievable equiripple attenuation level.

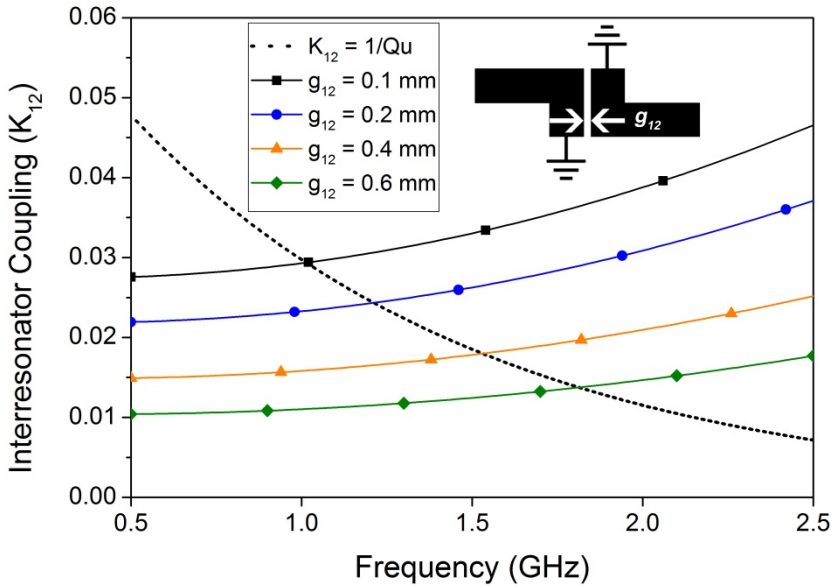

Fig. 2.14. Frequency dependence of interresonator coupling, extracted from electromagnetic simulations.

nominally 270° through-line. Filter A utilizes positive mutual inductance as interresonator coupling, which provides +90° insertion phase and thus requires a nominally 270° through-line. Filter B reverses the sign of interresonator coupling by

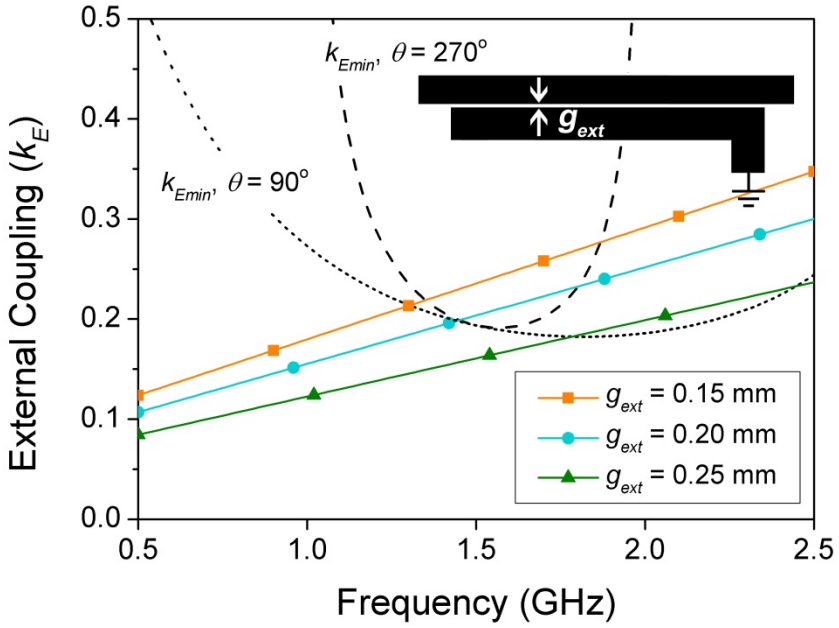

Fig. 2.15. Minimum required external coupling ($k_{E,min}$) and simulated external coupling values for different coupling gaps (g_{EXT}). For all frequencies where the actual value of k_E is greater than $k_{E,min}$, the filter can achieve an absorptive response. g_{12} = 0.15 mm.

reversing the position of the grounding via, and thus requires a nominally 90° through-line. The 3-dB bandwidths of Filter A and Filter B are equal: 5% at 1.5 GHz. Filter C utilizes a 90° through-line and is identical to Filter B with the exception of a narrower 3-dB bandwidth: 2.5% at 1.5 GHz. It illustrates the tradeoff between bandwidth and tuning range, as it has a narrower bandwidth and thus a smaller tuning range than the otherwise-identical Filter B. The fourth filter (Filter D) consists of two Filter Cs cascaded to form a four-pole filter, and illustrates increased selectivity with the penalty of reduced tuning range when compared to a 2-pole filter, as discussed in Section II.F. A detailed design procedure for Filter B is shown next. The design procedures for the other filters are omitted for brevity, but are essentially identical to the procedure used to design Filter B.

First, the varactors and the dimensions of the resonators were selected to yield the desired tuning range using a standard design procedure such as in [92]. MACOM MA46H202 GaAs hyperabrupt tuning varactors were chosen for their high Q_U and wide tuning range (0.6-6pF, Q_U = 2000 at 50 MHz). Using the information in the varactor's datasheet and electromagnetic simulation of the microstrip resonators, the unloaded

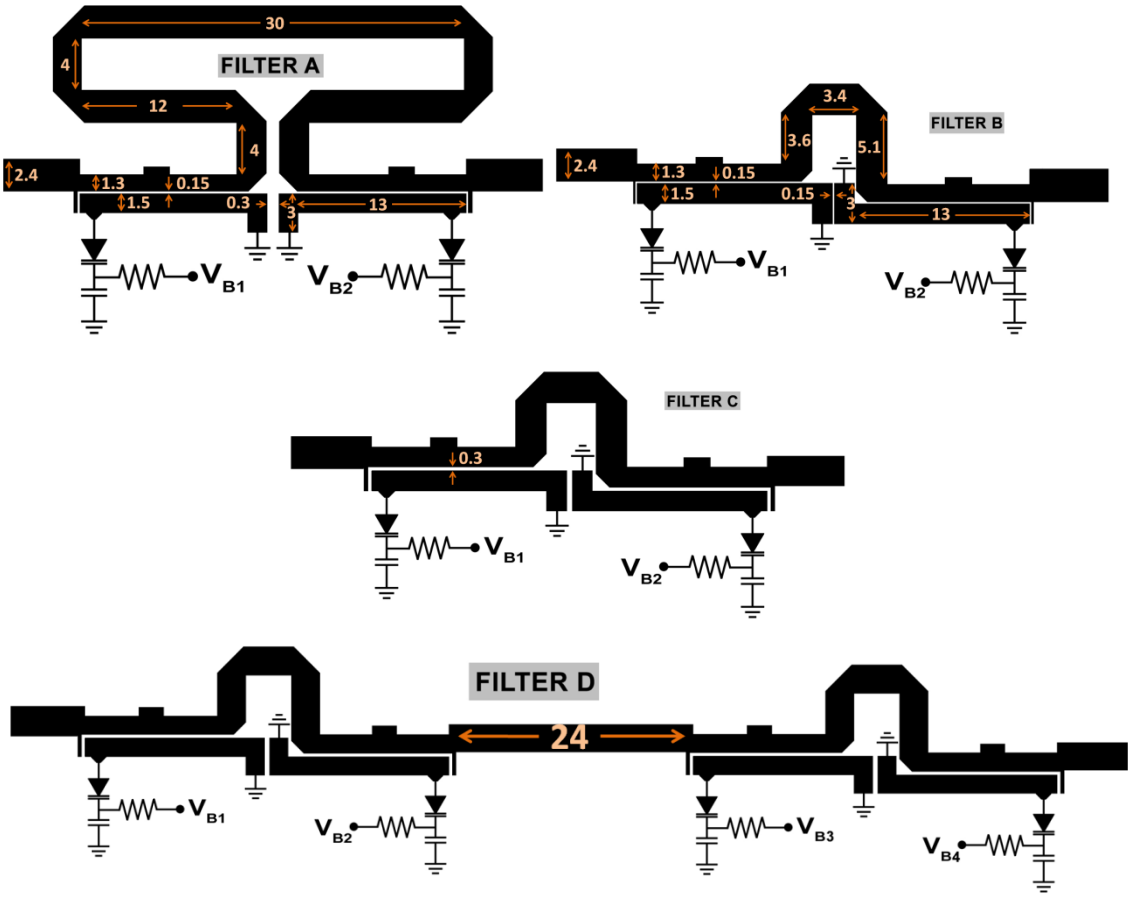

Fig. 2.16. Layout and dimensions of the designed filters. All dimensions are in millimeters. $V_{B1,2,3,4}$ denote the varactors' bias voltages.

quality factor was estimated at different frequencies in order to aid in choosing the interresonator coupling coefficient.

Design curves for interresonator coupling (k_{12}) versus frequency for different resonator spacings were calculated from electromagnetic simulation according to the method in [95] and are plotted in Fig. 2.14.The optimal value of k_{12} ($1/Q_U$) which allows for the minimum value of k_E was calculated using the estimated values of Q_U, and is also plotted in Fig. 2.14. It decreases with increasing frequency because of the frequency dependence of the resonator's unloaded quality factor, and it is clear that it has the opposite trend as the actual values of k_{12} which increase with frequency. Because smaller values of Q_U and k_E increase the design's sensitivity to the choice of k_{12} (see (2.31) and Fig. 2.5) k_{12} should be chosen such that it is equal to its optimal value at the lowest

frequency of the tuning range, where Q_U and k_E are the smallest. From the graphs in Fig. 2.14, the interresonator coupling gap g_{12} was initially chosen to be 0.25 mm in order to provide a coupling coefficient of 0.02 at 1.25 GHz, the optimal coupling coefficient for a resonator Q_U of 50. This serves as a starting point for fine tuning later in the design process.

The through transmission line length was initially chosen to be 29 mm long (90^o long at 1.9 GHz, the mid-point of the filter's tuning range), measured from the outside extremities of the resonators. Choosing the through-line to be 90^o at the center of the tuning range minimizes the deviation of its electrical length from a quarter wavelength, which is the required length of transmission line for a symmetric bandstop filter response [94]. This also serves as a starting point for fine tuning later in the design process.

Once the frequency-dependent values of Q_u and k_{12} are known and the transmission line length has been chosen, the minimum value of k_E required to obtain an absorptive response can be calculated from equation (2.29). Fig. 2.15 shows the minimum required values of k_E for nominally 90^o (Filter B) and 270^o (Filter A) through-lines, along with k_E extracted for several values of g_{EXT}. The method in Appendix A is used to extract k_E from simulations. Due to the frequency-dependence of k_{12}, k_E, and Q_U, the equation developed for calculating the tuning range (2.34) cannot directly be used. However, from these design curves the tuning range can be determined by noting the frequency range for which the simulated value of k_E is greater than the minimum required value of k_E. It is evident that in all cases the tuning range for a nominally 90^o through-line is greater than a nominally 270^o line for an equal k_E value, and that increasing k_E increases the tuning range.

Finally, the interresonator coupling gap g_{12} and the length of the through transmission line were fine-tuned in order to maximize the filter's tuning range by maximizing the range over which k_E was greater than k_{Emin}. It was found that due to the strong frequency dependence of k_E, the low end of the filter's tuning range was limited due to low values of k_E and Q_U, whereas there was no limit on the high end of the filter's tuning range because both k_E and Q_U were both much larger at these frequencies. The transmission line length was increased to 38 mm to further improve the lower limit of the

filter's tuning range, at the expense of slight asymmetry of the filter's transfer function at the upper end of its tuning range where the transmission line is significantly longer than the quarter wavelength required for a symmetric transfer function.

This design procedure is convenient in that it approaches the design of each design parameter individually, based on the design principles presented in this chapter. Each of these parameters can be evaluated without performing EM simulations of the entire filter, and minimal fine-tuning of the entire circuit is required at the end of this process. This is in contrast to the design procedures presented in [18], [24], which manually optimize the circuit without the guidance of clear design principles.

Using this design process, Filters A and B were designed with the same external coupling coefficient in order to have the same bandwidth (g_{EXT} = 0.15 mm, for a 3-dB bandwidth of approximately 5% at 1.5 GHz) and Filters C and D were designed with a smaller external coupling coefficient for a narrower bandwidth (g_{EXT} = 0.25mm, for a fractional bandwidth of approximately 2.5% and 3.5%, respectively, at 1.5 GHz). The final dimensions of all filters are shown Fig. 2.16.

The procedure for designing tunable absorptive bandstop filters with the minimum 3-dB bandwidth for a given tuning range can be summarized as follows:

1. Select resonators and tuning elements to cover desired frequency range, choosing a resonator topology for which the sign of $k_{E1}k_{E2}k_{12}$ is negative so that a 90^o through-line can be used.
2. Extract k_{12}-versus-frequency and Q_u-versus-frequency curves, and choose k_{12} to be equal to $1/Q_u$ near the lower end of the desired tuning range.
3. Plot $k_{E,min}$ calculated from (2.29) using frequency-dependent values of Q_u and k_{12}, choosing the through-line to be 90^o (or 270^o, as dictated by the coupling signs) near the center of the desired tuning range.
4. Extract k_E-versus-frequency curves, and choose the lowest value of k_E which is larger than the $k_{E,min}$ curve over the desired frequency range.
5. If necessary, fine-tune k_{12} and θ in order to maximize the filter's tuning range by using simulated k_E and calculated k_{Emin} curves, as in Fig. 2.14.

2.4 Experimental Validation

The filters were fabricated on 0.787-mm thick Rogers RT/Duroid 5880 substrate (ϵ_r = 2.2, tanδ = 0.0009), and measured using a Keysight N5230C PNA. The varactors were biased between 4 and 22 V using a Keysight N6705B voltage source. A photograph of Filters A, B, and D is shown Fig. 2.17.

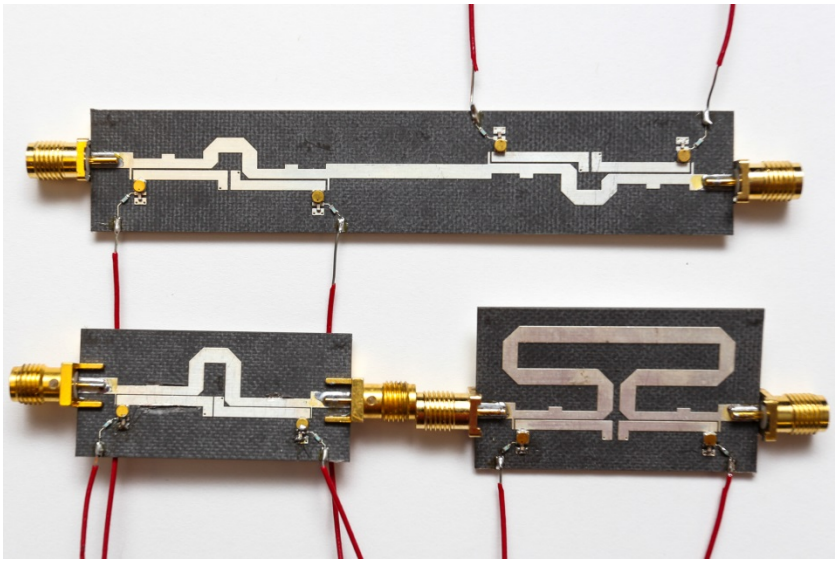

Fig. 2.17. Photograph of fabricated filters.

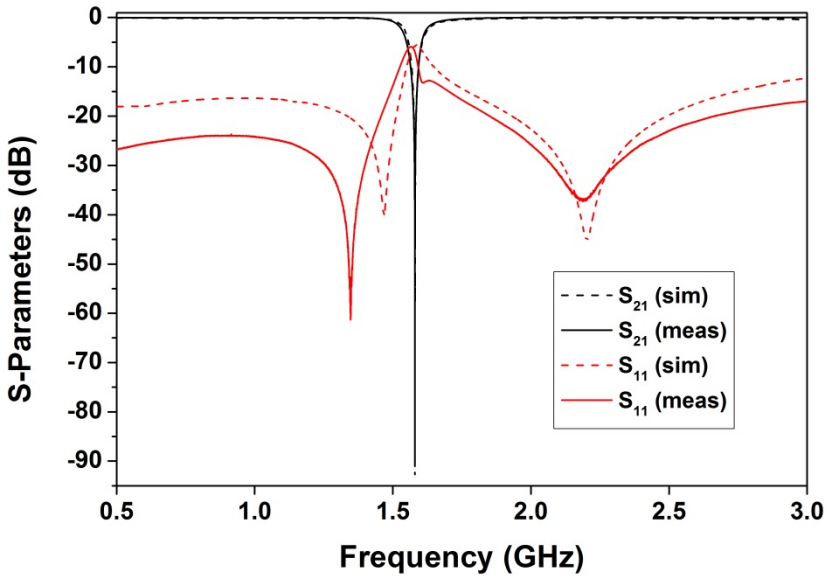

Fig. 2.18. Simulated and measured response of Filter B when tuned to 1.6 GHz.

Fig. 2.18 shows the measured frequency response of Filter B tuned to 1.6 GHz, illustrating its high-attenuation stopband and well-matched, low-loss passband. It has less than 0.2 dB passband insertion loss up to 3 GHz. As expected, the filter is able to achieve very high attenuation in its stopband (over 90 dB), although the bandwidth at high levels of attenuation is limited. Fig. 2.20 shows the measured attenuation plotted versus offset from the filter's center frequency. The filter has a 4.9% 3-dB bandwidth, 1.8% 10-dB bandwidth, 0.15% 30-dB bandwidth and 0.0015% 70-dB bandwidth. The measured attenuation is limited by the noise floor of the network analyzer, which is also plotted in Fig. 2.20.

In order to verify the design principles of Section II and the design procedure of Section III, the measured responses of each of the filters when tuned over their entire tuning ranges are shown in Fig. 2.21. As expected from the theory in Section II.D, Filter B has a wider tuning range than Filter A due to its use of a nominally 90^o instead of 270^o through-line (1.45:1 versus 1.27:1). Additionally, Filter B also has a wider tuning range than Filter C due to its larger bandwidth (1.45:1 versus 1.24:1). The high-attenuation tuning range of each filter is smaller than designed because the quality factors of the varactors used were much lower than specified in the datasheets. The extracted quality factor of the varactors varied from 34 to 87 between 1 and 2 GHz, compared to the Q_U of 77 to 220 specified in the datasheet. When the extracted value of varactor Q_U and the slight fabrication dimensional errors are taken into account, the measured results match simulation very well in Fig. 2.21.

The performance of the four-pole filter (Filter D) is compared to that of the wide-bandwidth two-pole filter (Filter B) in Fig. 2.22. Their 10-dB bandwidths are identical, and the four-pole filter has increased selectivity as expected. However, as noted in Section II.F, the maximum attenuation of Filter D is maintained over a narrower tuning range than Filter B (1.9 to 2.3 GHz, as compared to 1.59 to 2.3 GHz) because a smaller value of k_E is needed to obtain the same 10-dB bandwidth. Additionally, Filter D had a higher level of passband insertion loss than did Filter B (0.55 dB compared to 0.2 dB at 3 GHz) due to the longer lengths of transmission lines used.

The two bias voltages required to tune Filter B are shown in Fig. 2.23. The two bias voltages are nearly identical across the whole tuning range. Also shown in Fig. 2.23 is the

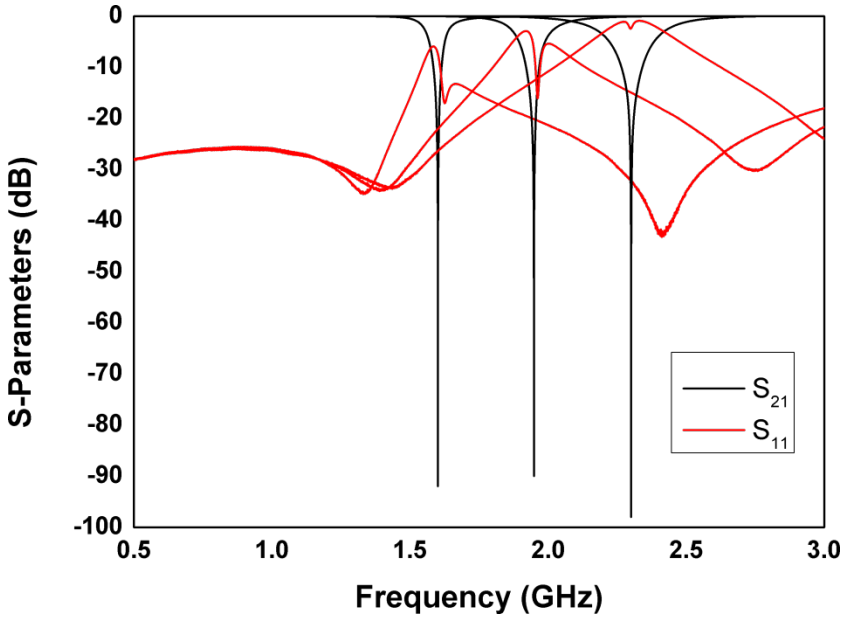

Fig. 2.19. Measured response of Filter B, showing that it can provide > 90 dB of stopband rejection over a 1.5 to 2.3 GHz tuning range.

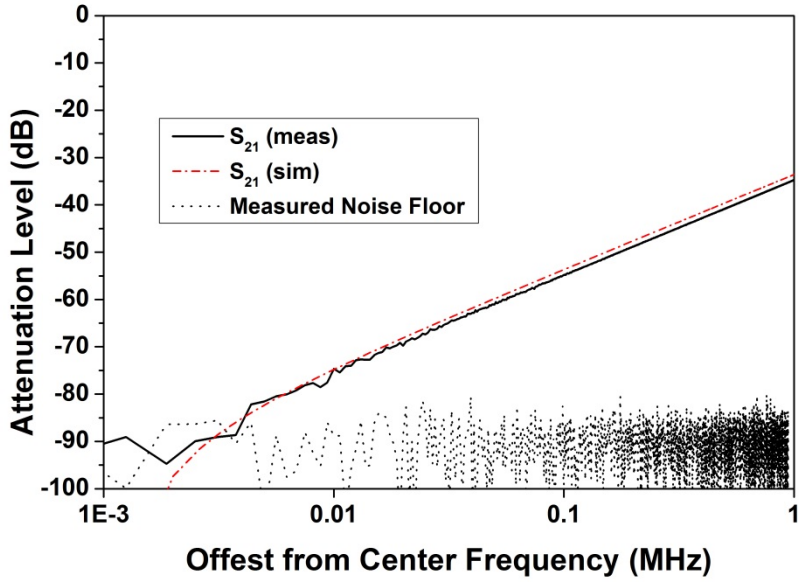

Fig. 2.20. Measured attenuation in stopband of filter.

frequency offset between the two resonators across its tuning range. It can be seen that at and below the lower limit of the filter's high-attenuation tuning range (~1.585 GHz), the frequency offset is zero and the resonators are synchronously tuned. Above this lower limit, the resonators are asynchronously

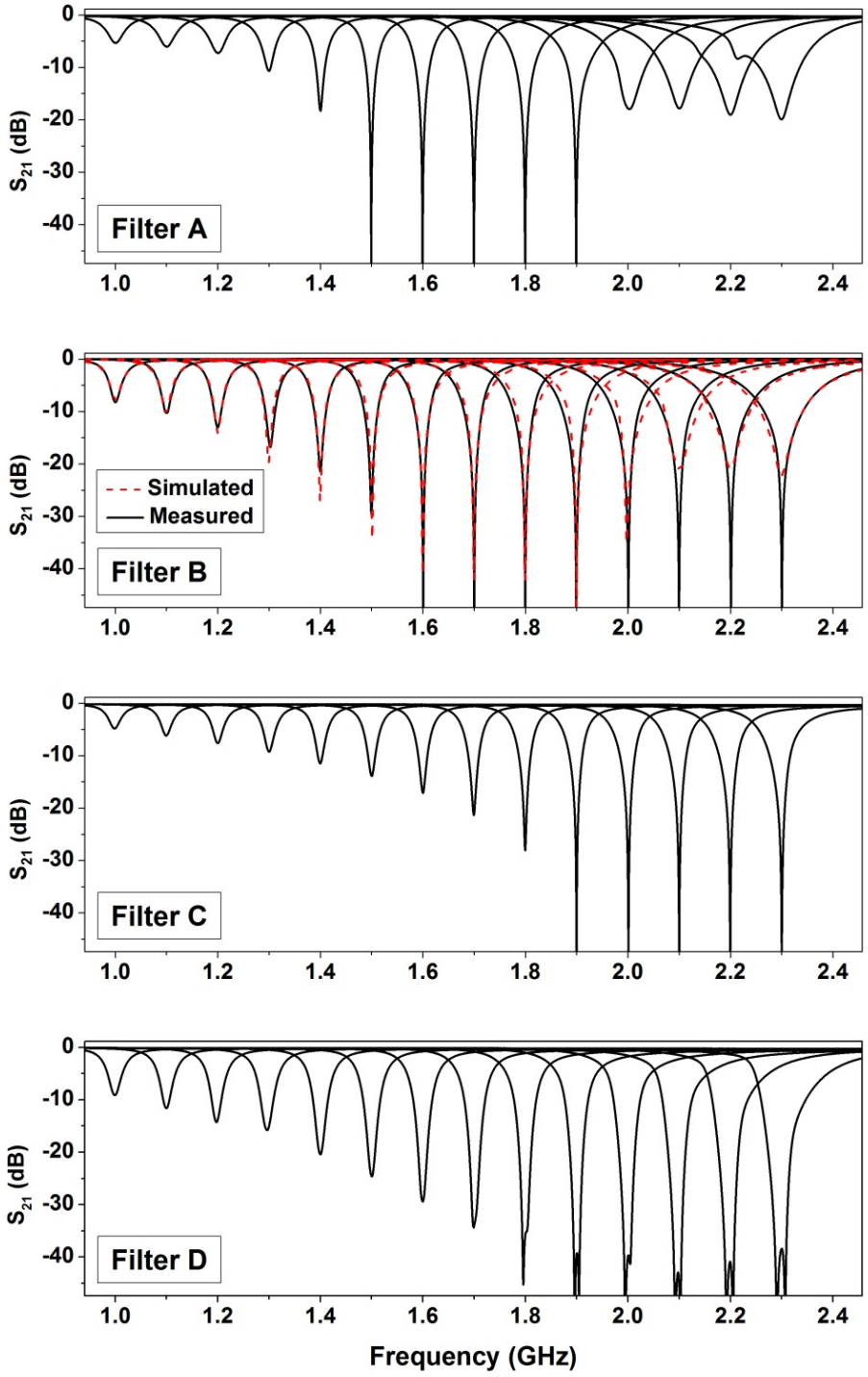

Fig. 2.21. Measured transmission responses of all filters tuned across their frequency ranges.

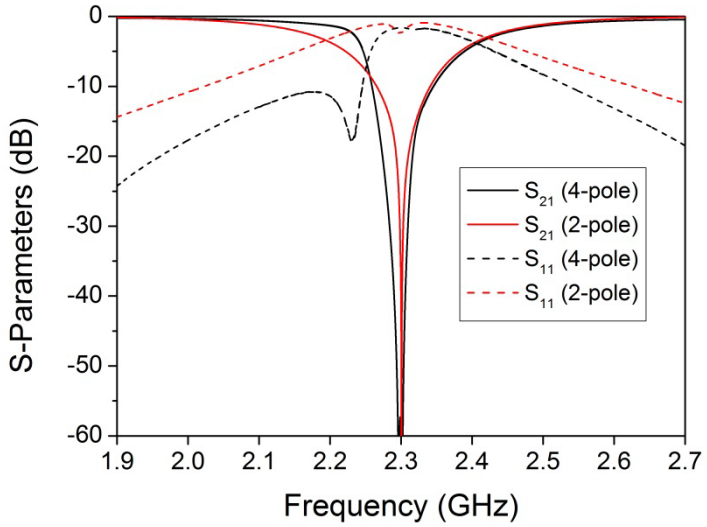

Fig. 2.22. Comparison of two- and four-pole filters. The four-pole filter exhibits greatly increased selectivity, but does not maintain high attenuation over as large of a frequency range as the two-pole filter.

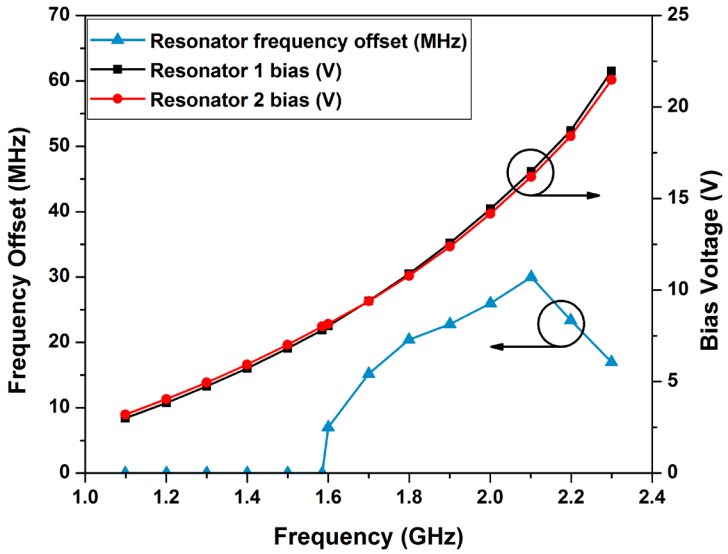

Fig. 2.23. Plot of varactor bias voltages versus center frequency, and resonator frequency offset versus center frequency. At and below the lower limit of the filter's high-attenuation tuning range, the resonator offset is zero and the resonators are synchronously tuned. Above this lower limit, the resonators are asynchronously tuned to achieve large stopband attenuation.

tuned in order to realize high levels of stopband attenuation. This is in agreement with the analysis of Section II, in which it was asserted that the frequency offset between the resonators was zero (B = 0) at the limits of the filter's tuning range, and that the resonators would be asynchronously tuned (B ≠ 0) between the upper and lower limits of

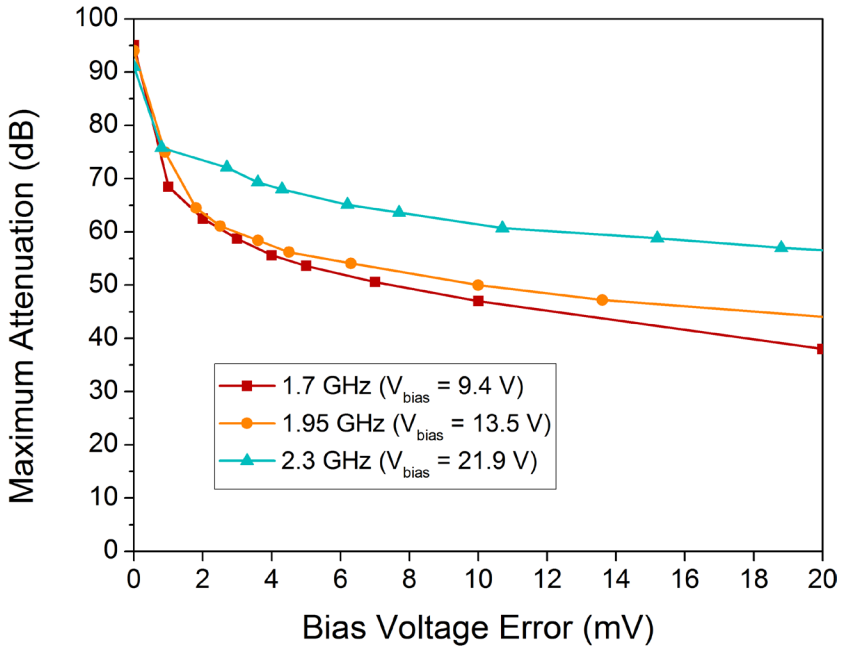

Fig. 2.24. Effect of error in bias voltage on filter attenuation. Measurements are when filter is tuned to 1.7 GHz, with nominal varactor biases of 9.4 V, 12.5 V, and 21.9 V.

the filter's tuning range. The maximum frequency offset between the resonators is 30 MHz, or 1.4% at 2.1 GHz.

Lastly, the sensitivity to variations in tuning voltage is examined. Although the filters are able to achieve extremely high levels of stopband attenuation when correctly tuned, errors in tuning voltage will degrade this response. Fig. 2.24 plots the maximum stopband attenuation versus tuning voltage error for 1.7, 1.9, and 2.3 GHz center frequencies. The sensitivity of stopband rejection to error in tuning voltage decreases as the filter's center frequency is increased. This is to be expected, since a varactor's capacitance becomes less sensitive to change in bias voltage as its bias voltage is increased, due to the nonlinear C-V curve of the varactor. It can be noted that at its most sensitive state (1.7 GHz), the maximum attenuation is greater than 50 dB when the tuning voltage error is less than 7 mV. If this voltage error is split between the two varactors, then the required precision for the tuning voltage is 3.5 mV. Considering that the maximum tuning voltage is 22 V, 3.5 mV equates to 13 bits of precision. Using the capacitance versus voltage curves of the varactors, this 3.5 mV precision can alternatively be interpreted as a capacitance precision of 0.55 fF.

2.5 Conclusion

In this chapter, a detailed analysis of absorptive bandstop filters has been performed, in which theory and simulations are used to derive and demonstrate their operating principles, design considerations, performance tradeoffs, and limitations.

A simple but general step-by-step design procedure has been proposed for the first time, taking into account non-ideal effects such as frequency-dependent couplings and quality factors. The theory and design principles derived are generic and not specific to a given technology, and thus can be used to design a wide variety of absorptive bandstop filters. Several varactor-tuned microstrip filters have been designed to demonstrate the design principles and tradeoffs derived in the chapter. A comparison is made between filters with different coupling structures and bandwidths to illustrate their effects on tuning range, and the performance of a two-pole filter is compared to that of a four-pole filter to show its increased selectivity. The filters designed and demonstrated are able to achieve very high levels of stopband isolation (> 90 dB), over as wide as a 1.45:1 tuning range.

3. TUNABLE MILLIMETER-WAVE BANDSTOP FILTERS

3.1 Introduction

Recent advances in millimeter-wave components such as antennas, LNAs, and power amplifiers, have made functional radar and communication systems possible at Ka through W-band frequencies. An important characteristic of robust communications systems is the ability to operate in the presence of strong, unpredictable interfering signals, but this often requires the use of dynamic filtering to prevent sensitive front-end components such as high-gain LNAs from saturating. There are multiple ways to achieve this, but one promising method is to place a tunable narrowband, high-isolation bandstop filter in front of an otherwise wideband receiver. Key characteristics of such a filter are low-loss in the passband, high levels of isolation in the stopband, high selectivity (narrow passband to stopband transition), and wide tuning range. This chapter proposes both Ka-band and W-band bandstop filters which exhibits these qualities.

3.2 Tunable W-Band Bandstop Filter

3.2.1 Concept

The simplest two-pole bandstop filter configuration consists of two parallel resonators in shunt configuration coupled to a source-to-load transmission line at an interval of an odd multiple of 90-degree length of transmission line. This topology relies on the constituent resonators' reactance to reflect incident signals in the filter's stopband. When losses in the resonator are considered, the maximum achievable amount of stopband isolation is limited, and depends the quality factor of the resonators used and the bandwidth of the filter.

Although tunable resonators with relatively high quality factors have been demonstrated, it is still usually not possible for tunable bandstop filters to achieve very

high levels of attenuation (>50 dB) with narrow bandwidths (< 3% fractional bandwidth). One technique to overcome the limitations of limited resonator quality factor is to add a small amount of interresonator coupling between the two resonators. By following the design principles outlined in Chapter 2, it is possible to achieve theoretically infinite attenuation even with finite-quality-factor resonators (see Fig. 3.1). This type of filter has been referred to as "absorptive" bandstop filters in literature [23], [45].

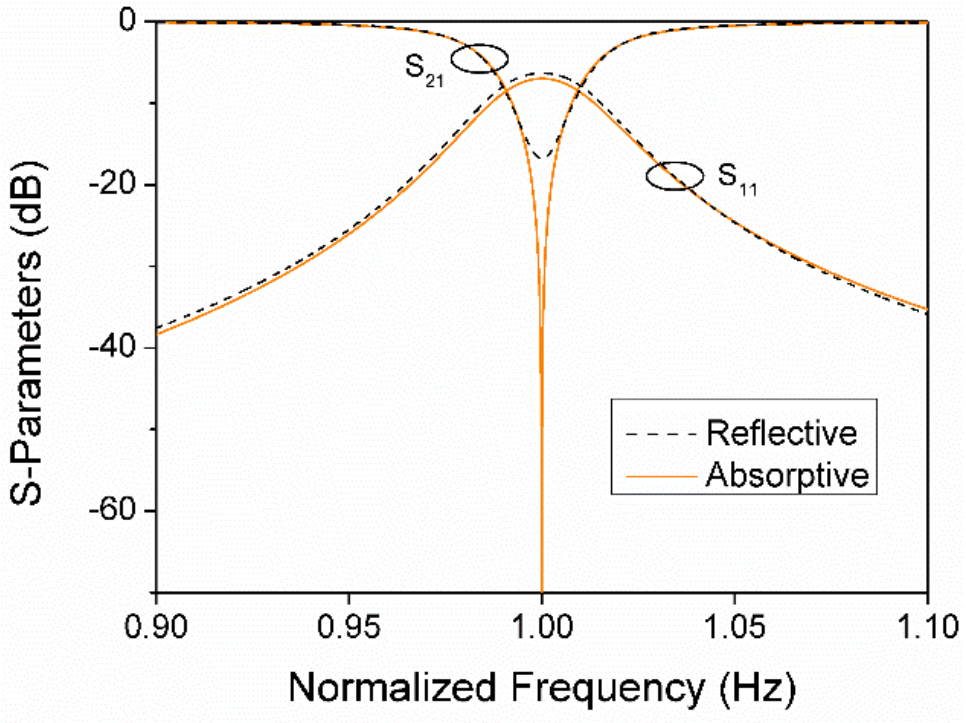

Fig. 3.1. Comparison of reflective and absorptive bandstop filters. Q = 75 in these simulations.

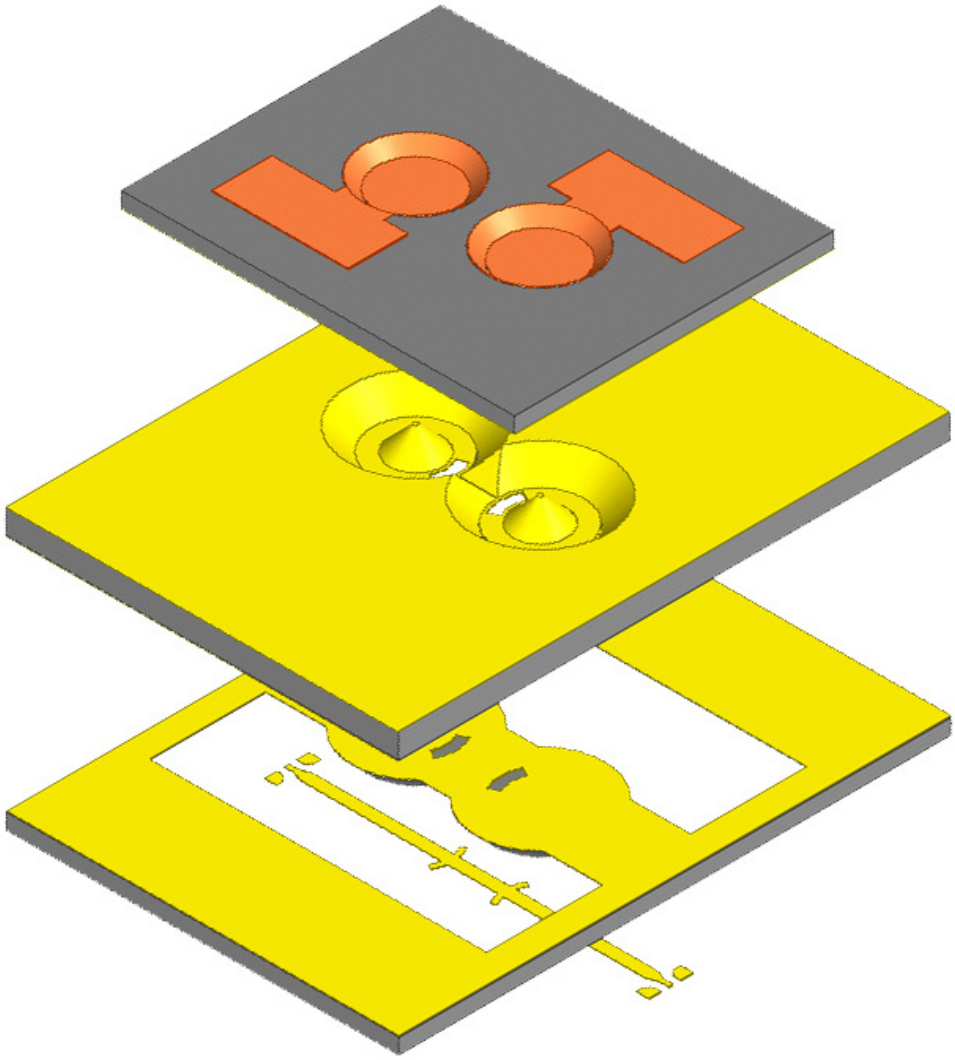

Fig. 3.2. Conceptual drawing of proposed W-band tunable bandstop filter. The top element is a MEMS electrostatic actuator, the middle element is the cavity substrate, and the bottom element is the signal substrate.

It is interesting to note that with this topology, the maximum attenuation of the filter is not limited by the quality factor of the resonators, but the minimum bandwidth is. The external coupling must be at least $\sqrt{2/Q}$, which limits the minimum possible 3-dB fractional bandwidth to 2/Q [96].

3.2.2 Design

In order to implement a high-isolation tunable bandstop filter at W-band frequencies, we propose a two-pole absorptive bandstop filter based on evanescent-mode cavity

resonator technology. Evanescent-mode cavity resonators are widely-documented in literature [71], [74], [97], and are resonant cavities which are capacitively loaded by inserting a post in the center of the cavity which forms a parallel-plate capacitance between the tip of the post and the ceiling of the cavity. If the ceiling of the cavity can be moved, such as by a piezoelectric or MEMS electrostatic actuator, this loading capacitance can be changed and thus the frequency of resonance can be tuned. A conceptual drawing of the proposed bandstop filter is shown in Fig. 3.2.

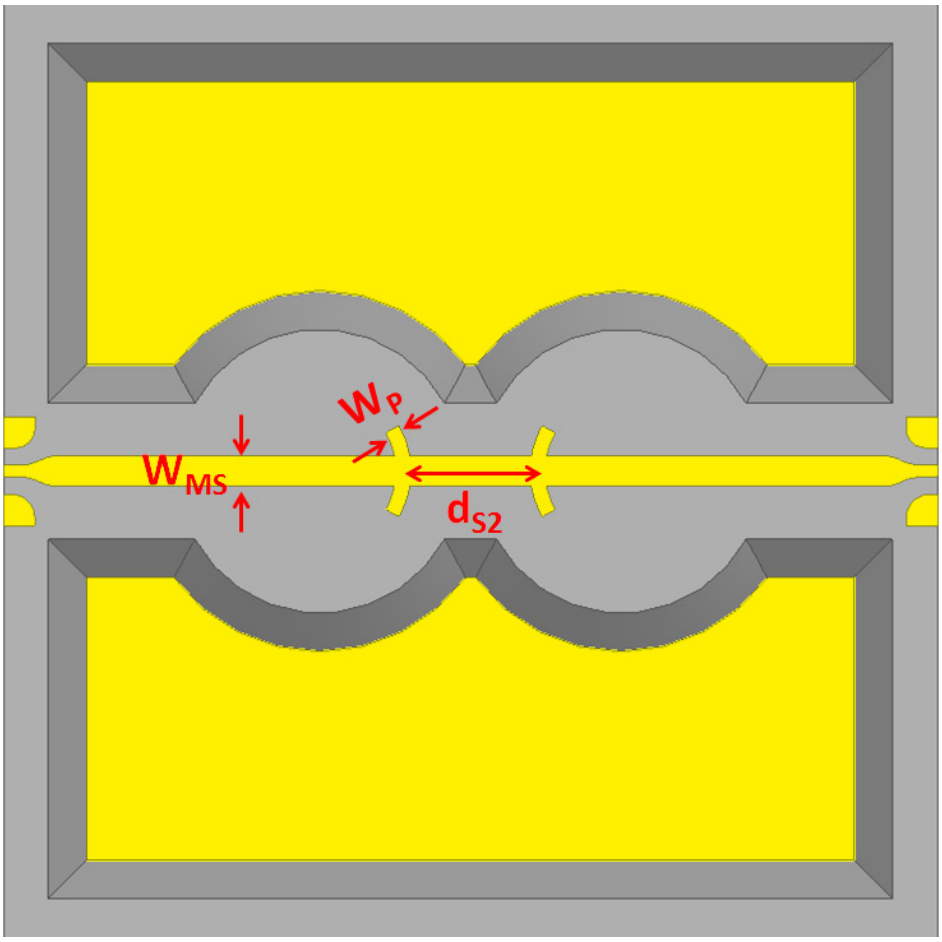

Fig. 3.3. Signal-side of cavity substrate. WMS = 155 µm, WP = 60 µm, ds2 = 710 µm

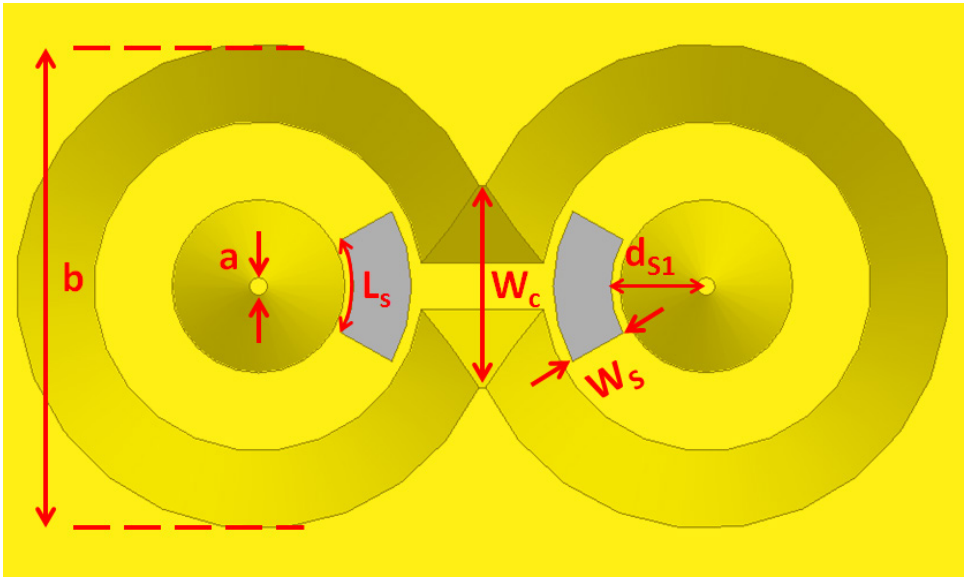

Fig. 3.4. Cavity-side of cavity assembly. b = 1.68 mm, a = 60 µm, LS = 340 µm, WC = 500 µm, W_S = 180 µm, ds1 = 330 µm.

The evanescent-mode resonators are realized with gold-plated wet-etched silicon cavities each containing a conical post in the center. This structure approximates a short length of coaxial transmission line loaded with a capacitance, and has been proven to yield tunability and high Q at frequencies up to 80 GHz [83]. The source to load coupling is realized with a 270 degree microstrip transmission line on a high-resistivity silicon substrate, with apertures in the ground plane which implement the external coupling by allowing a portion of the transmission line's magnetic field to couple with the magnetic field of the cavity at resonance. The interresonator coupling is created by introducing an iris between the two resonators, coupling the magnetic fields of the two resonators.

The strength of the external coupling is determined by both the width and length of the coupling aperture, and can be extracted from the S-parameters obtained from full-wave EM simulations according to [98]. The size of the coupling apertures was chosen to be 0.18 mm x 0.34 mm, yielding a coupling coefficient K_{ext} = 0.13 at 95 GHz in order to realize a 1.5% 3 dB fractional bandwidth notch.

The apertures in the ground plane present series inductance to the through transmission line, which can seriously degrade the passband performance of the filter. This effect can be mitigated by adding capacitive patches to the transmission line directly

over the ground plane apertures [55]. However, this combination of series inductance and shunt capacitance adds a significant phase shift to the through-line which must be taken into account when designing the through transmission line. Using 3D EM simulations to determine the actual phase of the through-line including the phase shift from the coupling apertures, the distance between the two coupling apertures was chosen to be 0.71 mm so that the total phase shift between coupling slots (center to center) was 270 degrees at 95 GHz.

It was observed through 3D EM simulations that above 100 GHz, a significant amount of power was leaked to parasitic propagating surface modes. To mitigate this problem and reduce passband insertion loss, the substrate on either side of the microstrip line was etched away, preventing the propagation of these spurious modes.

The inter-resonator coupling is realized with an inductive iris, which is essentially a section of below-cutoff waveguide which allows the magnetic fields of the resonators to couple with each other at resonance. Increasing the width of the coupling iris increases the strength of the coupling, as does reducing the spacing between the resonators. Because the resonator spacing was fixed after choosing the length of the through transmission line, the only free variable was the width of the coupling iris. The resonator quality factor was estimated to be 400 from HFSS simulations, and thus the desired interresonator coupling value was $1/Q_U = 0.0025$. The coupling iris width was chosen to be 0.5mm in order to attain this coupling value.

3.2.3 W-Band Bandstop Filter Fabrication and measurements

The 200-µm high-resistivity silicon substrate used for the signal substrate was bonded to a 300-µm silicon substrate using a gold intermediate layer, and the cavities were wet-etched using a TMAH and Triton X-100 solution [99]. The cavity and transmission lines were metalized and patterned with a 1 µm layer of sputtered gold.

The tuner's bias electrodes were created by wet-etching cavities in the backside of the tuner substrate, which were then electroplated with a thick layer of copper. The

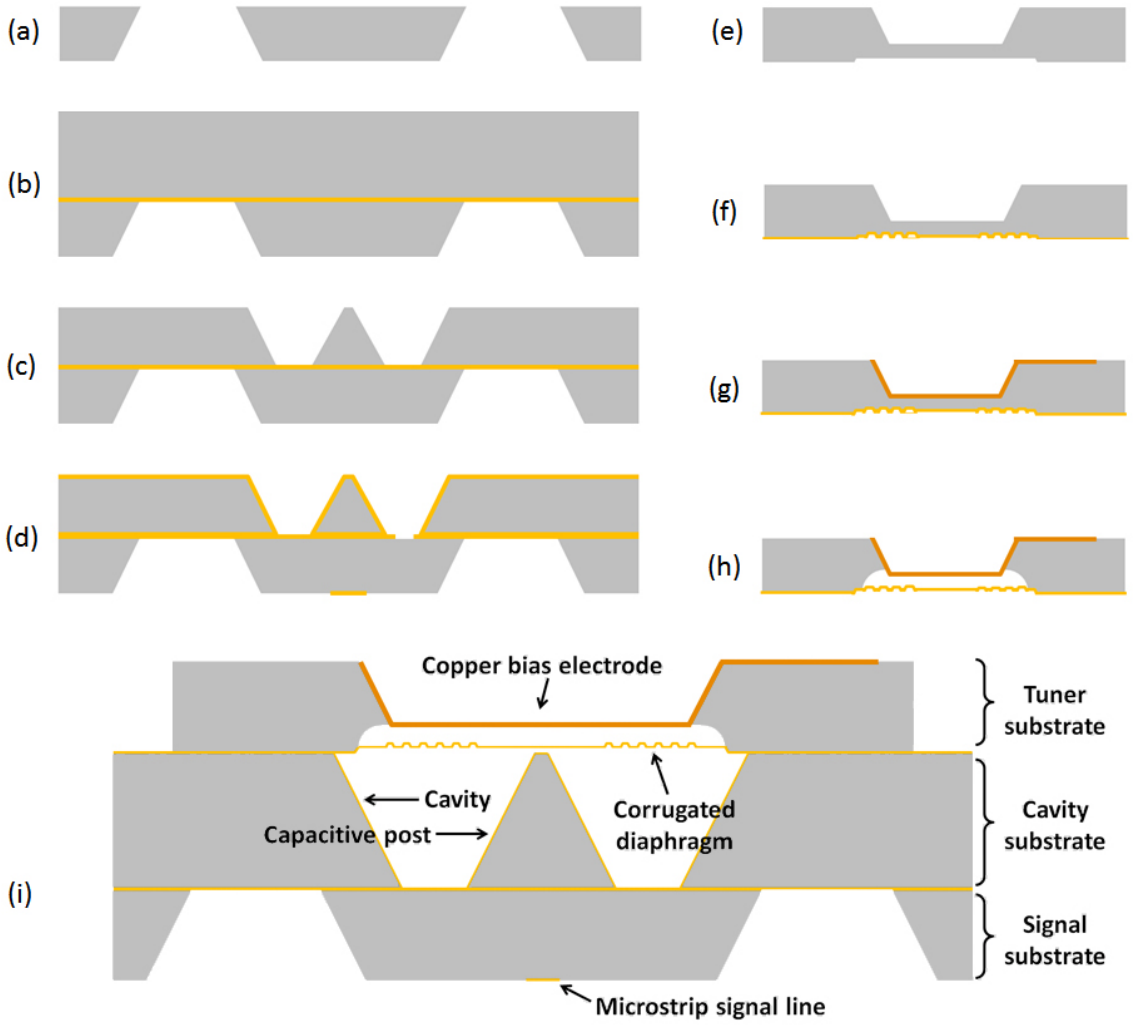

Fig. 3.5. Fabrication steps. (a) Etch signal substrate to suppress surface waves. (b) Bond etched substrate to cavity substrate (gold-gold thermocompression bonding). (c) Etch cavities using gold layer as etch stop. (d) Metalize and pattern cavities and microstr

corrugated diaphragm was created by etching circular corrugations in the silicon substrate, metalizing the corrugations, then etching the silicon from under the diaphragm using XeF_2 dry-release process to leave a flexible, free-standing diaphragm.

After release, the tuner was aligned and bonded to the cavity structure using gold-to-gold thermocompression bonding. SEM images of the fabricated device are shown in Fig. 3.6.

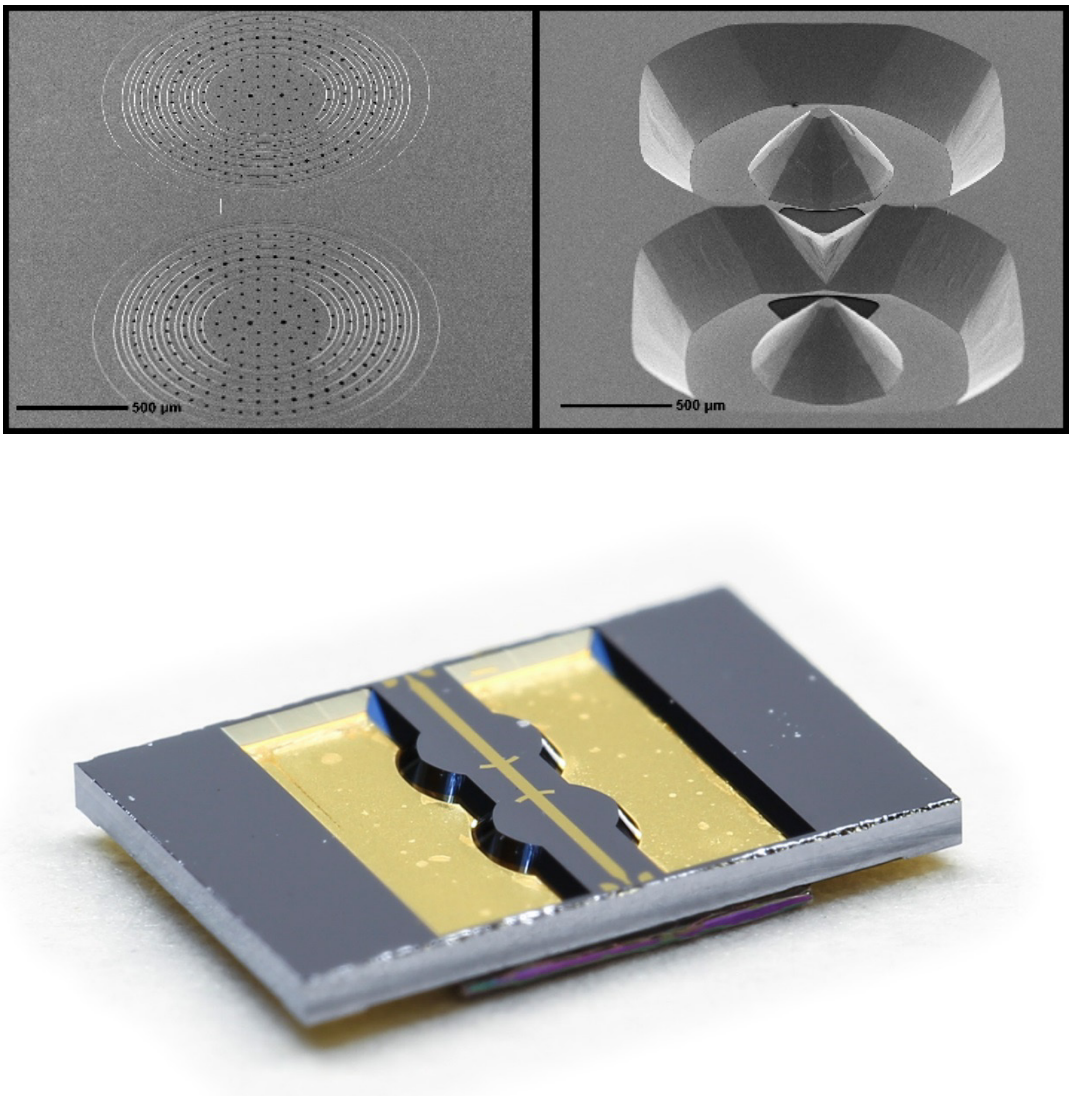

Fig. 3.6. SEM images of fabricated device. (top left) Corrugated tuner diaphragm. (top right) Cavities with capacitive posts and coupling apertures. (bottom) Photograph of assembled filter.

The assembled structures were measured using an Agilent E8361 precision network analyzer with a millimeter-wave extension head and Cascade Infinity RF probes, and the filters were appropriately biased using Keithley 2440 power supplies. In all measurements, TRL calibration was performed to bring the measurement reference plane to the tips of the measurement probes.

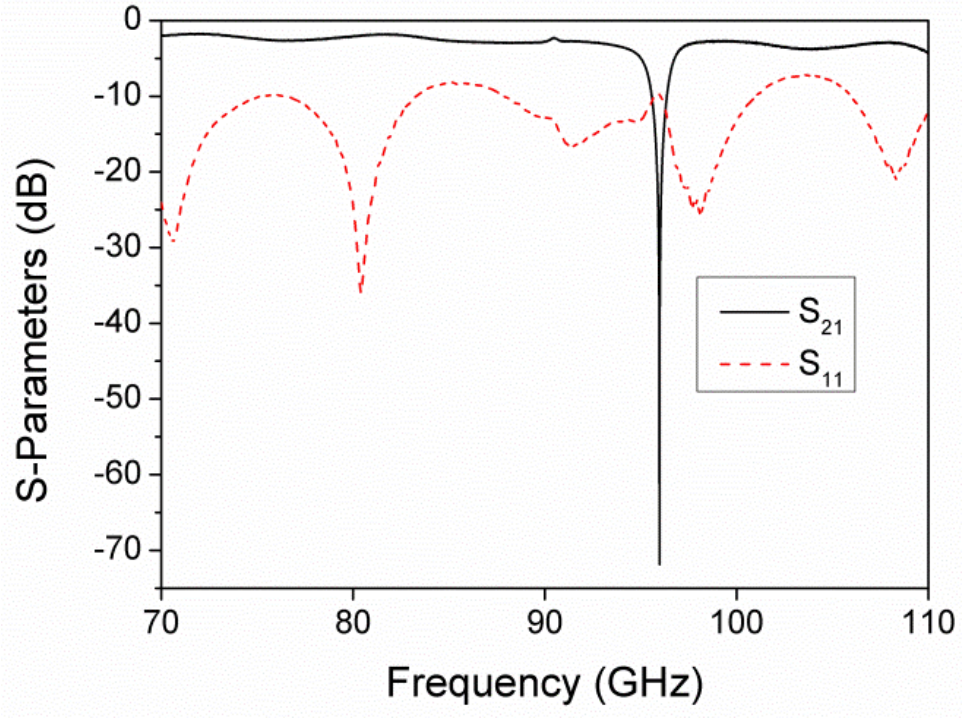

Fig. 3.7. Measured response of the W-band bandstop filter, exhibiting > 70 dB notch depth and < 3.25 dB passband insertion loss up to 109 GHz.

Fig. 3.7 shows the measured response of a filter tuned to 96 GHz. Its notch depth is greater than 70 dB, and the passband insertion loss varies from 1.7 dB at 71 GHz to 3.25 dB at 109 GHz. The relatively high passband return loss (~8 dB) is due to parasitic reactances caused by the CPW to microstrip transition required to measure the device with RF probes. From simulations, the return loss of the filter itself would be better than 15 dB across the passband if the effects of the transition were removed.

The measured responses of two assembled filters are shown in Fig. 3.8. The two filters are identical in all respects except for the initial gap between the tuning diaphragm and the post tip. The first filter has a capacitive gap which ranges from 3-10 μm, and the second filter has a gap which ranges from 6-13 μm. The first filter has an analog tuning range of 75-103 GHz with an applied bias of 0-90 V. The second filter tunes from 96-108 GHz with 0-80 V applied bias. Below 90 GHz, the filters are not able to obtain deep notches because the through-line is no longer 270 degrees and the phase relationship

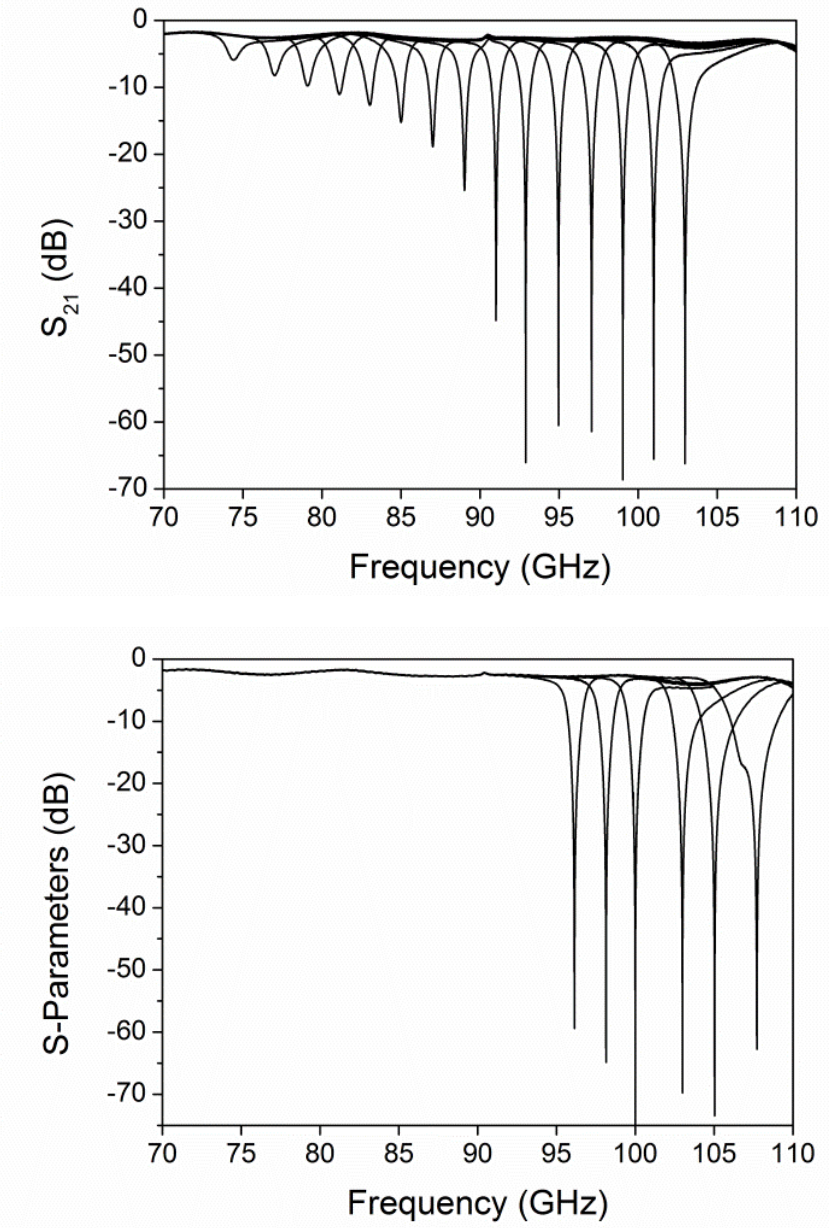

Fig. 3.8. Performance of the measured filters. (a) Filter with 3-10 μm tuning gap covering 75-103 GHz. (b) Filter with 6-13 μm tuning gap covering 96-108 GHz.

which is required for absorptive operation is no longer present. The unloaded quality factor of the resonators was extracted to be 290 and the filters had a 1.5% 3-dB fractional bandwidth (calculated after deembedding the passband insertion loss) at 95 GHz.

3.3 Ka-band Tunable Bandstop Filter

3.3.1 Concept

The Ka-band filter was designed to be intrinsically-switched, so that the tunable notch could be deactivated if necessary to leave a low-loss passband. A schematic diagram illustrating a resonator with intrinsically-switched coupling is shown in Fig. 3.9. The structure consists of a resonator with two external coupling elements, separated by a transmission line of electrical length θ [19].

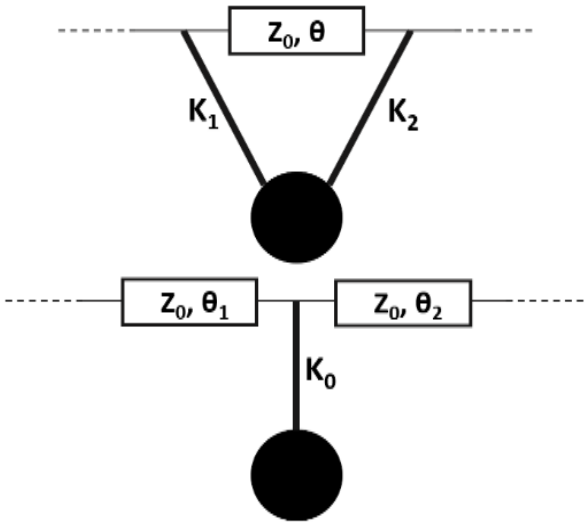

Fig. 3.9. (top) Topology of an intrinsically-switched resonator. (bottom) Equivalent circuit.

This structure can be represented by a resonator with a slightly offset center frequency and only a single (but frequency-dependent) coupling with transmission lines of lengths θ_1 and θ_2 preceding and following the coupled resonator. If $K_2 = -K_1$, the effective coupling coefficient and phase lengths are given by

$$K_0 = K_1\sqrt{2 - 2\cos\theta} \tag{3.1}$$

$$\theta_2 = \theta_1 = \frac{\theta}{2}. \tag{3.2}$$

If the resonator is tunable, then the resonator can be tuned to the frequency at which θ is 360^o which yields a coupling coefficient of zero, isolating the resonator from the through-line and creating an all-pass response.

The preceding concepts are combined to create a 20-40 GHz intrinsically-switched absorptive bandstop filter.

3.3.2 Design

The external coupling elements are implemented as ground-plane coupling apertures on either side of the cavity. From (3.3) it is evident that the total coupling of the intrinsically-switched topology coupling is greater than that of a single coupling element for values of θ between 60^o and 300^o. Through full-wave electromagnetic simulations, the coupling aperture size was chosen to be 0.85 mm x 0.25 mm to yield a total external coupling coefficient of 0.23 at 30 GHz and a 3-dB fractional bandwidth of approximately 5%.

The interresonator coupling is realized with a below-cutoff waveguide iris which allows the magnetic fields of the resonators to couple with each other. The simulated quality factor of the resonators is approximately 400, and thus the desired interresonator coupling coefficient is 0.0025. A cavity spacing of 3.3 mm and a coupling iris width of 1.6 mm yields this coupling coefficient at 30 GHz.

The filter is designed to have an intrinsically-switched all-pass state when the resonators are tuned 43 GHz, requiring a transmission line between the coupling elements which is 360^o at 43 GHz. This has a phase length of approximately 250^o at 30 GHz, the center of the filter's tuning range, which must be absorbed into the nominally-90^o length of transmission line used in the absorptive filter. A 90^o through-line cannot absorb the 250^o provided by the intrinsic-switching through-lines, so the next longer possible line length of $90^o + 360^o = 450^o$ must be used. Therefore an additional $450^o - 250^o = 200^o$ of transmission line must be added between the intrinsically-switched resonators. This

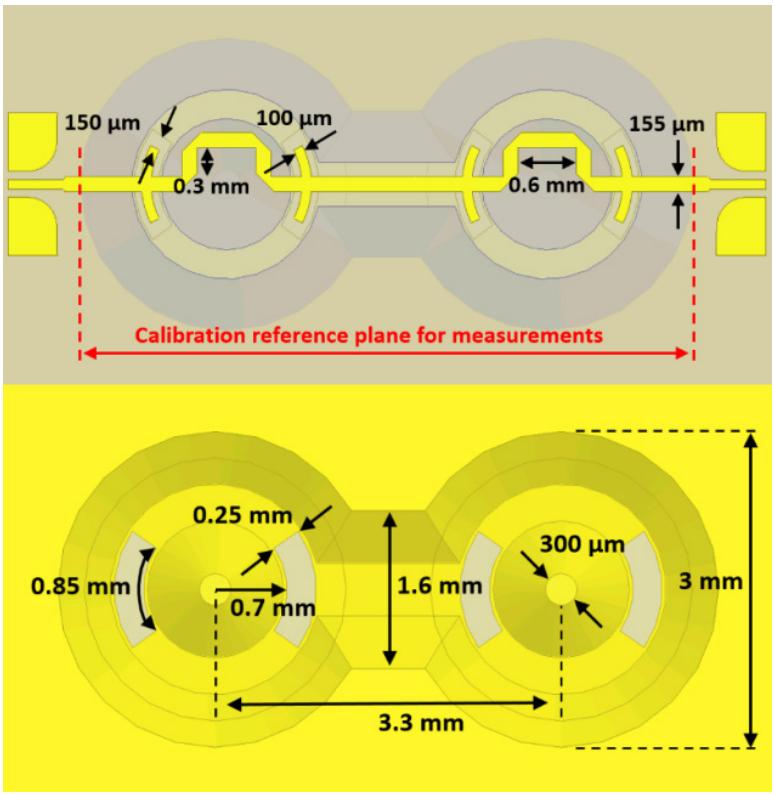

Fig. 3.10. Dimensions of (top) signal-side of substrate, and (bottom) cavity side of substrate.

phase length is obtained by choosing the spacing of the resonators to be 3.3 mm. The final dimensions of the filter are shown in Fig. 3.10.

3.3.3 Ka-Band Filter Measurements

The filter was fabricated using same process as in Fig. 3.5. SEM images and a photograph of the assembled filter are shown in Fig. 3.6.

The assembled filter was measured using an Agilent E8361 precision network analyzer with Cascade Infinity measurement probes. The effects of the probes and the CPW-to-microstrip transitions were removed using TRL calibration. Fig. 3.12 shows the filter when tuned to 30 GHz, as well as the filter in its all-pass state. The filter has > 60 dB notch depth with a 4.5% 3-dB fractional bandwidth, and has a passband with < 1.1 dB insertion loss up to 42 GHz. In its all-pass state, the filter has less than 1.1 dB of insertion loss and better than 15 dB return loss up to 42 GHz, and less than 2 dB insertion loss and

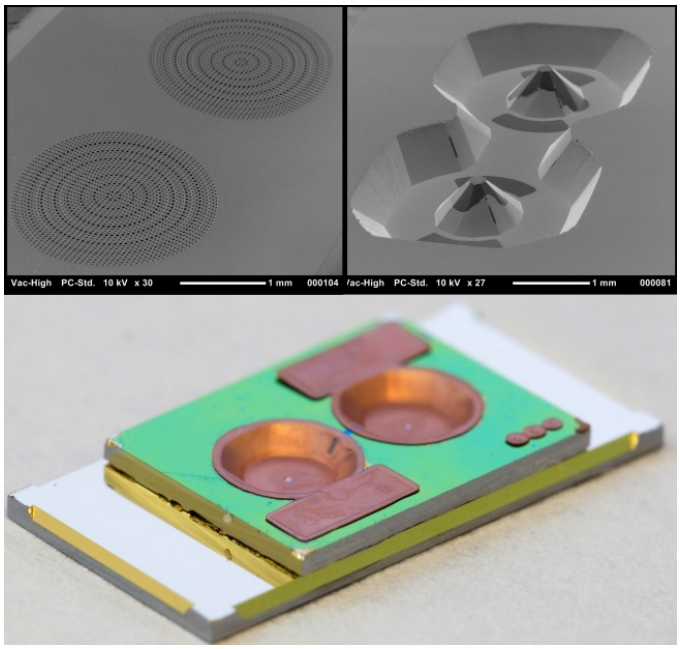

Fig. 3.11. (top) SEM images of (left) the corrugated diaphragm tuners and (right) the cavities. (bottom) Photograph of the assembled filter.

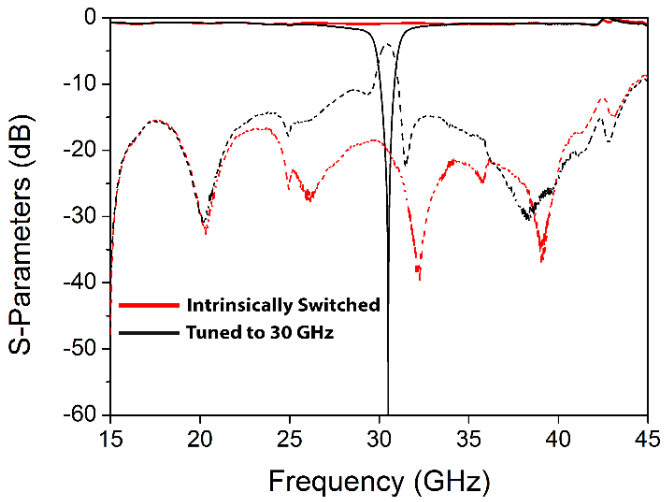

Fig. 3.12. Measured response of the filter when tuned to 30 GHz (black traces) and in its intrinsically-switched all-pass state (red traces)

greater than 9 dB return loss up to 45 GHz. The intrinsically-switched resonators add ~0.5 dB of insertion loss at 43 GHz due to a slight mismatch in coupling strengths due to fabrication uncertainties.

Fig. 3.13 shows the filter when tuned across its full tuning range. The filter tunes from 22 – 43 GHz with very high stopband attenuation from 27 – 34.5 GHz. This tuning

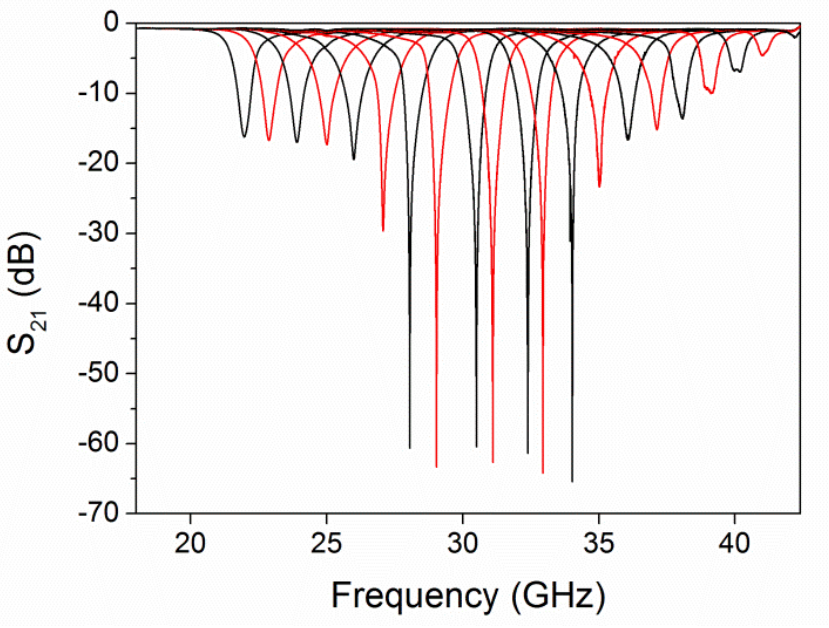

Fig. 3.13. Measured response of the filter when tuned across its entire tuning range.

range was achieved by biasing the electrostatic tuners with 0-80 V, corresponding to approximately 14 μm of deflection of the tuner's membranes.

3.4 Conclusion

High-isolation, widely tunable bandstop filters are demonstrated in the Ka and W bands. The filters combine the narrow bandwidths made possible by high-Q cavity resonators with the high-isolation characteristics of absorptive bandstop filters. These filters cover 22-43 GHz and 75-108 GHz, and produce notch depths of > 70 dB with narrow (4.5% and 1.5%, respectively) 3-dB bandwidths. The high performance of these filters and their potential for low-cost batch fabrication using mature MEMS fabrication processes make these filters attractive candidates for enabling robust Ka- and W-band communication systems which can operate in the presence of strong dynamic interferers.

4. A 0.95/2.45 GHZ SWITCHED BANDPASS FILTER USING COMMERICALLY-AVAILABLE RF MEMS TUNING ELEMENTS

4.1 Introduction

Radio-frequency (RF) software-defined radio chipsets are becoming increasingly available for a wide variety of bands including, for example, the industrial, scientific, and medical (ISM) bands. Robust operation of such a system often requires high-performance, multi-functional RF filters to enable adaptive preselection of the signal of interest while suppressing undesired interferers and noise. Fulfilling these requirements and ensuring high-quality transmission of the desired signal within a certain ISM bandwidth, miniaturized highly-selective bandpass filters (BPFs) with broadband switching/tuning capabilities need to be developed. This article describes the work of the first place award of the student design competition "Tunable RF Microelectromechanical Systems (MEMS) Filters" of the IEEE Microwave Theory and Techniques Society that was held in the 2015 International Microwave Symposium (IMS 2015) in Phoenix, Arizona. It addresses the RF design and implementation of a switched-frequency BPF using commercially-available RF MEMS capacitors.

4.2 Switched Filter Specifications

The main objectives of the "Tunable RF MEMS Filters" IMS 2015 student design competition include the RF design and practical realization of a compact, low-loss, two-state switchable microwave BPF that is able to operate at two alternative ISM bands (0.95 and 2.45 GHz) with a constant bandwidth of at least 100 MHz at each band. In particular, when operating at the low ISM band (centered at 0.95 GHz), the filter is

required to provide over 30 dB of rejection for frequencies between 0.5–0.8 GHz and 1.1–3.5 GHz while featuring a minimum insertion loss in its 0.9–1.0 GHz passband. Likewise, when operating at the high ISM band (centered at 2.45 GHz), a rejection beyond 30 dB needs to be obtained for frequencies between 0.5–2.3 GHz and 2.6–3.5 GHz, with minimum insertion loss for frequencies between 2.4–2.5 GHz. WS1041 digitally-tunable capacitors from WiSpry, Inc. were provided to the participating teams to be used as tuning elements. Conceptual drawings of the desired filtering transfer functions are illustrated in Fig. 4.1.

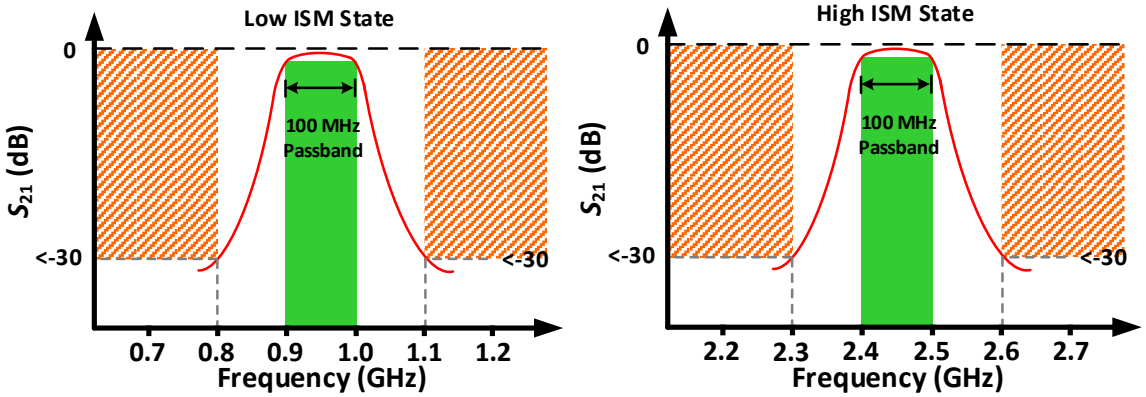

(a) (b)

Fig. 4.1. A conceptual illustration of the expected filtering transfer functions of the BPF for (a) the low ISM state (centered at 0.95 GHz), and (b) the high ISM state (centered at 2.45 GHz).Filter Design

4.2.1 Proposed Concept: Intrinsically-Switched Parallel-Cascaded BPFs

A number of different approaches can be taken in order to realize the specified two-state switchable BPF. For example, a tunable filter with 0.95-2.45 GHz tuning range could be implemented. Though filters with such wide tuning ranges have been demonstrated [39], [71], [100], the highly-selective filtering transfer function and absolute bandwidth required would be very difficult to preserve over such a wide frequency range. A switched-filter bank utilizing series RF switches (e.g. [101]) is an obvious choice, but is not within the scope of this competition due to the requirement of using WiSpry WS1041 tunable capacitors as tuning/switching elements. Therefore, a filter design approach based on parallel-cascaded intrinsically-switched BPFs [19] is

proposed. It consists of two intrinsically-switched BPFs centered at 0.95 GHz and 2.45 GHz, as illustrated in

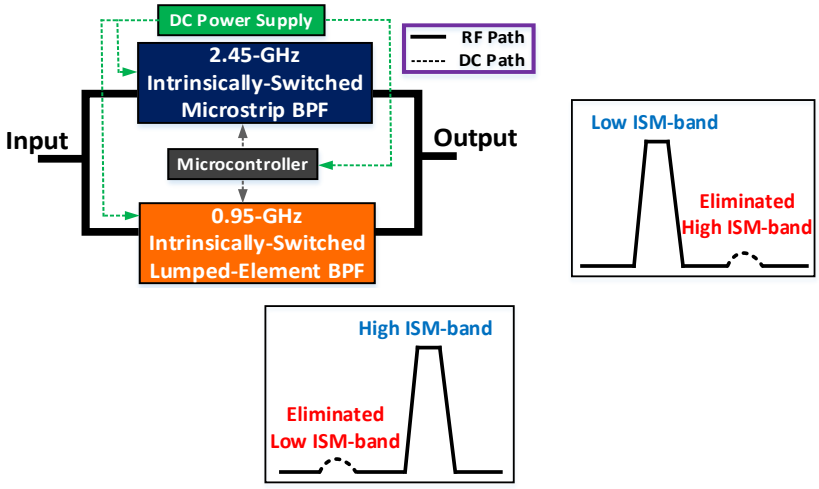

(a) (b) (c)

Fig. 4.2. (a) Schematic diagram of the proposed filter architecture and conceptual drawings of (b) the low ISM-band and (c) the high ISM-band filtering transfer functions.

Fig. 4.2 (a). To create the overall response, either of the two BPFs is intrinsically switched off by strongly detuning some of its resonators [102]. Note that with the conceived filter design approach, both BPFs can be individually designed at arbitrary center frequencies featuring independently-specified bandwidths.

Switching of the BPF architecture is realized by means of commercially available RF MEMS capacitors (WS1041) from WiSpry. They are single-chip, fully-integrated tunable capacitor arrays that feature four internal high-quality-factor (high-Q), high-linearity, digitally tunable capacitors which can be used in series, shunt or mixed configurations. Each of the four internal capacitors exhibits a 4-bit, 0.2─1.5 pF capacitance tuning range with a 0.05-pF resolution. Two supply voltages of 3.3 V and 1.8 V are required for operation. Tuning of the WiSpry capacitors is achieved through a digital serial control interface which needs to be generated by an auxiliary digital subsystem.

In order to fulfill the requirements of small physical size and low insertion loss, a hybrid integration scheme was employed for realizing the proposed filter cascade architecture. Note that a lumped-element design approach and a microstrip-line filtering topology were used for the materialization of the 0.95-GHz and the 2.45-GHz BPFs,

respectively. In this manner, the overall form factor of the filter architecture can be minimized while preserving a low passband insertion loss.

4.2.2 0.95-GHz Lumped-Element BPF Design

A four-pole, quasi-elliptic BPF topology was selected for the low ISM band filter as it presented a good compromise between passband insertion loss, stopband rejection, and complexity. Due to the large size of microstrip resonators at 0.95 GHz, a lumped-element realization was employed. The coupling matrix diagram (CMD) in Fig. 4.3(a) and its corresponding coupling matrix (CM) in (4.1) were used for the design of the 0.95-GHz BPF with a fractional bandwidth of 12%, a passband return loss of 20 dB, and two symmetric TZs.

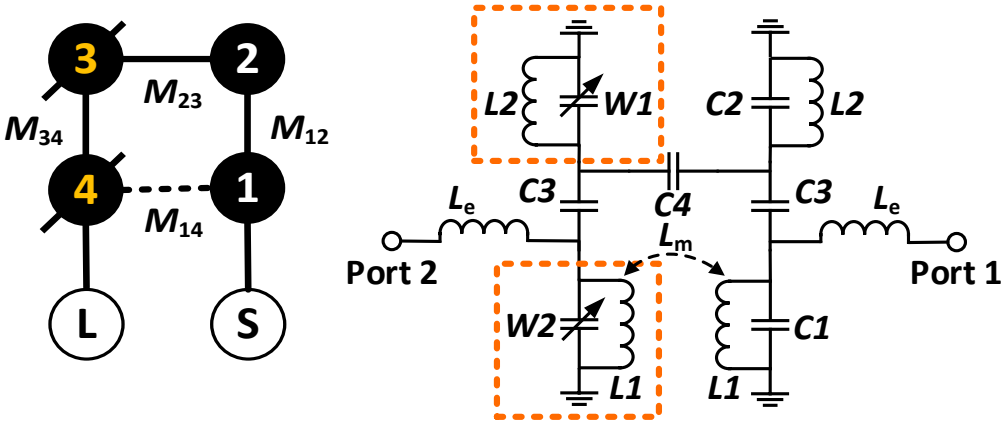

(a) (b)

Fig. 4.3. (a) CMD (black circles: resonant nodes; white circles: source (S) and load (L); static resonators: 1 and 2; tunable resonators: 3 and 4; solid lines: direct couplings; dashed line: cross coupling) of the four-pole quasi-elliptic BPF and (b) schematic of the designed 0.95-GHz lumped-element BPF. The optimized component values are: L1 = 12 nH, L2 = 8 nH, Le = 20 nH, Lm= 0.2 nH, C1 = W2 = 2.2 pF, C2 = W1 = 1.9 pF, C3 = 0.3 pF, C4 = 0.2 pF.

$$[M_{\mathrm{Low-Band}}] = \begin{bmatrix} M_{\mathrm{SS}} & M_{\mathrm{S1}} & \cdots & M_{\mathrm{S4}} & M_{\mathrm{SL}} \\ M_{1\mathrm{S}} & M_{11} & \cdots & M_{14} & M_{1\mathrm{L}} \\ \vdots & \vdots & \ddots & \vdots & \vdots \\ M_{4\mathrm{S}} & M_{41} & \cdots & M_{44} & M_{4\mathrm{L}} \\ M_{\mathrm{LS}} & M_{\mathrm{L1}} & \cdots & M_{\mathrm{L4}} & M_{\mathrm{LL}} \end{bmatrix} =$$

$$\begin{bmatrix} 0 & 0.123 & 0 & 0 & 0 & 0 \\ 0.123 & 0 & 0.107 & 0 & -0.012 & 0 \\ 0 & 0.107 & 0 & 0.089 & 0 & 0 \\ 0 & 0 & 0.089 & 0 & 0.107 & 0 \\ 0 & -0.012 & 0 & 0.107 & 0 & 0.123 \\ 0 & 0 & 0 & 0 & 0.123 & 0 \end{bmatrix} \quad (4.1)$$

A realistic implementation scheme of the aforementioned CMD is illustrated in the schematic circuit of Fig. 4.3(b). In order to realize the desired switching functionality, the third and fourth *LC* resonators of the BPF are made tunable by employing the WS1041 capacitors, noted as *W1* and *W2* in Fig. 4.3(b), while the first and second *LC* resonators (*L1*, *C1* and *L2*, *C2*) are static. By detuning two of the four resonators, around 25 dB of rejection can be obtained as compared to approximately 15 dB of rejection if only one of the resonators is detuned. Detuning the remaining (third and fourth) resonators would further complicate design, while yielding little improvement in rejection. Two of the four capacitors within each WS1041 chip are used in a parallel configuration, yielding a total capacitance tuning range of 1.2─3.85 pF including an intrinsic shunt parasitic capacitance of 0.4 pF at each terminal of the capacitor bank. The resonator inductances are chosen to yield a center frequency of 0.95 GHz.

The inter-resonator and external coupling elements are realized with lumped-element admittance inverters. Note that capacitive inter-resonator couplings are utilized in this design because the required coupling capacitance values (*C3* and *C4* in Fig. 4.3(b)) are more realistic at the designed frequency than the equivalent coupling inductance values (0.2─0.3 pF versus 100─800 nH). Furthermore, the external coupling is realized inductively (L_e in Fig. 4.3(b)) so that the upper stopband can be approximated as an open circuit, which simplifies the process of cascading the two filters. In order to realize the negative coupling coefficient M_{14}, the inductors *L1* of the first and fourth resonators are placed in close proximity to each other so that a weak mutual inductance (L_m) is created between them. The spacing between the inductors for realizing L_m was specified through full-wave EM simulations, and the final values of the filter components were obtained

through post-layout simulations. The EM-simulated resonant frequency of the tunable *LC* resonator is plotted versus the total loading capacitance in Fig. 4.4(a). As can be seen, the third and fourth resonators can be detuned from 0.95 to 0.6 GHz.

The EM-simulated "On"- and "Off"-state frequency responses of the 0.95-GHz BPF are plotted in Fig. 4.4(b). In the "On" state, all of the filter's resonators are synchronously tuned and the BPF has approximately 2 dB of insertion loss and 20 dB return loss in the passband. In the "Off" state (maximum detuned state of the filter), the bandpass response

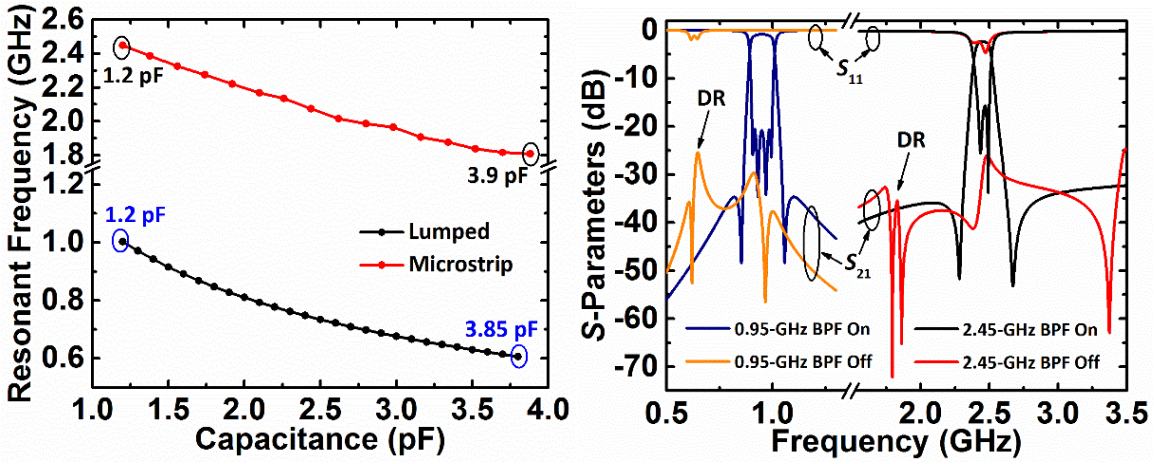

(a) (b)

Fig. 4.4. (a) EM-simulated resonant frequencies versus loading capacitances for a single tunable *LC* resonator and a single microstrip resonator using the WiSpry tunable capacitor and (b) EM-simulated frequency responses of the 0.95-GHz lumped-element and the 2.45-GHz microstrip BPFs when tuned to the "On" and "Off" states. "DR" in (b) indicates the detuned resonances of the filter resonators.

is eliminated and approximately a 25 dB out-of-passband rejection is achieved for frequencies from 0.5─3.5 GHz

4.2.3 2.45-GHz Microstrip BPF Design

As a design compromise between filter performance and occupied physical area, a fourth-order microstrip BPF design based on a high-permittivity, low-loss Rogers RT/Duroid 6010 substrate (ε_r = 10.2, dielectric tanδ = 0.0023) was chosen. The BPF is composed of four highly-miniaturized hairpin-line resonators and is illustrated in Fig. 4.5(a). It realizes the CMD illustrated in Fig. 4.5(a), which possesses an elliptic-type

transfer function. Note that in this configuration the third and fourth resonators are capacitively loaded with the WS1041 capacitors which enable frequency tuning, while the first and second resonators are unloaded. The detailed geometries of both the loaded and the unloaded hairpin-line resonators are illustrated in Fig. 4.5(b).

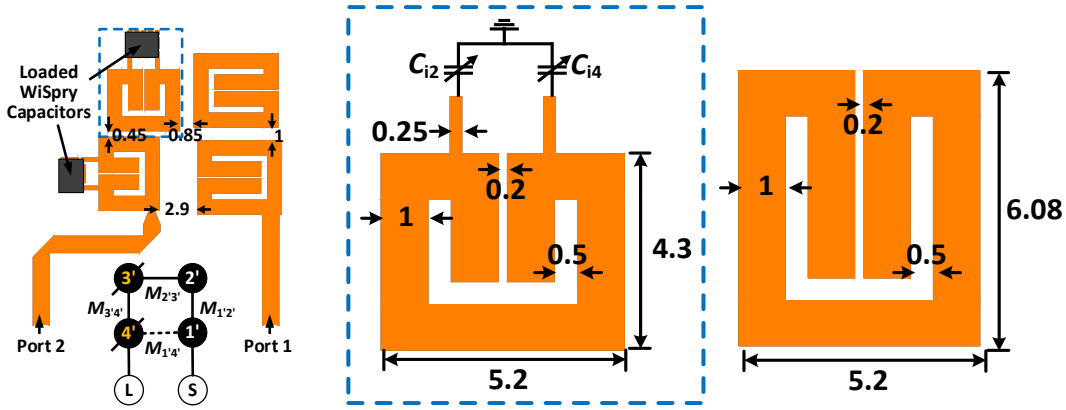

(a) (b)

Fig. 4.5. (a) Layout and CMD (black circles: resonant nodes; white circles: source (S) and load (L); static resonators: 1' and 2'; tunable resonators: 3' and 4'; solid lines: direct couplings; dashed line: cross coupling) of the designed 2.45-GHz microstrip BPF and (b) layout of the loaded (left) and unloaded (right) hairpin-line resonators. Dimensions are all in millimeters.

$$[M_{\text{High-Band}}] = \begin{bmatrix} M_{SS} & M_{S1'} & \cdots & M_{S4'} & M_{SL} \\ M_{1'S} & M_{1'1'} & \cdots & M_{1'4'} & M_{1'L} \\ \vdots & \vdots & \ddots & \vdots & \vdots \\ M_{4'S} & M_{4'1'} & \cdots & M_{4'4'} & M_{4'L} \\ M_{LS} & M_{L1'} & \cdots & M_{L4'} & M_{LL} \end{bmatrix} = \begin{bmatrix} 0 & 0.050 & 0 & 0 & 0 & 0 \\ 0.050 & 0 & 0.044 & 0 & -0.005 & 0 \\ 0 & 0.044 & 0 & 0.036 & 0 & 0 \\ 0 & 0 & 0.036 & 0 & 0.044 & 0 \\ 0 & -0.005 & 0 & 0.044 & 0 & 0.050 \\ 0 & 0 & 0 & 0 & 0.050 & 0 \end{bmatrix} \tag{4.2}$$

The analyses of the individual resonators as well as the final filter design were performed in ANSYS high-frequency structural simulator (HFSS) in which conductor loss, dielectric loss, and radiation loss have been taken into consideration. The EM-simulated resonant frequency of a single WS1041-loaded hairpin-line resonator is plotted versus the loading capacitance in Fig. 4.4(a), showing a tuning range of 2.45─1.8 GHz. Employing the geometrical configuration in Fig. 4.5(a), the 2.45-GHz BPF was designed using the CM in (4.2) to have a fractional bandwidth of 4.9%, a passband return loss of 20 dB, and two TZs located at 2.3 and 2.6 GHz. The inter-resonator coupling coefficients

are determined by the separation of two adjacent resonators, while the external couplings are controlled by the tapping position of the microstrip lines on the first and fourth resonators. The extraction of these matrix parameters was performed in HFSS using the design methodology in [92].

The EM-simulated frequency response of the 2.45-GHz filter when tuned to the "On" and "Off" states is plotted in Fig. 4.4(b). In the "On" state, the filter has approximately 2.3 dB of insertion loss and 16 dB return loss in the passband. In the "Off" state, when the tuning capacitors are set to their maximum values and the bandpass response is eliminated, the worst-case rejection from 0.5─3.5 GHz is calculated to be around 25 dB.

4.2.4 RF Design of the BPF Cascade

The standard filter synthesis and design procedures assume a 50-Ω characteristic impedance for both the source and the load of the filter. Away from the designed frequency, however, the input/output impedances of each BPF are reactive, and as such a reactance is introduced at the source/load of either of the two filters. This in turn results in passband degradation when the individual filters are parallel-cascaded as shown in Fig. 4.1(a). In order to overcome this problem, the filter design need to be modified so that the input/output impedances are complex-conjugate matched to the reactive source/load impedances. However, this process becomes complicated when the two filters must be simultaneously matched to each other. Alternatively, a matching network can be designed and inserted in between the two filters to transform the complex impedance that each filter presents at the source or the load of the other filter into an open circuit.

In this design, the input/output impedances of the 0.95-GHz BPF are nearly open-circuited at 2.45 GHz due to the use of inductive external couplings (L_e), presenting negligible reactance to the input and the output of the 2.45-GHz BPF. The input/output impedances of the 2.45-GHz BPF are heavily-reactive at 0.95 GHz, but they can easily be transformed into an open circuit by simply inserting a section of 50-Ω microstrip line between these two filters, as illustrated in the overall filter layout in Fig. 4.6(b). Note that different lengths of microstrip lines are required for the source and load because the input and output impedances of the 2.45-GHz BPF are different when two of its resonators are

detuned to their "Off" states. The physical lengths of the microstrip impedance-transforming lines are 49.2 and 41.3 mm (in terms of electrical lengths, θ_1 = 154° and θ_2 = 121°, at 0.95 GHz).

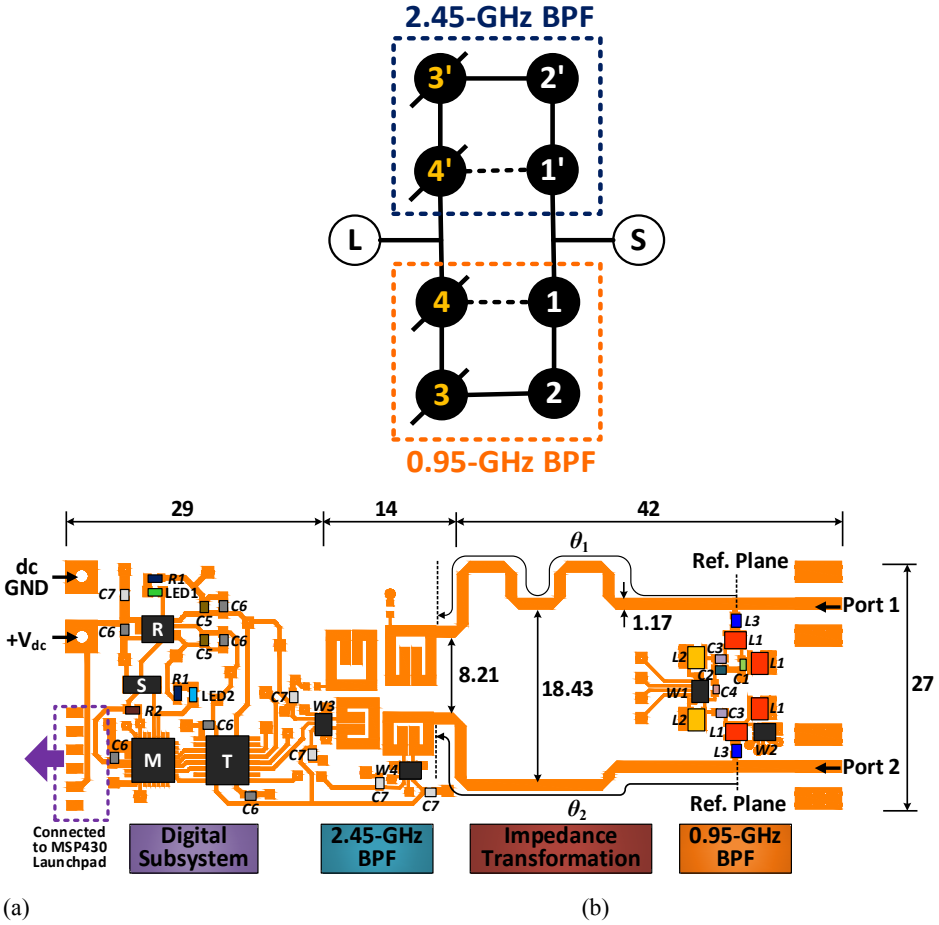

(a) (b)

Fig. 4.6. (a) Combined resonator coupling topology of the 0.95/2.45-GHz switched-frequency BPF and (b) Front view of the filter layout, where dimensions are all in millimeters.

The input/output microstrip lines of the 2.45-GHz BPF need to be well separated so as not to degrade the out-of-passband rejection levels. All four WS1041-loaded tunable resonators are controlled by a microcontroller (MCU)-based digital subsystem at the core of which is a 16-bit MSP430 MCU from Texas Instruments (TI). Other critical components in the digital circuit include a TI 6-bit bidirectional level-shifter which interfaces the microcontroller to the WS1041, and a TI low-dropout regulator, all of which are listed in Table 4.1 together with other lumped components labeled in Fig.

4.6(b). The lumped inductors and capacitors utilized are Coilcraft 0908SQ series [15] and Johanson Technology R07S series [16], respectively.

Table 4.1. Summary of the Components Labeled in Fig. 4.6(b)

Component	Value	Component	Value
L1	12.1 nH	*C4*	0.2 pF
L2	8.1 nH	*C5*	47 pF
L3	8.2 nH	*C6*	10 μF
C1	2.0 pF	*C7*	1 μF
C2	1.7 pF	*R1*	150 Ω
C3	0.3 pF	*R2*	100 KΩ

Others	Description	Part Number
T	TI 6-Bit Bidirectional Level-Shifter	TXB0106
M	TI 16-bit Low-Power Microcontroller	MSP430G2553
R	TI Low-Dropout Voltage Regulator	LP2966
S	Omron SPST Switch	B3U-1000P
LED1, 2	Light-emitting diode (LED)	LG L29K
W1–W4	WiSpry Digitally-Tunable Capacitor	WS1041

4.3 Measured Performance of the 0.95/2.45-GHz Switched-Frequency BPF

Fig. 4.7 shows a photograph of the manufactured filter, whose total volume is around 16 cm^3 including the two subminiature A (SMA) connectors. The measured and EM-simulated frequency responses of the filter cascade are depicted in Fig. 4.8(a)–(d). As can be seen, good agreement is obtained between the RF-measured and EM-simulated plotted curves for all reconfigurable states. In particular, it can be observed that in the low ISM-band state, the filter exhibits a mid-band insertion loss of around 2.4 dB and provides greater than 26 dB of rejection across its entire stopband. Furthermore, in the high ISM-band state, the filter exhibits a mid-band insertion loss of 3.9 dB and provides greater than 23 dB of rejection across its entire stopband. Compared to the simulated results, the measured mid-band insertion losses for the low and high ISM-passbands are 0.4 dB and 1.6 dB higher, respectively, and the measured passband return losses are on average 5–10 dB worse. These effects can be attributed to 1) manufacturing tolerances of the microstrip circuit, 2) additional losses from radiation, SMA connectors, and surface/edge roughness of the microstrip lines, and 3) component tolerances of the lumped inductors and

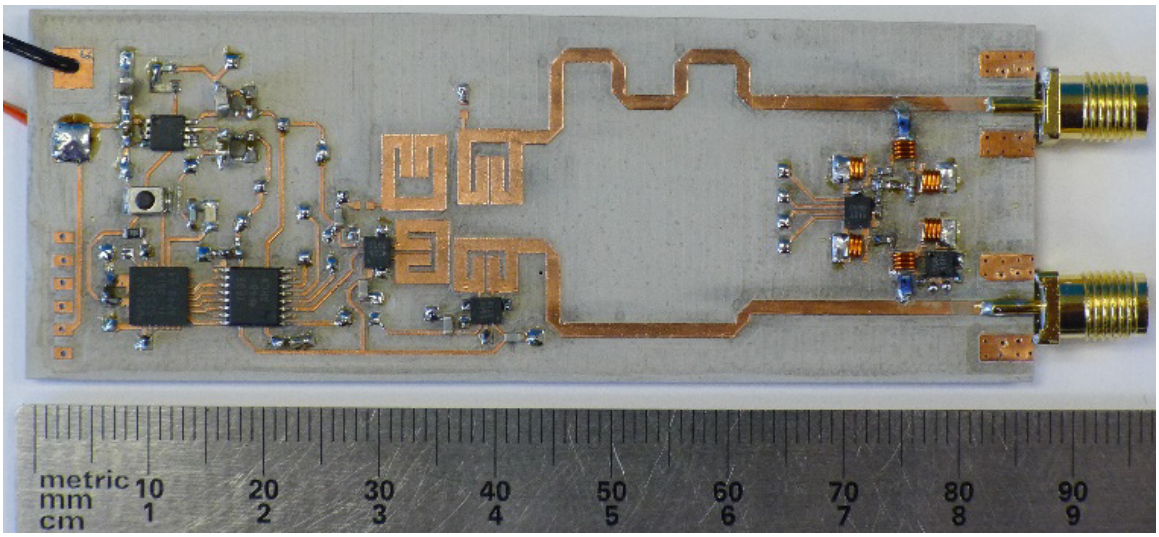

Fig. 4.7. Photograph of the manufactured filter.

capacitors. These parasitic effects also yield slight discrepancies of the S_{11} and S_{21} parameters for frequencies out of the desired passbands. A parasitic resonance due to the self-resonance of the inductor L3 can be observed around 2.7–2.8 GHz in each measured state, degrading the attenuation at the adjacent frequencies to a certain extent.

4.4 Conclusion

In this article, the RF design and the practical realization of a compact, multi-state BPF that is capable of switching its passband between 0.95 and 2.45 GHz were developed within the scope of the IMS2015 Student Design Competition. The proposed filtering architecture is based on a hybrid implementation composed of a 0.95-GHz fourth-order lumped-element BPF and a 2.45-GHz fourth-order microstrip BPF that are arranged in a parallel configuration and realize a quasi-elliptic filtering transfer function. Switching functionality is achieved by integrating RF MEMS digitally tunable capacitors from WiSpry in two of the resonators of each parallel-connected BPF that can in turn be detuned and effectively switch off the operation of each BPF. The highly miniaturized filter occupies a volume of only 16 cm^3 including all associated digital circuitry. The filter provides an innovative solution to the competition criteria, while being subject to the constraints of the competition. It offers an attractive solution over conventional

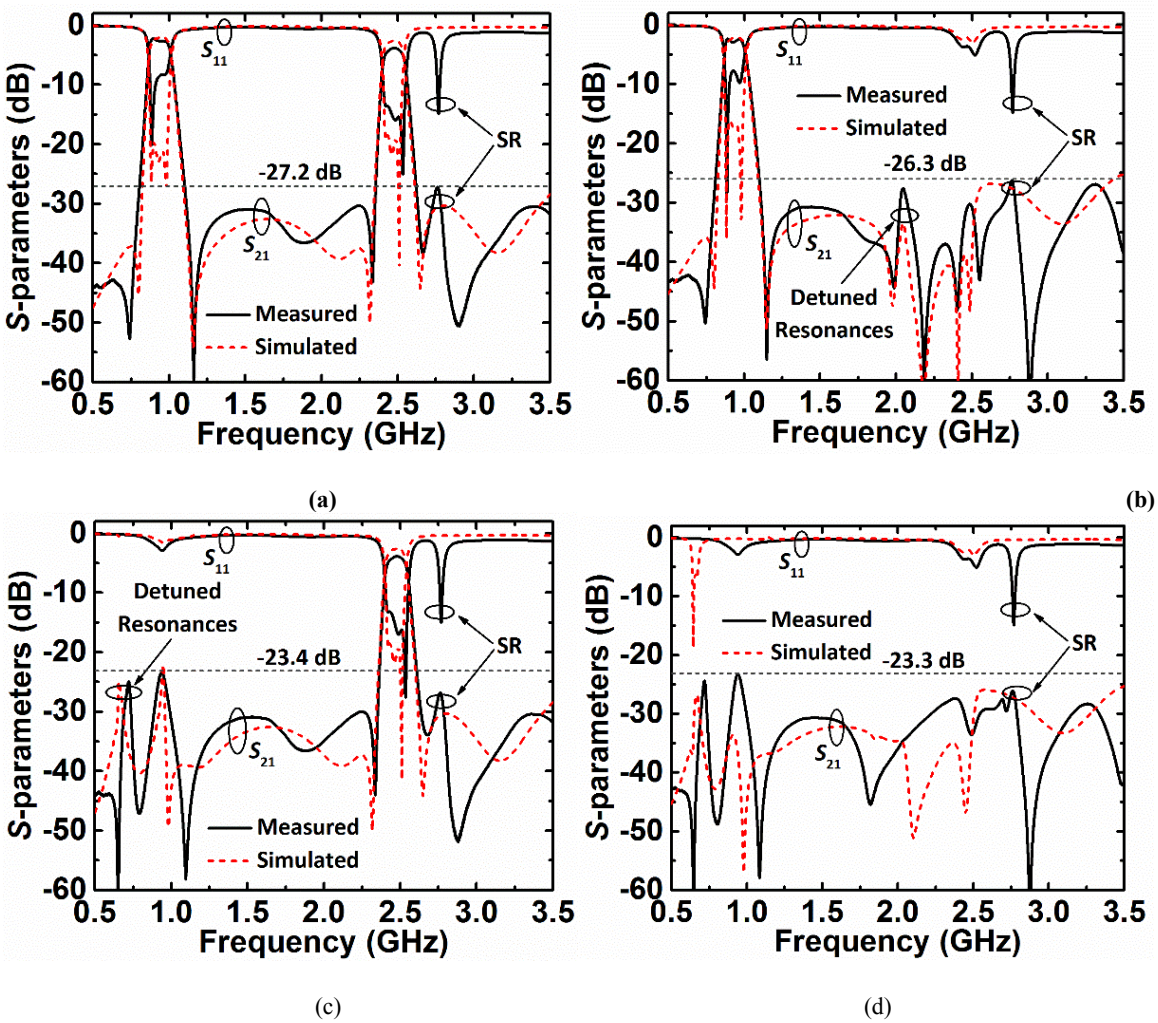

Fig. 4.8. (a) RF-measured and EM-simulated frequency responses of the filter: (a) both passbands on, (b) lower passband on and higher passband off, (c) lower passband off and higher passband on, and (d) both passbands off. The "SR" in each state indicates the self-resonance of the inductor *L3*.

widely-tunable filters as it is able to switch over a very wide (~2.6:1) frequency range while maintaining a nearly-constant absolute bandwidth, and low insertion loss. The proposed filter architecture received the first place in the student design competition, and its obtained RF performance makes it an excellent candidate for multifunctional ISM-band radio communication systems.

5. CONSTANT-BANDWIDTH TUNABLE BANDSTOP FILTERS

5.1 Introduction

Tunable bandstop filters have been the focus of many research endeavors in recent years due to their ability to suppress signals at will by many orders of magnitude with a high degree of selectivity. Tunable bandstop filters can be cascaded with bandpass filters in order to add additional isolation to that already provided by the bandpass filter ([103], [104]), or can be used without a preselect bandpass filter at the front end of a receiver chain in order to realize a very wideband receiver with the ability to reject undesired signals, such as image frequencies or jammers.

Though many excellent examples of tunable bandstop filters have been demonstrated, almost all are plagued by large variations in bandwidth when tuned over wide frequency ranges. Only a short survey of published tunable bandstop filters is needed to see this. In [56], a bandstop filter which has a 0.65 to 1.65 GHz tuning range and a 1.2% to 3.2% fractional bandwidth (FBW) is presented. An 8.6-11.3% FBW is seen in [105], a bandstop filter with a 1.3 to 2.3 GHz tuning range. The filter in [86] experiences a 4.0% to 5.9% FBW over an 8.9 to 11.3 GHz tuning range, and the filter in [26] 1.6-4.2% FBW with slightly over an octave tuning range.

The reason for the variation in fractional bandwidth over tuning range is related to the coupling structures which connect the resonators of the filters to the source and load. The FBW of a 1st order lossless bandstop filter consisting of a shunt parallel resonator coupled to a source-to-load transmission line with an external coupling element of magnitude K_0 can be shown to depend only on the external coupling [19]:

$$BW_{3dB} = \frac{{K_0}^2}{2} \tag{5.1}$$

Though factors such as finite unloaded quality factor and lengths of transmission lines other than 90^o complicate analytical expressions for the bandwidths of higher-order bandstop filters, they are still primarily determined by the strength of their external coupling. Typical microwave coupling structures used to realize external coupling in bandstop filters include coupled microstrip lines, lumped capacitors or inductors, and apertures in cavities. Coupling structures that rely on a certain geometry to provide the desired coupling coefficient, such as coupled sections of microstrip lines or apertures in cavities, have frequency variation because the electrical size of the structure increases as frequency is increased. Lumped element coupling structures such as capacitors or inductors have frequency-dependent reactances which lead to changes in coupling magnitude.

It is usually even more challenging to maintain a constant absolute bandwidth (ABW) across a wide tuning range, because ABW is equal to $FBW \cdot f_0$, where f_0 is the center frequency of the filter. Even with a perfectly-constant FBW, the ABW of a filter will double when tuned over an octave tuning range. To maintain constant ABW, the FBW must decrease linearly with frequency (i.e. the external coupling coefficient must be inversely proportional to the square root of frequency.)

Several methods for addressing the problem of bandwidth variation have been presented. In [8] and [11], lumped-element absorptive bandstop filters are implemented with inductive admittance inverters which, when combined with capacitively-tuned resonators, provide fairly constant ABW over more than an octave tuning range. Due to the use of lumped-element inductors and capacitors, however, this method is only applicable for frequencies less than approximately 2 GHz.

Another method for maintaining constant ABW is to realize the external coupling with an electrically-long section of coupled transmission line. The length of coupling section can be optimized to blend electric and magnetic coupling, and the opposite frequency dependence of these two types of coupling can partially compensate for each other, yielding a fairly constant bandwidth. Examples of this method can be found in [18] and [106]. This method works well, as [18] demonstrated a 92% center frequency tuning range with only 24% variation in 3-dB bandwidth. However, this method is only

applicable to microstrip or other electrically-long resonators which can use both electric and magnetic coupling.

A third method for realizing constant-bandwidth filters is to utilize tunable coupling elements, so that the coupling can be reduced at higher frequencies in order to maintain constant ABW. In [19] and [107], microstrip resonators loaded with varactors on each end are used. By differentially tuning the varactors, the voltage and current distributions on the resonator can be modified, which tunes the external coupling coefficient and the filter's bandwidth. [107] demonstrates the ability to tune the 3-dB bandwidth from 70 to 140 MHz, and can maintain a constant 100 MHz 3-dB bandwidth over a 1.2 to 1.6 GHz center frequency tuning range. The filter in [19] has a 3-dB bandwidth which can be tuned from 26 to 143 MHz, and can be held constant over a 0.67 to 1.0 GHz tuning range. In [25], substrate-integrated-waveguide cavity resonators are coupled to a through-line with varactors, which allows the filter to maintain a constant 83 MHz 3-dB bandwidth across an 0.77 to 1.25 GHz tuning range. Using tunable coupling elements allows tunable filters to maintain constant bandwidth, but it increases control complexity due to the additional tuning elements, and also decreases the filter's linearity and adds additional loss to the resonators.

Until recently, there was no way to passively control the bandwidth variation of high-Q evanescent-mode cavity resonators. The lumped element coupling method of [8] is not compatible with this type of resonator, particularly at high frequencies where lumped-element components are very lossy. The electric field is concentrated into a very small portion of resonator's volume, while the magnetic field is fairly evenly distributed throughout the volume of the resonator, and thus it is difficult to simultaneously realize both electric and magnetic coupling, and the method used by [106] cannot be used. Tunable coupling elements can be used, as in [25], but it is often preferable to avoid the additional tuning elements introduced by tunable coupling.

A passively-compensated coupling method for evanescent-mode bandstop filters was recently presented by the authors in [108], which for the first time allowed control over bandwidth for bandstop filters of this technology. This paper introduced a method for passively compensating the frequency variation of the filter's coupling coefficients, and showed a constant-ABW filter with only 27% variation in its 3-dB absolute bandwidth

over an octave center-frequency tuning range – an 80% improvement compared to the typical method of coupling for these filters. Our work in this chapter builds on this work by investigating this new bandwidth control method in greater detail, explaining its method of operation and evaluating design considerations for this method such as the relationship between tuning range and bandwidth variation, and the effects of coupling sign and transmission line length on bandwidth variation. It is shown that in addition to providing greatly reduced bandwidth variation, this coupling method also reduces the phase variation of the transmission line between the two resonators of a two-pole bandstop filter, which serves to reduce the variation in the shape of the filter's transfer function. The coupling method is used to design four filters with tuning ranges centered around 4.5 GHz: a two-pole constant FBW filter with an octave tuning range and a 1.16% to 1.3% 3-dB bandwidth; a two-pole constant ABW filter with an octave tuning range and a 50.3 to 56.5 MHz 3-dB bandwidth (12% variation - a 55% improvement over the filter in [108]); a two-pole constant ABW with a 50% tuning range and a 52 to 54 MHz MHz 3-dB bandwidth; and a constant ABW octave-tunable 4-pole filter which can maintain a 50 MHz 10-dB bandwidth which is constant to within the measurement limits of the network analyzer used to characterize the filters.

Section 5.2 of this chapter revisits the coupling concept introduced in [108] and examines its design space, presenting design principles and design tradeoffs. Section 5.3 details the design of constant-bandwidth evanescent-mode cavity based filters using the new coupling method. Section 5.4 presents the measured results of the designed filters, and Section 5.5 concludes the work.

5.2 Constant Bandwidth Coupling Concept

The coupling topology studied in this work is shown in Fig. 5.1 This circuit was first introduced in [19] in order to realize intrinsically-switchable bandstop filters, and was proposed in [108] for the purpose of constant-bandwidth filters.

It can be shown [19] that the circuit of Fig. 5.1(a), consisting of a resonator coupled twice to a through line of length θ_0 with coupling elements k_{E1} and k_{E2}, is equivalent to the circuit of Fig. 5.1(b), which comprises a resonator coupled to a through-line with only

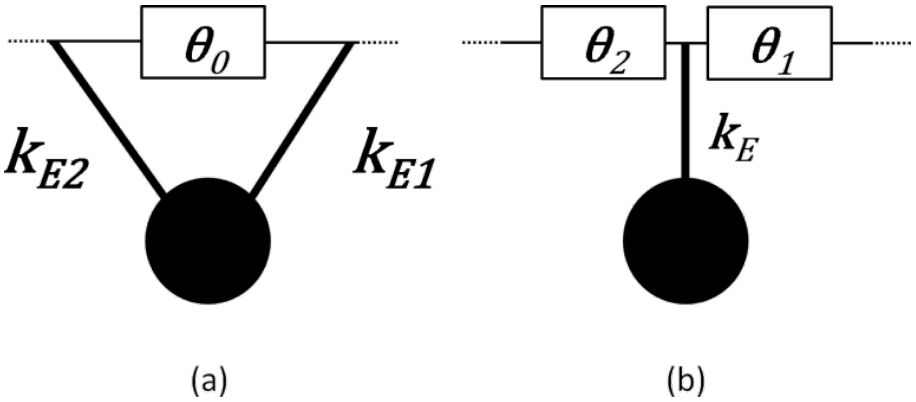

Fig. 5.1. (a) Twice-coupled resonator topology for constant bandwidth. (b) Equivalent circuit of (a).

a single coupling element k_E, followed and preceded by transmission lines of lengths θ_1 and θ_2. There is also a slight resonant frequency offset between the resonators in Fig. 5.1(a) and (b), but this frequency offset can be neglected since we are using widely-tunable resonators which can compensate for any slight frequency offset. The equations relating the expressions in the equivalent circuit to those of the original circuit are:

$$k_E = \sqrt{{k_{E1}}^2 + {k_{E2}}^2 + 2k_{E1}k_{E2}\cos(\theta_0)} \tag{5.2}$$

$$\theta_1 = \frac{1}{2}\left(\pi - \arg\left(-\frac{\frac{k_{E1}}{k_{E2}} + e^{-j\theta_0}}{\frac{k_{E1}}{k_{E2}} + e^{j\theta_0}}\right)\right) \tag{5.3}$$

$$\theta_2 = \theta_0 - \theta_1 \tag{5.4}$$

If the two coupling elements k_{E1} and k_{E2} have roughly the same frequency dependence but one is a fraction of the other, e.g.

$$k_{E2} \approx r k_{E1} \tag{5.5}$$

where r is a constant, then (5.2) can be approximated as

$$k_E = k_{E1}F \tag{5.6}$$

$$F = \sqrt{1 + r^2 + 2r\cos(\theta_0)} \tag{5.7}$$

We now see that the total equivalent coupling coefficient is equal to one of the original coupling coefficients multiplied by a shaping factor F which, because the electrical length of the transmission line θ_0 is proportional to frequency, has a

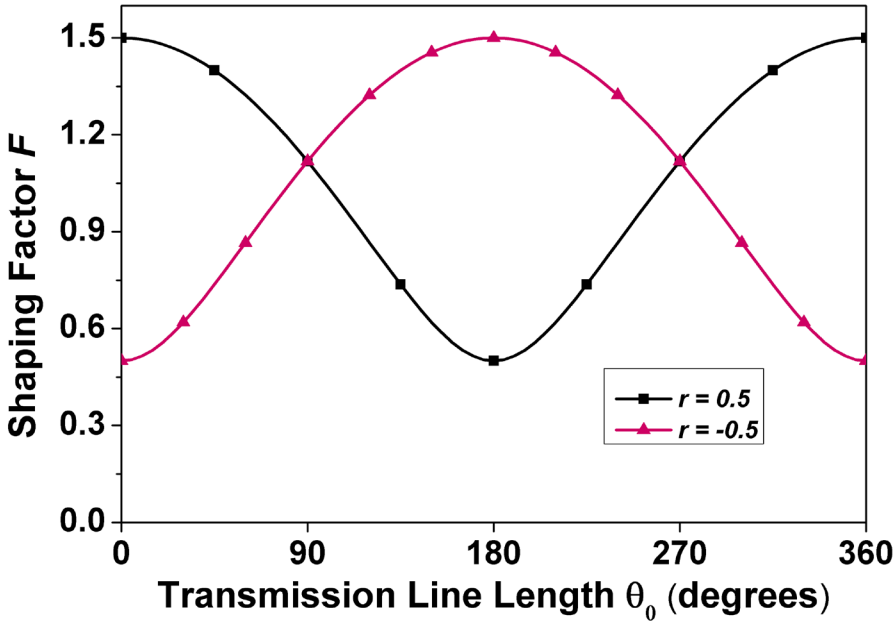

Fig. 5.2. Frequency variation of the shaping factor F which modifies the frequency dependence of the coupling apertures.

sinusoidal-like frequency dependence. The frequency dependence of the shaping factor F is plotted in Fig. 5.2. It can be seen that when the two coupling coefficients have the same sign (i.e. *r* is positive), F has a negatively-sloped frequency dependence for $0^o < \theta_0 < 180^o$ and a positive frequency dependence for $180^o < \theta_0 < 360^o$. Conversely, when the two coupling coefficients have opposite sign (that is, *r* is negative), the opposite trend is observed: F has a positive frequency dependence for $0^o < \theta_0 < 180^o$ and a negative frequency dependence for $180^o < \theta_0 < 360^o$. The regions where F has negative frequency dependence ($0^o < \theta_0 < 180^o$ when the coupling coefficients have the same sign, and $180^o < \theta_0 < 360^o$ when they have opposite signs) can be used to at least partially compensate for the positive frequency dependence inherent in the original coupling structure.

To see how this method can realize constant coupling coefficients for constant-FBW filters and coupling coefficients which decrease with frequency for constant-ABW filters, we will apply this method to a frequency-dependent coupling coefficient and investigate how the various design parameters affect the frequency variation of the composite coupling coefficient. In the rest of the figures in Section 5.2, k_{E1} is defined such that it

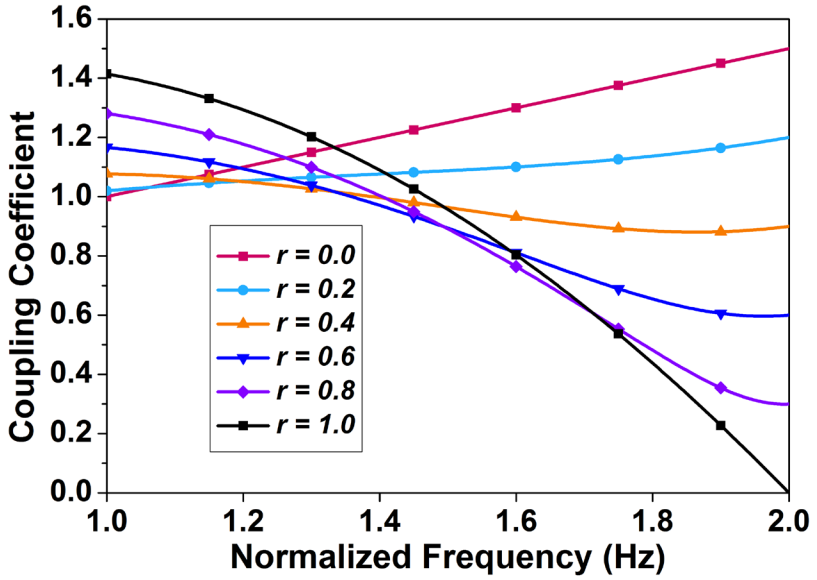

Fig. 5.3. Frequency variation of coupling coefficient for various values of coupling ratio r. θ_0 = 180° at 2 Hz in this figure.

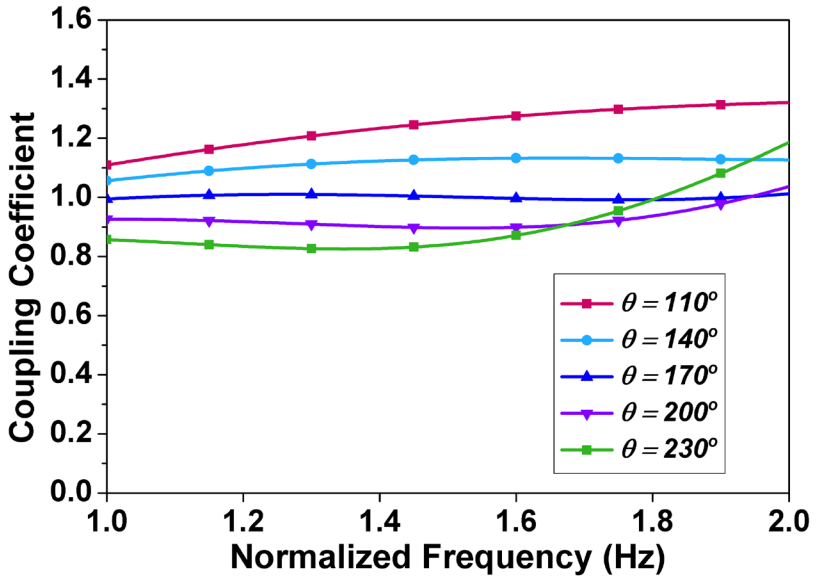

Fig. 5.4. Frequency variation of coupling coefficient for various values of transmission line θ_0. r = 0.3 in this figure.

has a nominal value of 1 at the resonator's minimum tuned frequency and increases by 50 % over an octave tuning range:

$$k_{E1} = 1 + 0.5\left(\frac{f_0}{f_{min}} - 1\right) \tag{5.8}$$

We will see in Section 5.3 that this frequency dependence is fairly accurate approximation of practical coupling coefficients.

The effect that changing *r*, the ratio of the two coupling elements, has on the variation of coupling coefficient is shown in Fig. 5.3. It can be seen that when r is zero, the composite coupling coefficient k_E is the same as that of a single coupling element, increasing by 50% over an octave tuning range. As r is increased, the coupling is increased at lower frequencies and reduced at higher frequencies, reaching a value of zero at the frequency at which θ_0 is 180^o when r = 1. This can be understood intuitively, because two coupling structures of equal magnitude separated by a 180^o transmission line should cancel each other out, resulting in a net zero coupling coefficient.

The dependence of coupling variation on the length of transmission line θ_0 separating the coupling elements is plotted in Fig. 5.4. The values of θ_0 stated are defined at 2 Hz. It can be seen that for lengths of θ_0 less than 170^o, the coupling coefficient has a concave-down shape, whereas it is concave-up for lengths of θ_0 greater than 170^o. For the specific frequency dependence of the coupling coefficient used in this example, a transmission line of length 170^o at 2 Hz and r = 0.28 results in a nearly-constant coupling coefficient as needed for constant FBW, and a transmission line of length 180^o at 2 Hz and coupling ratio r = 0.6 causes the coupling coefficient to decrease with frequency as required for constant ABW.

5.2.1 BW Variation vs. T-Line length and Tuning Range

The shaping factor F has a negative slope with respect to frequency over a wide range of frequencies, and thus is able to reduce the amount of coupling variation over wide tuning ranges. However, it can be seen that the slope of F is much more linear over narrow ranges of θ_0 (in the neighborhood of $\theta_0 = 90^o$ when r is positive and $\theta_0 = 270^o$ when r is negative), and it is thus expected that this method will be even more effective when utilized over narrow tuning ranges. In general, the amount of reduction in bandwidth variation is a nonlinear function of the tuning range over which the bandwidth variation is optimized. To show this, the transmission line length θ_0 and coupling ratio r were optimized in order to provide minimum possible bandwidth variation for a variety

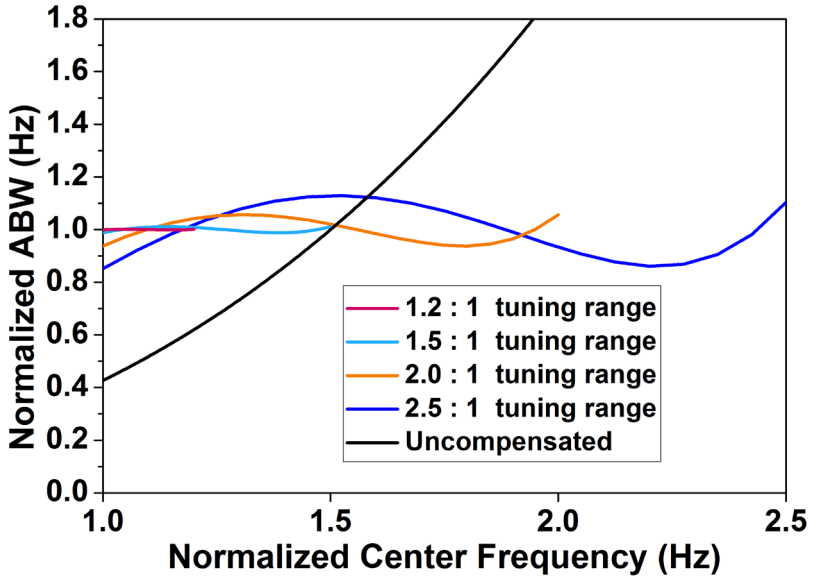

Fig. 5.5. Frequency variation of absolute bandwidth for different tuning ranges.

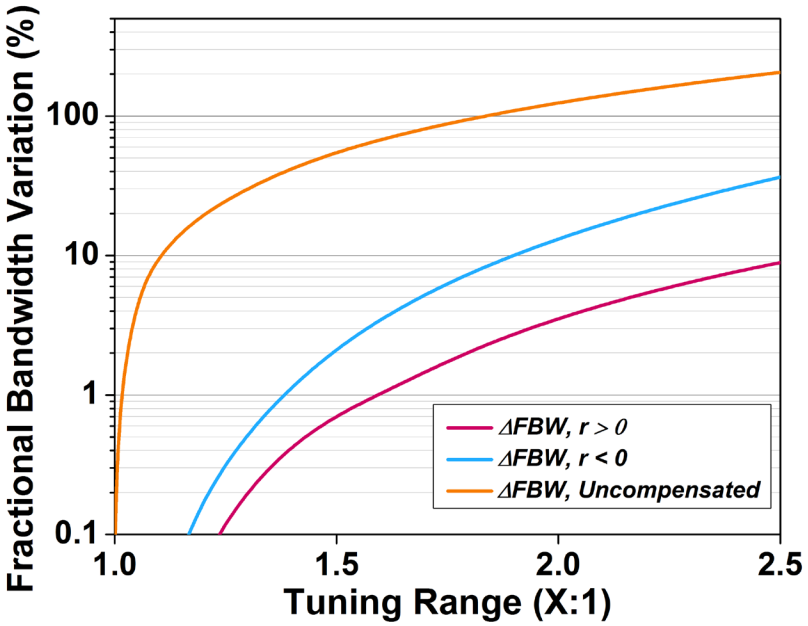

Fig. 5.6. Minimum possible FBW variation as a function of center frequency tuning range.

of tuning ranges, using the model for coupling coefficient defined in equation (5.8). The resulting ABW variation is shown in Fig. 5.5. As expected, for all tuning ranges the bandwidth variation is significantly reduced compared to the uncompensated case.

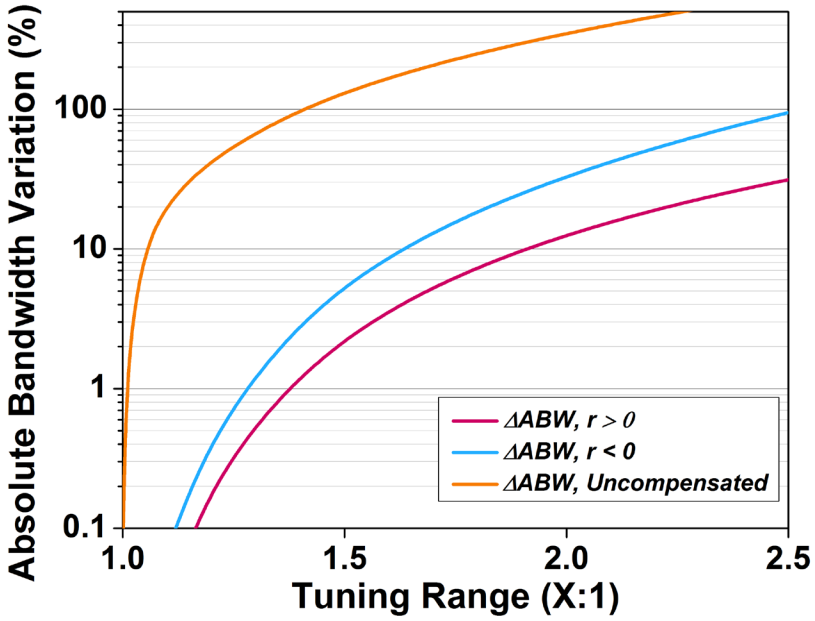

Fig. 5.7. Minimum possible ABW variation as a function of center frequency tuning range.

However, as the tuning range decreases, the bandwidth variation reduces dramatically and can be come nearly constant for small tuning ranges. Fig. 5.6 and Fig. 5.7 plot the minimum possible bandwidth variation (FBW and ABW, respectively) versus tuning range. The bandwidth variations are defined as:

$$\Delta FBW = 100 \cdot \left(\frac{\max(FBW)}{\min(FBW)} - 1 \right) \tag{5.9}$$

$$\Delta ABW = 100 \cdot \left(\frac{\max(ABW)}{\min(ABW)} - 1 \right) \tag{5.10}$$

Fig. 5.6 and Fig. 5.7 show the degree to which the proposed method can reduce bandwidth variation. For example, over an octave (2:1) tuning range, the proposed method can reduce the FBW variation from 150% to just 3.5%, and can reduce the ABW variation from 350% to just 12%. Reducing the tuning range by 50% to 1.5:1 greatly reduces the amount of bandwidth variation. In this case the FBW variation can be reduced to approximately 0.7%, and the ABW variation can be reduced to approximately 2%.

The figures also show the difference between utilizing coupling elements of the same sign, which requires a transmission line which is ~180^{o} at f_{max}, and utilizing coupling

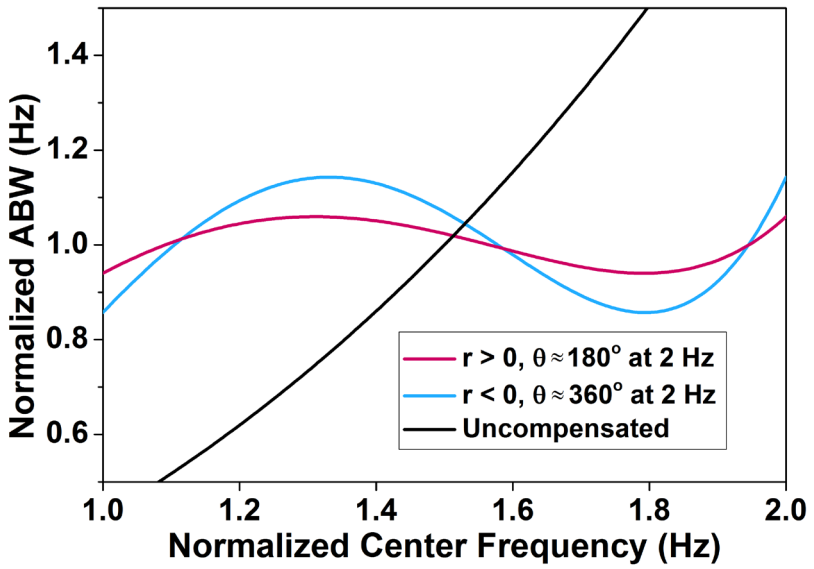

Fig. 5.8. Frequency variation of coupling coefficient for 180° and 360° transmission lines.

elements of opposite sign, which requires a transmission line which is ~360° at f_{max}. It is evident that significantly less bandwidth variation can be obtained when coupling elements of the same sign are used. This is because compared to a nominally 180° transmission line, the nominally 360° transmission line experiences twice as much variation in phase over a given frequency tuning range, and the shaping factor F is therefore more non-linear and less effective at compensating for the linear frequency dependence of the coupling element. Because of this it is always desired, if possible, to use coupling elements of the same sign so that a <180° transmission line can be used. This might not always be possible however, especially at high frequencies or when using high-permittivity substrates (such as [109] and [82]) which could make it physically impossible to realize a transmission line which is less than 180° between the coupling elements. Fig. 5.8 shows the frequency dependence of the coupling coefficient when a 360° transmission line is used compared to that of the 180° structure.

5.2.2 Phase Variation

A two-pole absorptive bandstop filter (e.g. [23]) implemented using the coupling topology of Fig. 5.1(a) has the structure shown in Fig. 5.9(a). A transmission line of

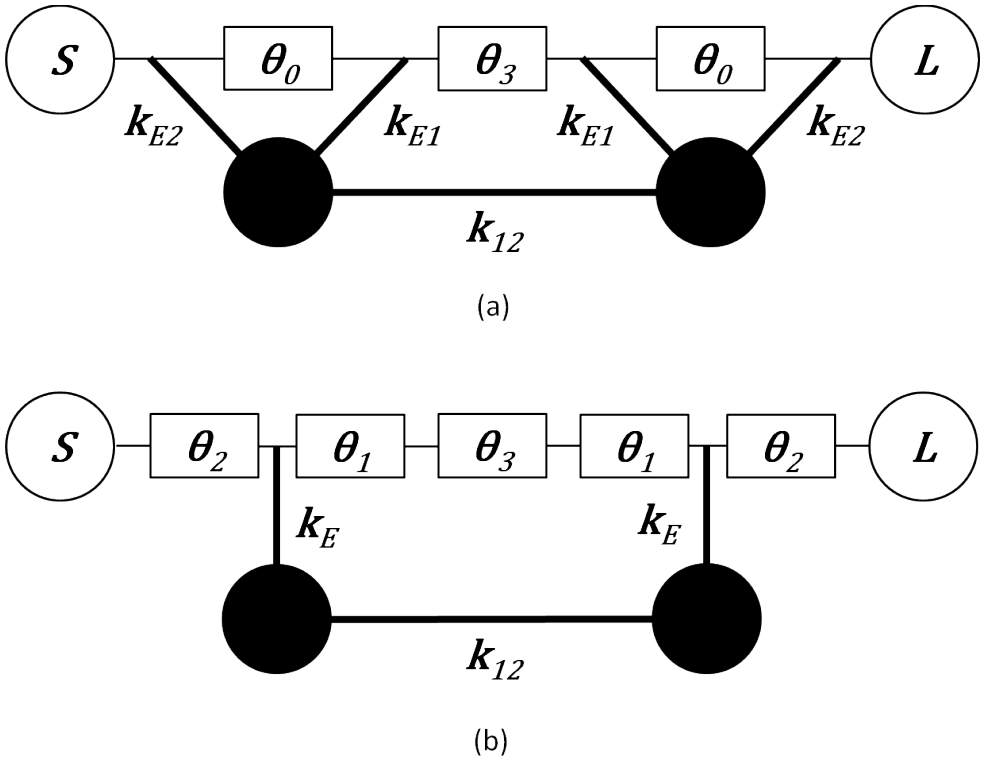

Fig. 5.9. (a) Topology of a two-pole bandstop filter using the constant-bandwidth coupling structure of Fig. 5.1(a). (b) Topology from (a) using equivalent circuit for coupling structure from Fig. 5.1(b)

length θ_3 must be inserted between the two resonators in order to provide a 90° phase between the resonators, as is required for a symmetric bandstop response [94]. Replacing the twice-coupled resonators in Fig. 5.9(a) with their equivalent circuits (Fig. 5.1(b)) yields the circuit of Fig. 5.9(b), showing that the phase contributed by the constant-coupling structure must be taken into account when selecting the length of transmission line θ_3. If equation (5.5) is substituted into equation (5.3), the equation for θ_1 can be reformulated as follows:

$$\theta_1 = \frac{1}{2}\left(\pi - \arg\left(-\frac{r + e^{-j\theta_0}}{r + e^{j\theta_0}}\right)\right) \tag{5.11}$$

while equation (5.4) for θ_2 remains the same. We see that the equivalent lengths of transmission line which define the coupling reference plane depend not only on the length of transmission line in the coupling section, but also on the ratio of the two coupling values. If we examine the frequency variation of θ_1 and θ_2 for different values of

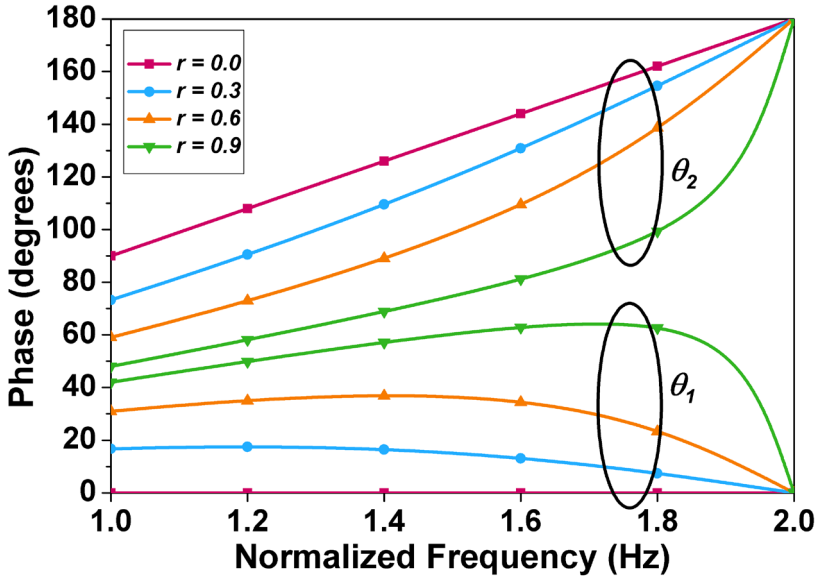

Fig. 5.10. Frequency variation of phase lengths θ_1 and θ_2 from Fig. 5.9.

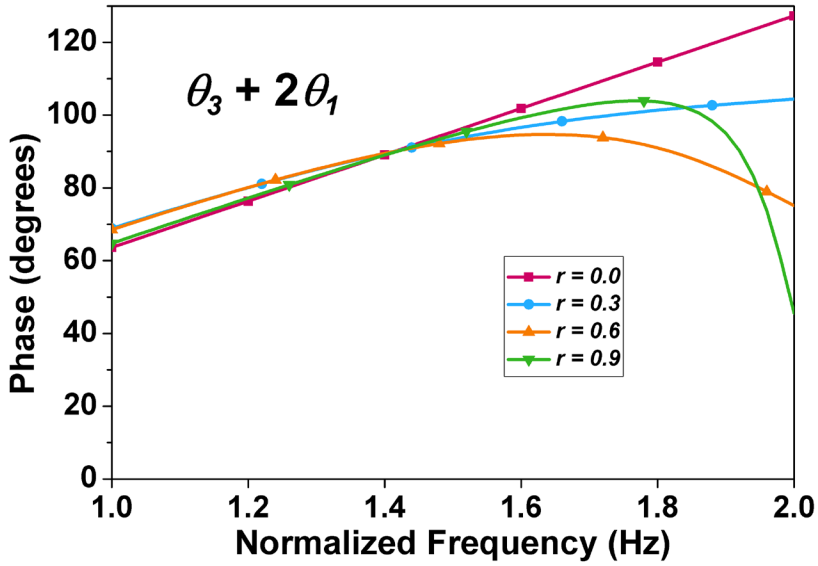

Fig. 5.11. Frequency variation of total phase between resonators, equal to θ_3 (the physical transmission line added between the resonators) + $2\theta_1$ (the phase contributed by the coupling structure)

r (plotted in Fig. 5.10), we notice that for $0^o < \theta_0 < 180^o$, the effective phase length closest to the larger of the two coupling apertures (θ_1 as shown in Fig. 5.9(b) when $|r| < 1$,) has,

for some frequencies, a negative slope versus frequency. In fact, θ_1 always becomes zero when θ_0 is equal to 180^o.

This negative phase-versus-frequency slope is very useful, as it can reduce the frequency variation of the phase length between the two resonators. The total phase between the resonators, equal to the sum of this additional transmission line length θ_3 and twice the length θ_1, has less phase variation over a given tuning range than a single length of TEM transmission line would. This is shown in Fig. 5.11. It can be seen that for a coupling ratio of r = 0, which is the case of only a single coupling aperture, the total phase between the resonators changes by 100% over an octave tuning range (63.6^o to 127.3^o) as expected because θ_1 is 0 and all of the phase between the resonators is provided by the TEM transmission line θ_3. As *r* is increased the variation in phase decreases, and can be as little as 38% (68.5^o to 94.7^o for r = 0.6). This reduction in phase variation is beneficial, as it helps the filter to maintain a symmetric transfer function when tuned over a wide frequency range.

5.3 Constant Bandwidth Filter Design

Tunable evanescent-mode cavity resonators were chosen as the technology for the filters in this work due to their well-known high unloaded quality factors and wide tuning ranges. This kind of resonator consists of a substrate-integrated waveguide cavity loaded with a capacitive post which is connected to the bottom of the cavity. A small gap is left between the post and the top of the cavity, which approximates a parallel-plate capacitor and gives a method for tuning the frequency of the resonator if the ceiling of the cavity can be displaced by an actuator, such as a piezoelectric disc [81] or an electrostatically-actuated MEMS diaphragm [80]. The features and design of these resonators will not be further discussed here because of the abundance of information available in open literature [72], [77], [110].

Five filters were designed in order to validate the efficacy of the method described in Section II. Filter A is a 1.25% constant FBW filter with a 3-6 GHz tuning range. Filter B is a 53 MHz constant ABW filter with a 3-6 GHz tuning range. Filter C is a 53 MHz constant ABW filter with a 3.5-5.5 GHz tuning range in order to demonstrate that much

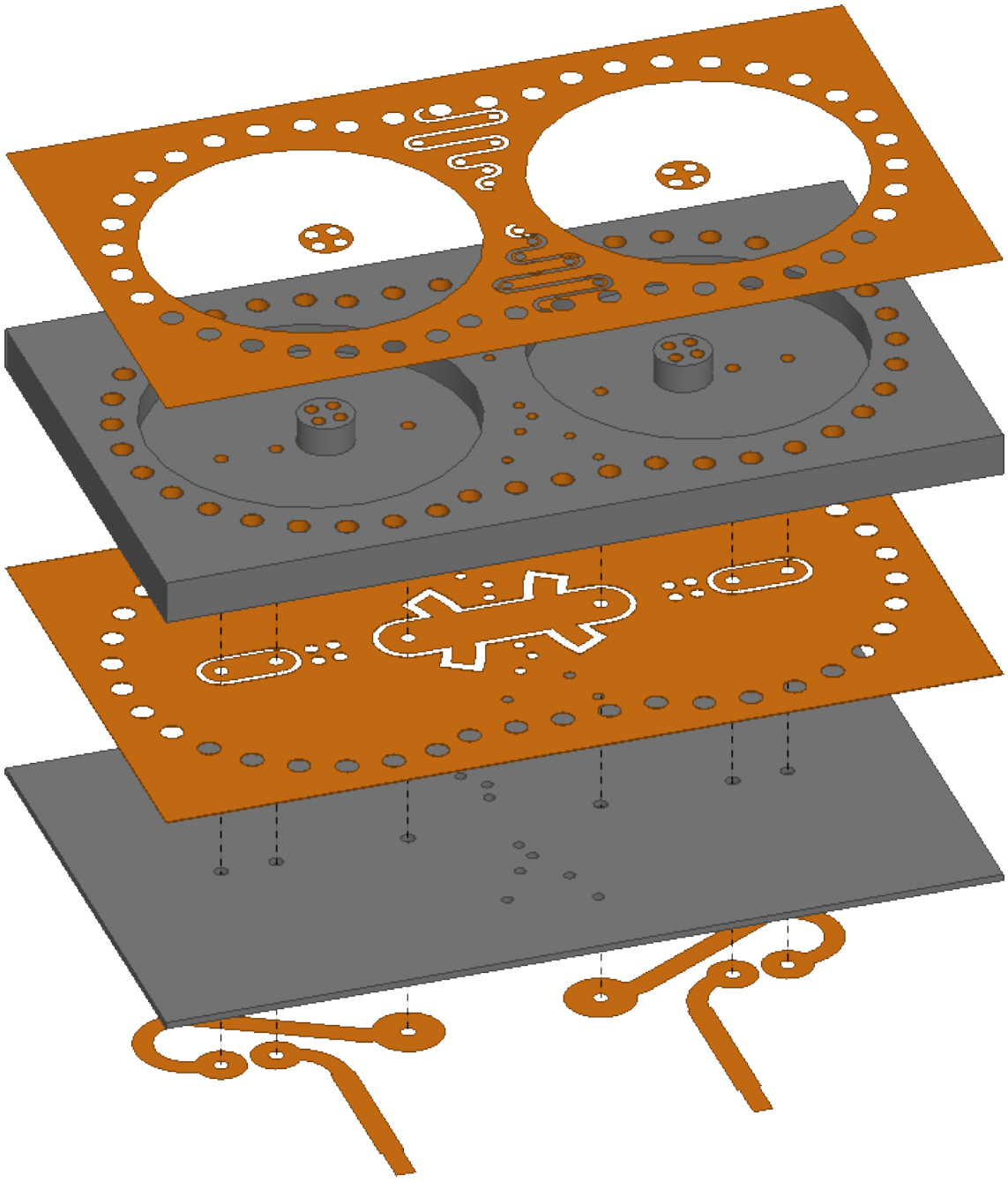

Fig. 5.12. Exploded view of the designed two-pole constant-bandwidth filters.

less bandwidth variation can be obtained over a smaller tuning range. Filter D is a 4-pole filter consisting of a back-to-back cascade of two Filter C's. Filter E is an uncompensated filter which does not use the presented constant-bandwidth coupling method, but instead uses a single coupling element. This filter allows for a fair evaluation of the performance

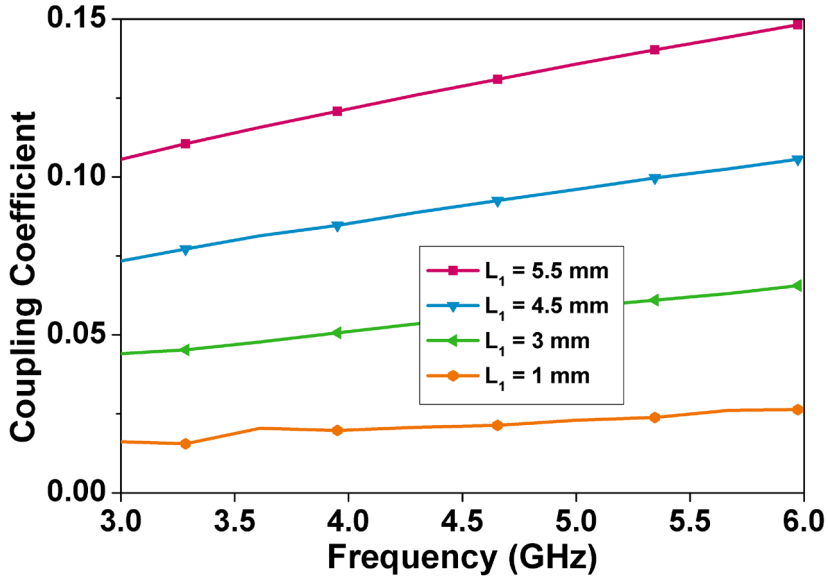

Fig. 5.13. Frequency variation of the coupling coefficients k_{E1} for various lengths L_1.

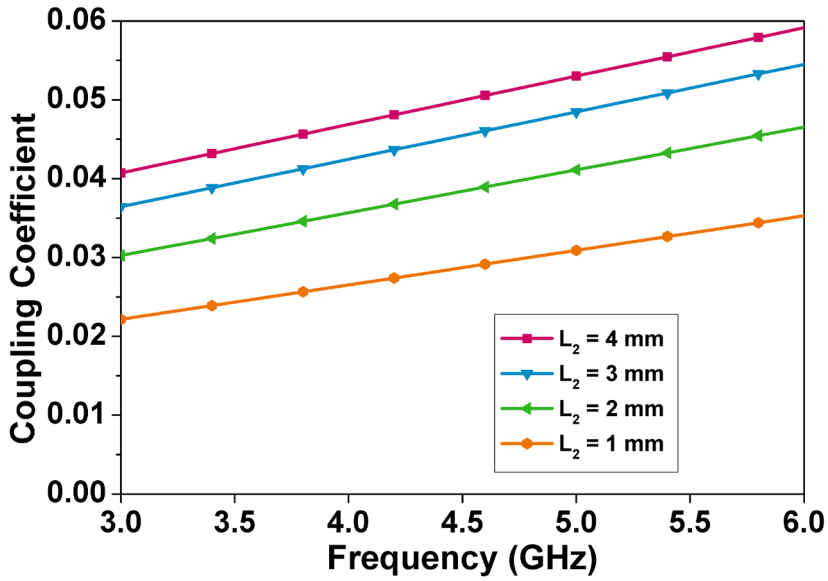

Fig. 5.14. Frequency variation of the coupling coefficients k_{E2} for various lengths L_2.

gained by using the constant-bandwidth coupling structure. To improve the performance of the filter (namely, to increase the amount of stopband rejection), an absorptive bandstop filter design is used [23]. By choosing the external coupling coefficient greater than $\sqrt{2/Q_U}$, and the interresonator coupling coefficient $k_{12} \approx 1/Q_U$, where Q_U is the

unloaded quality factor the constituent resonators, the filter can achieve theoretically infinite stopband attenuation even with finite-Q_U resonators.

5.3.1 External Coupling

The filter proposed in this work uses a coupling structure in which the microstrip feeding line is transferred to a coplanar waveguide (CPW) transmission line embedded in the ground plane, which is shared with the cavity. This structure is shown Fig. 5.12. The magnetic field of this section of CPW couples with the magnetic field of the cavity, realizing the desired external coupling. The strength of the coupling depends on both the length and width of the section of CPW line embedded in the cavity's ground plane. To increase the coupling coefficient, radially-oriented stubs can also be added to this section of CPW line in order to increase the area of the CPW section inside the cavity. Fig. 5.13 shows the frequency dependence of the coupling coefficient k_{E1} produced by this coupling structure for various lengths of the CPW section and angles of radial stubs (L_1 and φ in Fig. 5.16). can be seen that the coupling coefficient is roughly linear with respect to frequency and increases by about 50% over an octave tuning range, which justifies the model used for the coupling coefficients used in Section 5.2.

The required value of k_{E2} is much smaller than k_{E1}, so a narrower and shorter length of CPW coupling line was used. This is the dimension L_2 in Fig. 5.16. The frequency dependence of this coupling element is shown in Fig. 5.14 for different lengths of CPW.

5.3.2 Polarity of External Coupling Structures

As can be seen from Fig. 5.2, the relative sign of the external coupling elements must be known in order to design a constant-bandwidth coupling structure. If a cavity using the coupling structure just described is excited with a signal from the left side of the structure and the excitation is de-embedded such that the reference plane is in the middle of the coupling section, as shown in Fig. 5.15, the magnetic field in the cavity aligns with the magnetic field of the transmission line and is oriented in an counter-clockwise direction. However, if the coupling section is placed on the opposite side of the cavity and the same excitation is applied, again de-embedding the reference

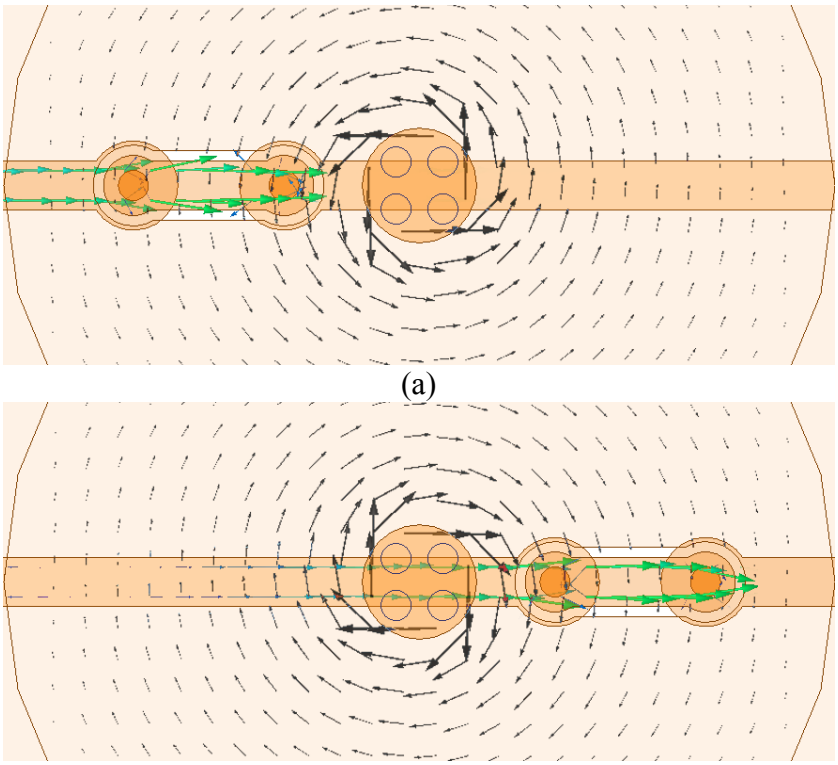

(a)

(b)

Fig. 5.15. Current density on the microstrip line (green arrows) and magnetic field inside the cavity (black arrows) when the incident signal propagates (a) from the outside of the cavity to the inside, and (b) from the inside of the cavity to the outside. Because the magnetic field has the opposite direction in the two cases, the sign of the coupling for the two cases is opposite.

plane to the center of the coupling element, the magnetic field in the cavity has the opposite orientation. From this we see that two coupling structures with exactly the same shape can yield opposite sign of coupling depending on the direction of signal propagation across the coupling section with respect to the orientation of the cavity.

It is then evident that if one wishes to use a nominally-180^{o} transmission line in the coupling structure in order to minimize bandwidth variation, the two coupling elements must provide the same polarity of coupling and thus the coupling sections must be oriented such that the direction of signal propagation across each element is the same: either from inside of the cavity to outside the cavity, or outside the cavity to the inside. To accomplish this the transmission line between the coupling elements is looped around the smaller coupling section, so that for both coupling elements a signal launched from the input will propagate from the inside of the cavity to the outside.

With the knowledge of the frequency-dependent couplings values k_{E1} and k_{E2} and the length of transmission line between them, equation (5.2) was used to optimize the structure in order to minimize the change in coupling coefficient for Filter A, and absolute bandwidth for Filters B-D across the filters' tuning ranges. The final dimensions of L1 and L2 are shown in Fig. 5.16.

5.3.3 Interresonator Coupling

Interresonator coupling between evanescent-mode cavity resonators is typically realized by a coupling iris consisting of a below-cutoff section of substrate-integrated waveguide. When this is used to realize an absorptive bandstop filter, a 270^o length of transmission line between the resonators is needed in order to achieve destructive signal interference and provide very high levels of stopband attenuation ([45], [53]). It would be preferable to be able to use a 90^o length of transmission line, as this would result in less passband insertion loss but more importantly would yield a wider tuning range over which the filter is able to achieve high stopband rejection, because the required phase relationship between the interresonator coupling and the transmission line can be upheld over a wider tuning range. This requires the interresonator coupling to take on the opposite sign.

The method used in this filter is derived from the methods for achieving negative interresonator coupling presented in [46] and [111]. An array of vias is used to connect the top and bottom conductors of the coupling iris section together, and a slot is cut into the copper of the upper conducting layer. This slot blocks the current flowing on the top conductor, and re-routes it onto the bottom conductor through the vias. This effectively reverses the direction of the current in the coupling section, which in turn yields a coupling value which is opposite of that from the original coupling iris. The interresonator coupling dimensions, such as the spacing between the vias and the width of the coupling iris, were determined through full-wave electromagnetic simulations in order to yield the coupling required for the absorptive bandstop filter ($k_{12} \approx 1/Q_U$). The final dimensions are listed in Fig. 5.16.

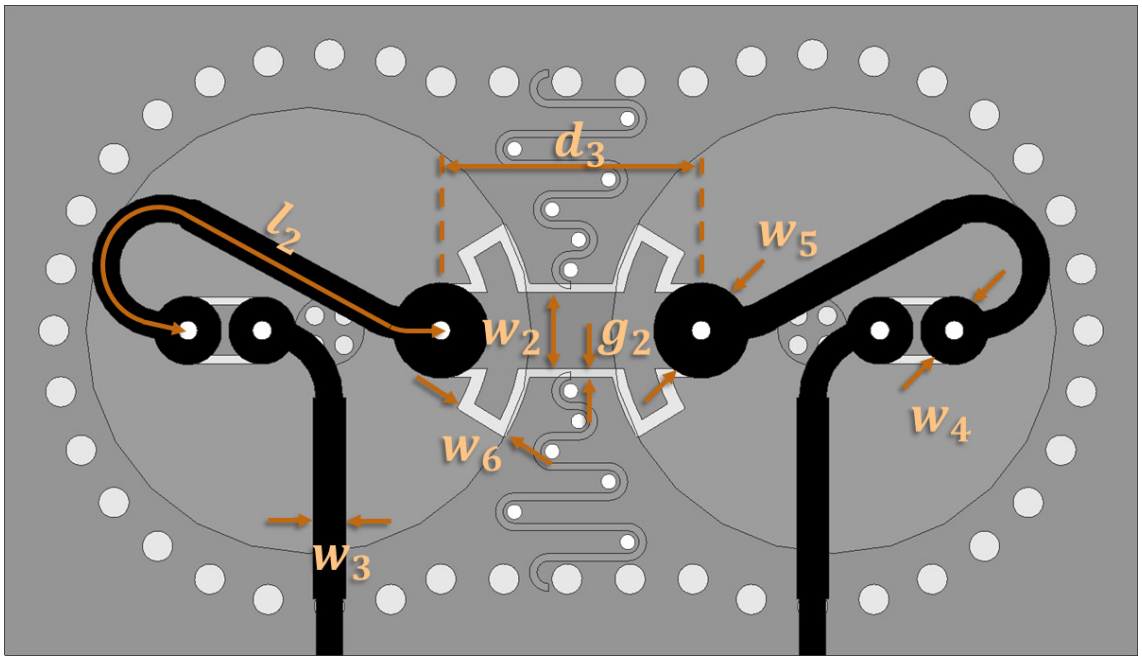

(a)

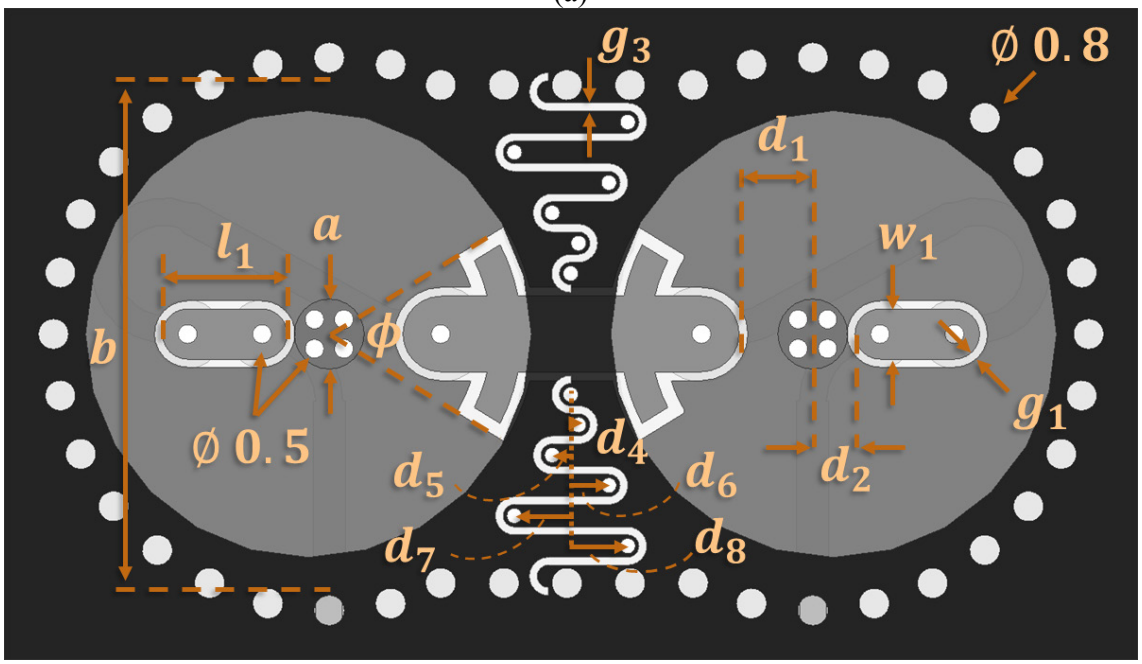

(b)

Fig. 5.16. Layout of Filters A, B, and C. Dimensions are shown below (in millimeters) and in Table 5.1 1. $a = 1.9, b = 13.8, d_4 = 0.2, d_5 = 0.5, d_6 = 1, d_7 = 1.5, d_8 = 1.5, g_3 = 0.15, w_3 = 0.86$.

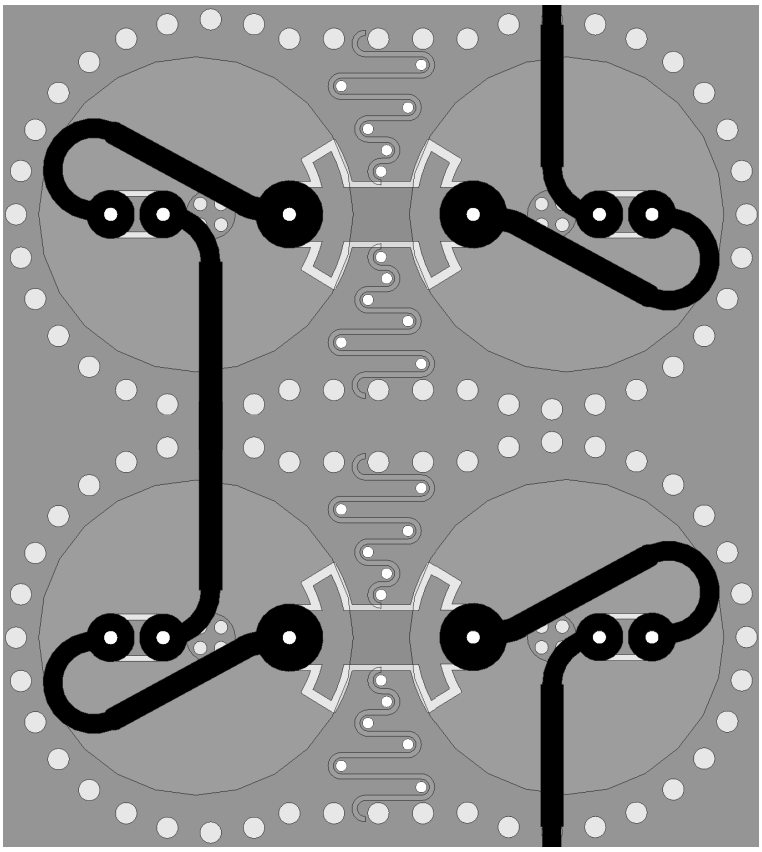

Fig. 5.17. Layout of 4-pole, comprising two cascaded Filter C's.

Table 5.1. Summary of dimensions of the designed filters in millimeters.

Filter	d_1	d_2	d_3	g_1	g_2	l_1	l_2
A	0.71	2.0	10.2	0.21	0.24	2.35	14.0
B	1.8	1.11	6.9	0.19	0.23	3.3	13.7
C	1.8	1.29	7.0	0.19	.23	3.13	14.3
	φ	w_1	w_2	w_4	w_5	w_6	
A	0^o	1.0	1.9	1.4	2.0	---	
B	63^o	1.33	2.2	1.83	2.61	1.5	
C	63	1.33	2.2	1.83	2.61	1.5	

5.4 Fabrication and Measurements

The filters were fabricated using a commercial PCB milling, laminating, and plating system. The signal and cavity substrates were made out Rogers 5880, and were laminated together using Rogers 2929 bondply material. 12.7 mm diameter piezoelectric disks (Piezo Systems T216-A4NO-273X) were used as the tuning elements. The disks

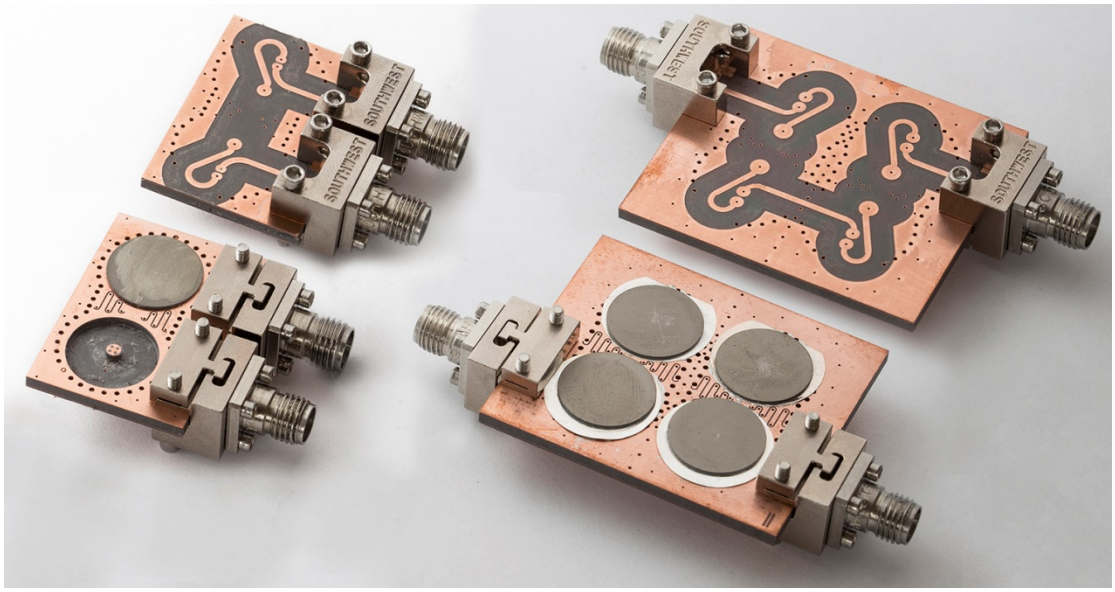

Fig. 5.18. Photograph of the fabricated filters

were copper plated and attached on top of the cavities using low-temperature solder paste. The fabricated filters are shown in Fig. 5.18. A ± 200 V voltage source was used to bias the piezoelectric discs.

5.4.1 Constant FBW Filter

Fig. 5.19 shows the measured response of Filter A when tuned to 4.8 GHz. The filter has over 70 dB of stopband rejection due to the absorptive filter design, and the passband is low-loss and well-matched, with better than 15 dB of passband return loss and less than 0.5 dB of insertion loss up to 7 GHz.

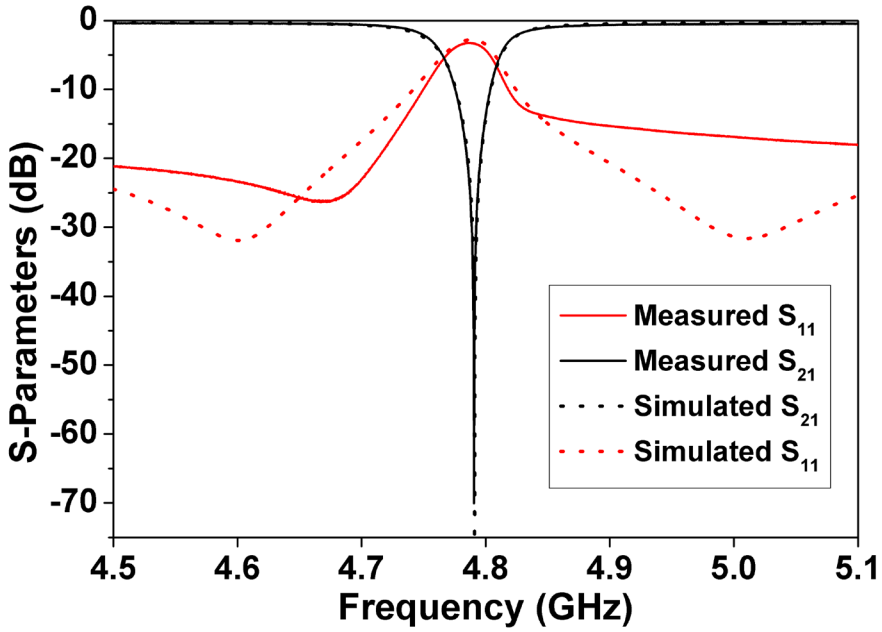

Fig. 5.19. Measured response of Filter A when tuned to 4.8 GHz.

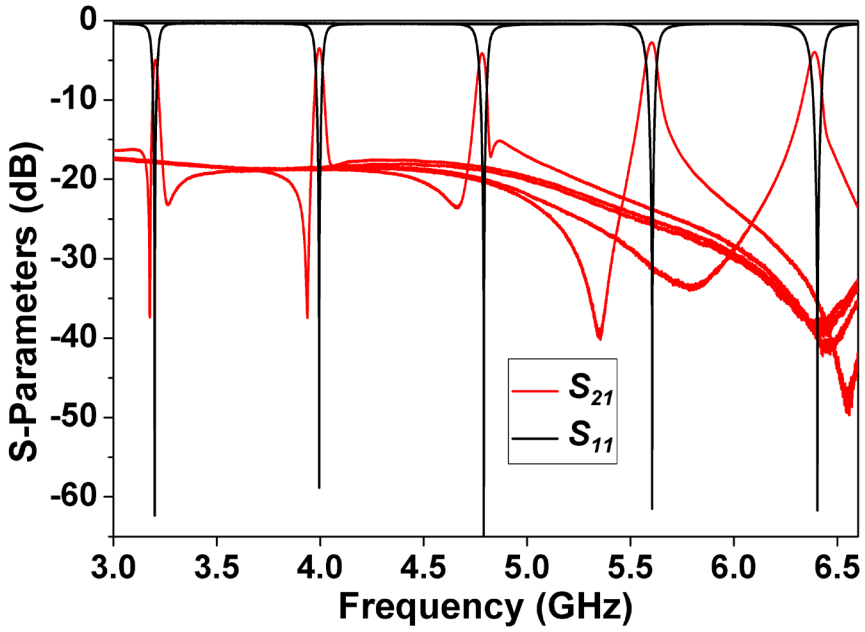

Fig. 5.20. S-parameters of Filter A when tuned across its octave tuning range.

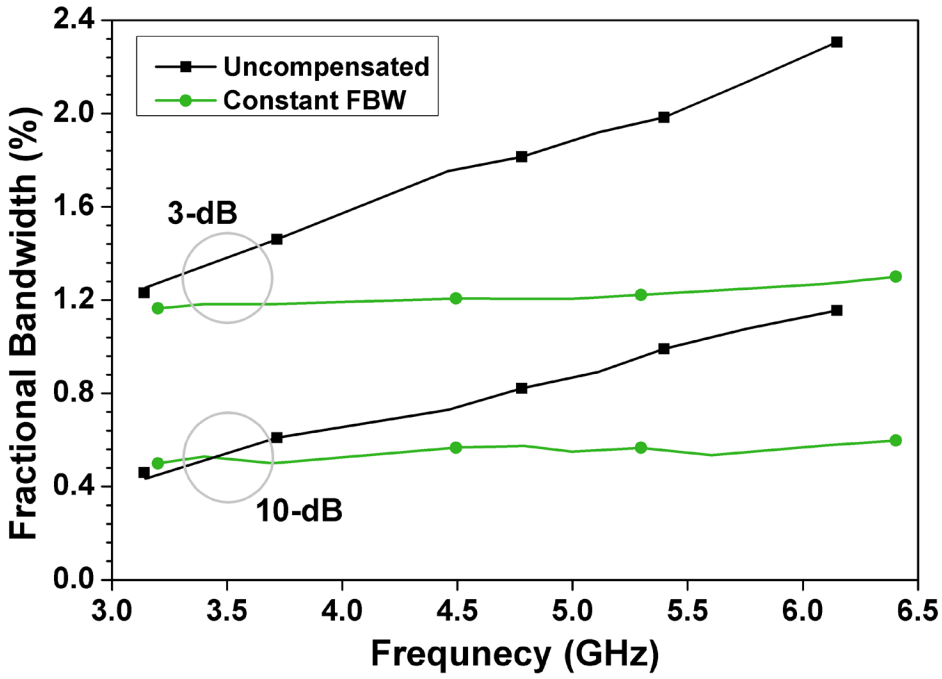

Fig. 5.21. Measured 3- and 10-dB fractional bandwidths of Filter A, compared to that of the uncompensated Filter E.

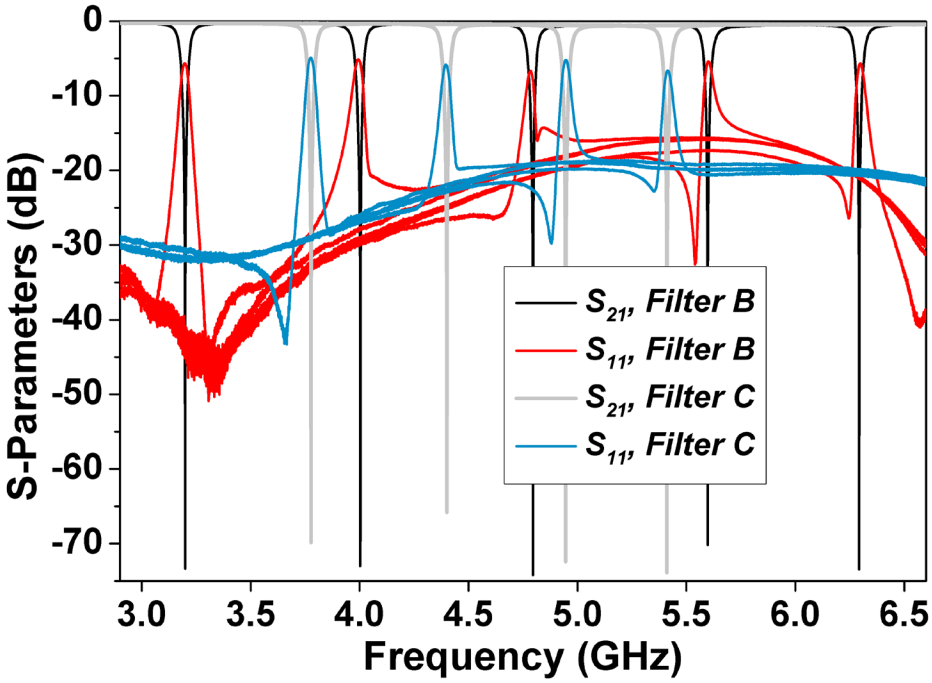

Fig. 5.22. Measured S-Parameters of Filters B and C (constant absolute bandwidth filters with 2:1 and 1.5:1 tuning ranges, respectively).

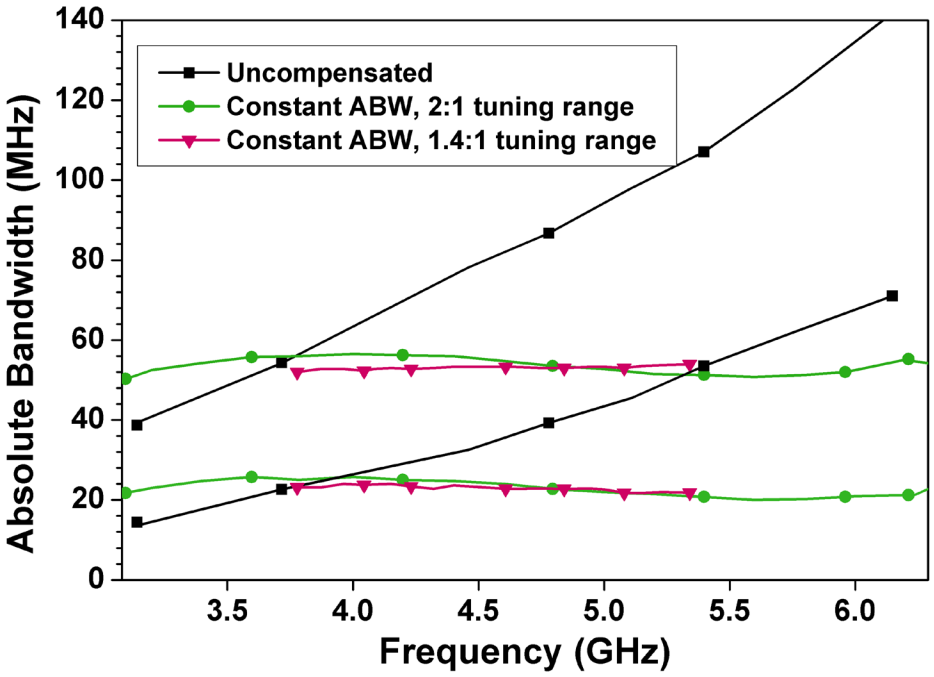

Fig. 5.23. Measured 3- and 10-dB bandwidths of Filters B and C (constant absolute bandwidth filters with 2:1 and 1.5:1 tuning ranges) and the uncompensated Filter E.

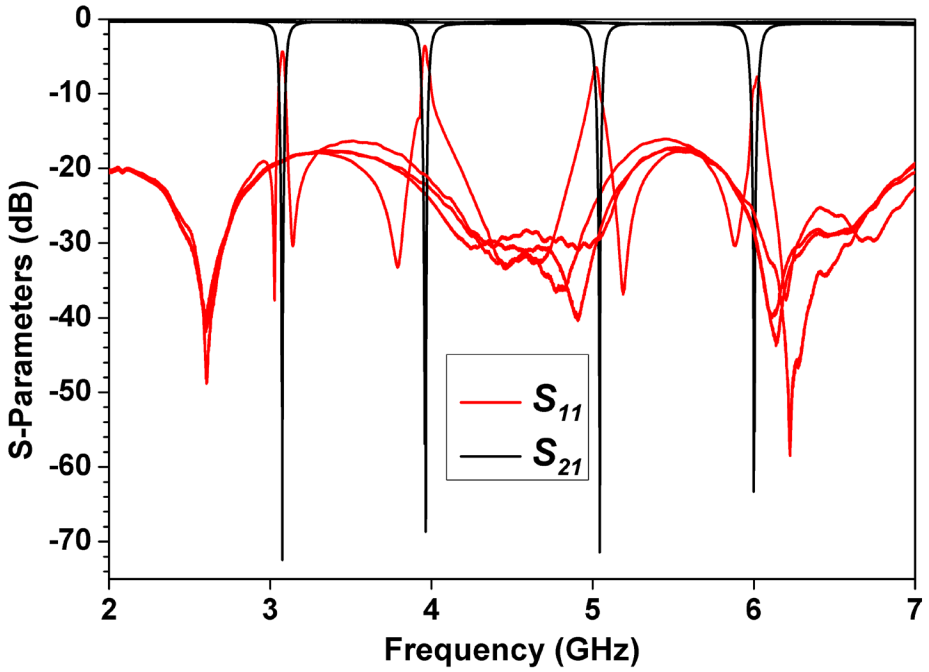

Fig. 5.24. Measured S-Parameters of 4-pole constant absolute bandwidth filter, with notches synchronously tuned in order to maintain maximum stopband attenuation.

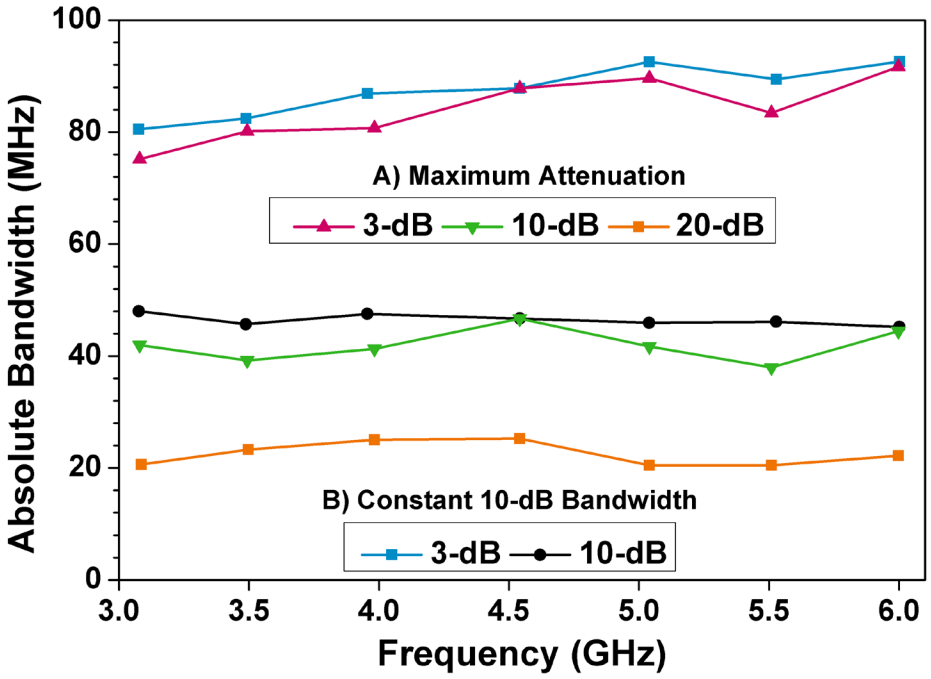

Fig. 5.25. Measured bandwidth versus center frequency for the 4-pole filter in two states: A) both notches are synchronously tuned in order to provide maximum attenuation, and B) the notches are asynchronously tuned in order to maintain a constant 20-dB bandwidth.

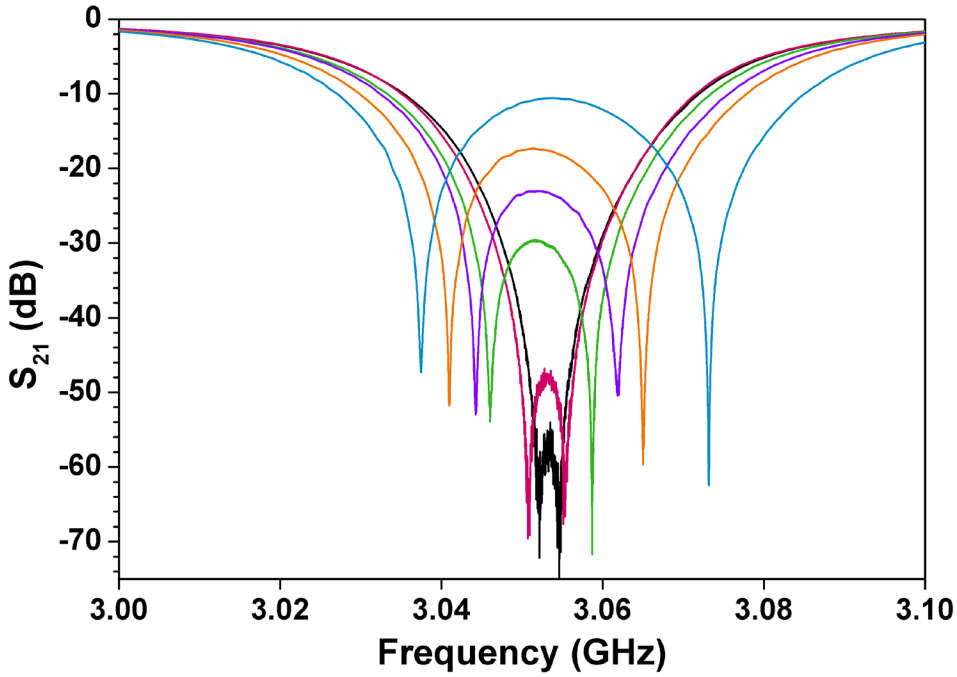

Fig. 5.26. Measured response of 4-pole filter when tuned to different levels of stopband ripple and increased bandwidth.

The performance of Filter A when tuned across its octave tuning range is shown in Fig. 5.20. It tunes from 3.2 – 6.4 GHz, maintaining over 60 dB of stopband rejection for all tuning states.

In order to investigate the relative improvement gained by the constant-bandwidth coupling method, the 3-dB and 10-dB bandwidths of both the uncompensated filter (Filter E) and the constant FBW filter (Filter A) were measured across their tuning ranges, and are shown in Fig. 5.21. The uncompensated filter's 3-dB and 10-dB bandwidths vary from 1.25% to 2.3% (an 84% variation) and 0.43% to 1.16% (a 170% variation), respectively. The constant FBW filter has greatly reduced bandwidth variation, however, with a 1.16% to 1.3% 3-dB bandwidth (a 12% variation) and a 0.5% to 0.6% 10-dB bandwidth (a 20% variation). Compared to the uncompensated filter, the constant-FBW filter has an 86% reduction in 3-dB FBW variation and an 88% reduction in 10-dB FBW variation.

5.4.2 Constant ABW Filters

The two filters optimized for constant absolute bandwidth, one over a 2:1 tuning range (Filter B) and the other over a 1.5:1 tuning range (Filter C), were measured. Their S-parameters are plotted in Fig. 5.22.

The measured ABW of both filters, along with that of Filter E, are shown in Fig. 5.23. The 3-dB and 10-dB bandwidths of the uncompensated Filter E are 39 to 142 MHz (a 264% variation) and 14.4 to 71 MHz (a 393% variation), respectively. The filter optimized for constant bandwidth over a 2:1 tuning range (Filter B) experiences much less bandwidth variation, and has a 50.3 to 56.5 MHz 3-dB bandwidth (a 12.3% variation), and a 20 to 25.8 MHz 10-dB bandwidth (a 29% variation). Compared to the uncompensated filter, Filter B realizes a 95% reduction in 3-dB bandwidth variation, and a 93% reduction in 10-dB bandwidth variation.

The filter optimized for a 1.5:1 tuning range experiences even less bandwidth variation, and has a 52 to 54 MHz 3-dB bandwidth (a 3.8% variation), and a 21.8 to 24 MHz 10-dB bandwidth (a 10% variation).

Note that because the unloaded quality factors of the resonators change across the filter's tuning range, it is impossible to simultaneously minimize the 3-dB and 10-dB bandwidths. In these designs, the filters were optimized for constant 3-dB bandwidth, but the filters could be similarly optimized for minimum 10-dB bandwidth variation.

5.4.3 4-Pole Filter

The 4-pole constant absolute bandwidth filter was measured with the notches of each stage synchronously tuned in order to provide maximum attenuation. The measured 3- and 10-, and 20-dB bandwidths were measured and are plotted in Fig. 5.25. As in the case of the two-pole filters, it maintains fairly constant ABW across its octave tuning range.

Compared to the two-pole filters, the 4-pole offers an additional degree of freedom in reconfigurability, as it consists of two cascaded absorptive notch sections, and the center frequency of each notch can be controlled independently. This allows the filter to produce a variety of transfer functions, as shown in Fig. 5.26. The notches can be tuned to the same frequency in order to provide maximum attenuation, or they can be asynchronously tuned in order to provide a Chebyshev frequency response. By asynchronously tuning the notches, the bandwidth of the filter can also be tuned slightly, and it is possible to use this bandwidth tunability to compensate for any residual bandwidth variation present after applying the constant-bandwidth method presented in this chapter. Using this method, the filter was again tuned from 3 to 6 GHz while asynchronously tuning the notches in order to maintain a constant 50 MHz 10-dB bandwidth. The 10-dB bandwidth is maintained nearly perfectly constant, and is only limited by the accuracy with which the two notches are tuned. The 3- and 10-dB bandwidths are plotted in Fig. 5.25. In order to maintain constant 10-dB bandwidth, the stopband ripple varied from a minimum of -55 dB at 4 GHz to a maximum of -15 dB at 5.5 GHz.

5.4.4 Insertion Loss of Filters

Because the constant bandwidth coupling method requires additional lengths of transmission lines, it also has higher passband insertion loss compared to the uncompensated design. The passband insertion loss of all filters is shown in Fig. 5.27.

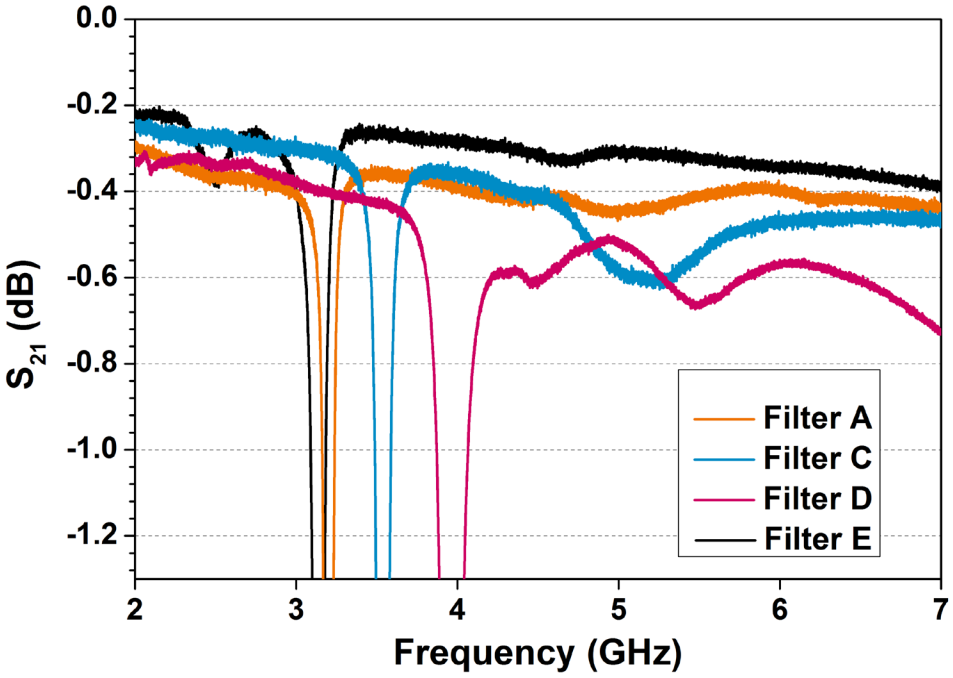

Fig. 5.27. Comparison of the insertion loss of the filters.

The uncompensated filter has 0.33 dB of insertion loss at 6 GHz, which as expected is lower than all of the other filters.. Filters A and C have approximately 0.1 dB more insertion loss than Filter E at 6 GHz, and Filter D has roughly 0.2 dB more insertion loss than Filters A and C.

5.4.5 Comparison to State-of-the-Art

In order to compare the relative effectiveness of this method of achieving constant bandwidth, Table 5.2 compares the results of the filters demonstrated in this chapter to other demonstrates of constant-bandwidth tunable bandstop filters.

5.5 Conclusion

In this chapter a new coupling method which was recently introduced in [108] was investigated in greater detail. It is shown that the coupling method can partially compensate for the frequency dependence inherent to practical coupling structures, yielding a nearly-constant coupling coefficient or a coupling coefficient which decreases with respect to frequency, in order to have constant ABW. Several design tradeoffs are investigated, and it is shown that less bandwidth variation can be obtained for narrower tuning ranges than for larger tuning ranges. To validate the theory and design principles, several filters were designed, fabricated and measured: a constant FBW filter with a 1.16% to 1.3% 3-dB bandwidth; a constant ABW filter with an octave tuning range and a 50.3 to 56.5 MHz 3-dB bandwidth; a constant ABW with a 50% tuning range and a 52 to 54 MHz 3-dB bandwidth; and a constant ABW 4-pole filter which can maintain a constant 50 MHz 10-dB bandwidth.

Table 5.2. Comparison of our work to existing state-of-the-art constant-absolute-bandwidth tunable bandstop filters.

Ref.	Technology	Tuning Range	ABW Variation
[8]	Lumped-element	2.75 : 1	~20%*
[11]	Lumped-element	2.42 : 1	~40%*
[18]	Microstrip	1.93 : 1	24%*
[106]	Microstrip	1.27 : 1	10%†
Filter B	3-D cavity	2.0 : 1	12.3%*
Filter C	3-D cavity	1.5 : 1	3.8%*

* = 3-dB bandwidth † = 20-dB bandwidth

6. HIGH-Q, WIDELY-TUNABLE BALANCED-TO-UNBALANCED (BALUN) FILTERS

6.1 Introduction

Differential circuits are extremely common in today's communication systems, which have stringent requirements on crosstalk, noise immunity, linearity, and other kinds of signal degradation. In order to allow differential circuits to interface with single-ended circuits, balanced-to-unbalanced transformers (baluns) are commonly used. An ideal balun has a single-ended input and generates a differential output, consisting of two outputs which are equal in magnitude and 180^{o} out of phase. Because practical baluns add size and loss to a circuit, it would be beneficial to integrate them with other devices if possible to reduce size and loss. Bandpass filters are commonly placed either immediately before or after baluns in a receiver chain, and thus a significant amount of research effort has recently been devoted to developing filters with integrated balun functionality. Fig. 6.1 illustrates the concept of replacing a filter/balun cascade with a balun filter – a bandpass filter with a single-ended input and a balanced output.

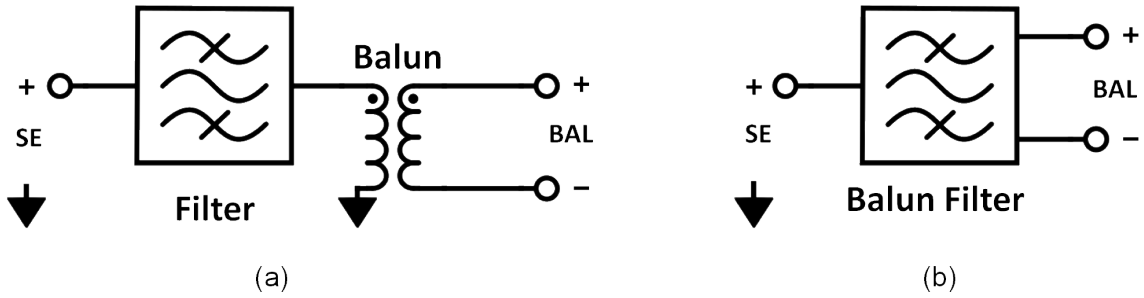

Fig. 6.1. (a) A commonly-encountered situation in microwave systems: a bandpass filter followed by a balun. (b) An integrated balun filter which combines the functionality of both the bandpass filter and the balun. SE denotes the single-ended port, and BAL denotes the balanced port.

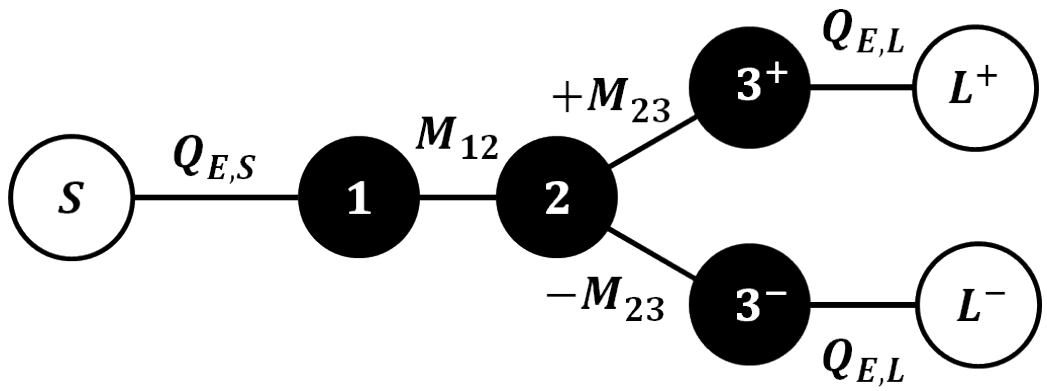

Fig. 6.2. The most common method of implementing a balun filter. The 180° phase difference between the balanced output ports is achieved by utilizing positive interresonator coupling in one path to the output, and using negative coupling in the other path.

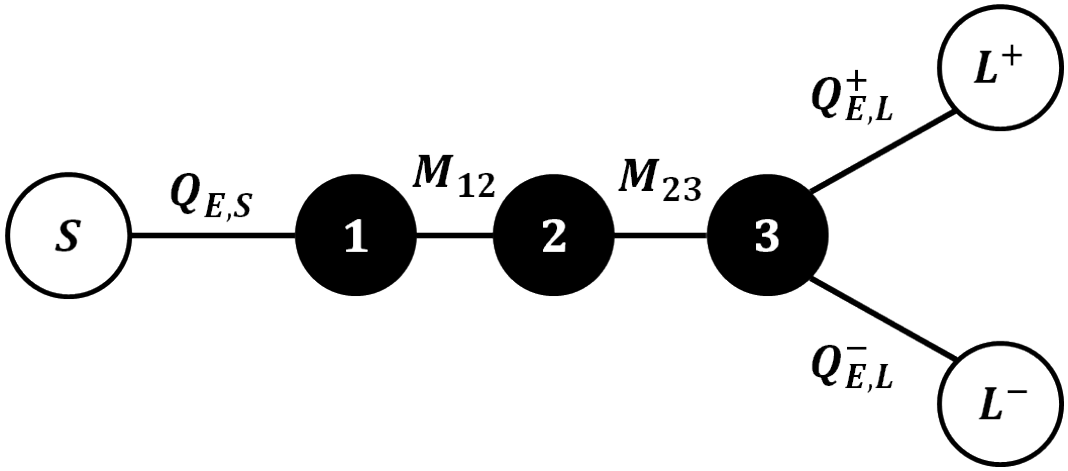

Fig. 6.3. A less common topology for realizing balun filters. The 180° phase difference is realized by coupling the last resonator to two different outputs, using positive/negative external. coupling

In order for a filter to realize an ideal differential output, it must contain two paths from input to output which are equal in magnitude but are 180° out of phase. If using coupled resonators to construct the filter, the 180° phase shift can be realized by reversing the sign of one of the coupling elements in one of the output paths. A common way that this is accomplished is shown in Fig. 6.2, in which a three-pole balun filter is realized by replacing the third resonator with two resonators, each of which is coupled to the second resonator with coupling elements which are equal in magnitude but opposite in sign. Examples of filters implemented in this way can be found in [112]–[115] This

configuration does provide the behavior of a filter cascaded with a balun, but it is unnecessarily large as it contains a redundant resonator (4 resonators are required to realize a 3rd order filter response), and the amplitude and phase balance at the output are strongly dependent on how well resonators 3^+ and 3^- are matched in resonant frequency and quality factor.

A better configuration is shown in Fig. 6.3, in which the 180^o phase difference between the output ports is simply realized by coupling the last resonator to two separate output ports, with external coupling elements which are equal in magnitude but opposite in sign. No redundant resonators are needed in this configuration, and the amplitude and phase balance does not depend on any resonator parameters such as resonant frequency or Q_U, but only on the amplitude/phase balance between $Q_{E,L}^+$ and $Q_{E,L}^-$. Examples of balun filters implemented with this topology can be found in [116], [117]

Despite the need for balun filters with tunable center frequencies, very few such devices have been demonstrated because of the difficulty in maintaining amplitude and phase balance between the two output ports over a wide tuning range. To the best of the authors' knowledge, [118], [119] are the only tunable balun filters published to date. The tunable balun filter in [118] uses two split-ring microstrip resonators to realize the filter. The positive/negative external coupling of Fig. 6.3 is realized by tapping opposite ends of the split-ring resonator, where the voltages have opposite polarity. The filter is tuned with varactor diodes, and has a 1.7:1 tuning range while maintaining < 0.5 dB and < 5^o of amplitude and phase imbalance. The filter in [119] uses essentially the same topology as [118], but uses a magnetically-tunable permalloy thin film as the tuning element. The filter has a 1.04:1 tuning range, and also has < 0.5 dB and < 5^o of amplitude and phase imbalance.

In this paper, we introduce for the first time a tunable balun filter implemented with high-Q evanescent-mode cavity resonators. The balun functionality is achieved by means of a new differential coupling structure which implements the positive/negative external coupling of Fig. 6.3. Evanescent-mode cavity resonators have a number of advantages over tunable planar resonators, such as higher unloaded quality factors, higher linearity, and in some cases wider tuning ranges. The new design proposed and demonstrated in

this paper has state-of-the-art performance with respect to other tunable balun filters, with < 0.2 dB and < 0.9° of in-band amplitude and phase imbalance across a 3.2 to 6.1 GHz tuning range.

6.2 Differential Coupling Structure

External coupling in evanescent-mode cavity resonator based filters is usually implemented by creating a slot in the ground plane of the cavity, which is the shared ground plane of the feeding transmission line. This aperture allows the magnetic field of the transmission line to couple with that of the cavity. The transmission line is short-circuited with a via just following the coupling aperture, in order to create maximum current and thus maximum magnetic field at the aperture.

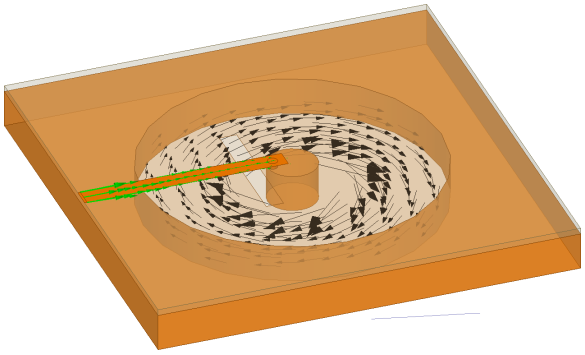

Fig. 6.4. The standard method for realizing external coupling to evanescent-mode cavity resonators in single-ended operation.

The direction of the magnetic field inside the cavity corresponds to the direction of the transmission line's magnetic field, which is determined by the direction of the transmission line's current with respect to the coupling aperture. By changing the direction of current across the coupling aperture, external couplings with opposite polarities can be realized.

Based on this concept, a differential coupling structure which consists of a U-shaped loop of microstrip transmission line crossing over a coupling aperture is proposed. The structure, shown in Fig. 6.5, is a compact realization of the two external coupling elements of Fig. 6.3, which utilizes a single coupling aperture to realize two coupling elements which have opposite polarities. This can be seen by examining the field

distributions in Fig. 2. If the resonator is excited from the right-hand port as shown in Fig. 6.5(a), the direction of current flow in the microstrip line (assuming that the length of the feed-line is negligible) is oriented radially outwards with respect to the cavity and coupling aperture, and thus induces a counter-clockwise magnetic field in the cavity. However, if the resonator is excited from the left-hand port, then the current flow is oriented radially inward with respect to the cavity, and it induces a clockwise-oriented magnetic field in the cavity. Because identical excitations from each of the two ports excite opposite-polarity voltages and currents in the cavity, the two ports are coupled to the resonator with opposite coupling polarity. This implements the differential coupling concept of Fig. 6.3.

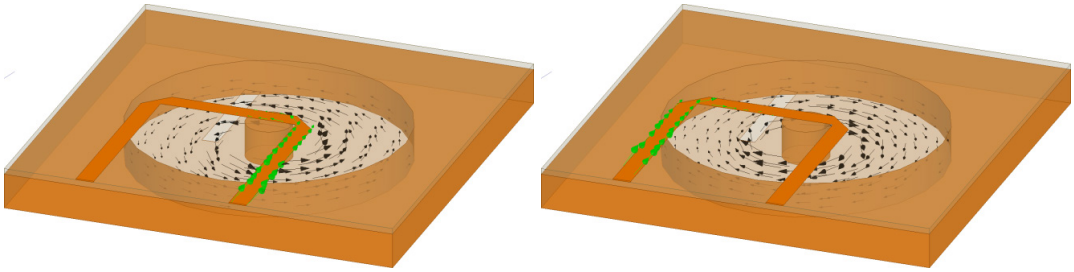

Fig. 6.5. The proposed differential coupling structure for evanescent-mode cavity resonators. An identical stimulus from either port will exciting the opposite polarity of magnetic field inside the cavity, and conversely a given resonator field distribution will induce currents 180^{o} out of phase at the two output ports.

6.3 Design

To demonstrate this concept, an octave-tunable three-pole bandpass filter was designed. Using standard coupled-resonator design procedures (e.g. [92]), the filter was designed to have a 2.4% fractional bandwidth with 15 dB return loss at the center of its tuning range. The external quality factor resulting from the differential coupling structure is somewhat different than that from the single-ended coupling structure, stemming from the fact that the single-ended coupling structure is grounded with a via, which creates maximum magnetic field at the coupling aperture, whereas the differential coupling structure is not via-grounded and thus its magnetic field

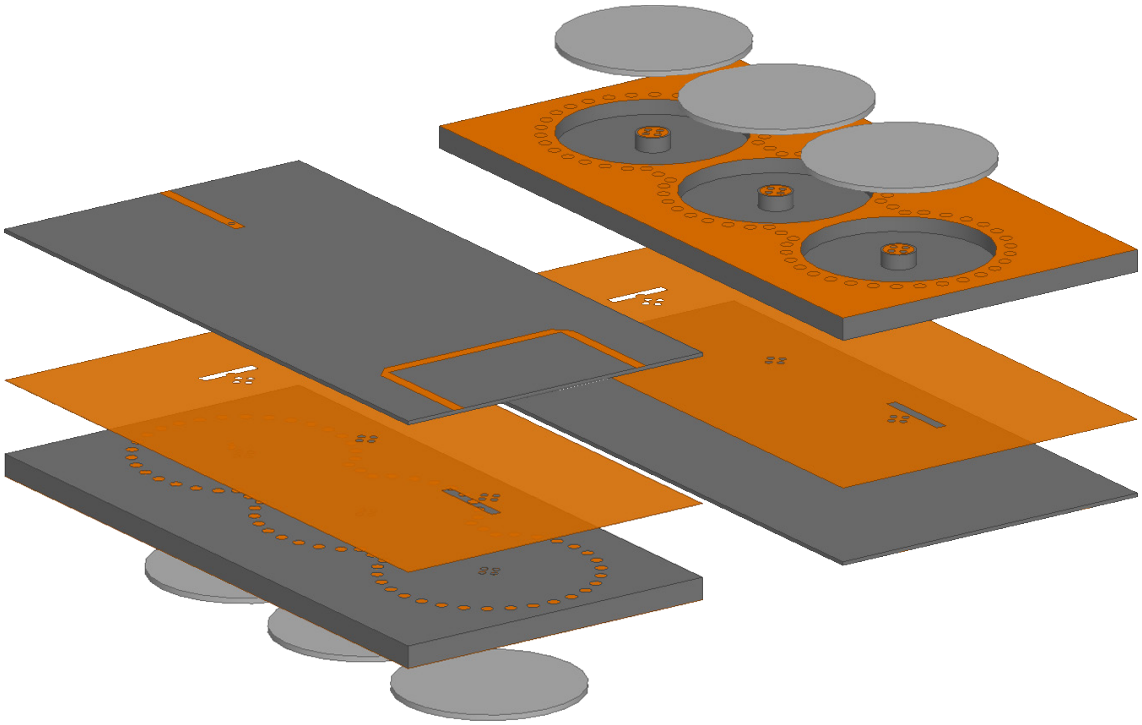

Fig. 6.6. Exploded view of the proposed 3-pole balun filter.

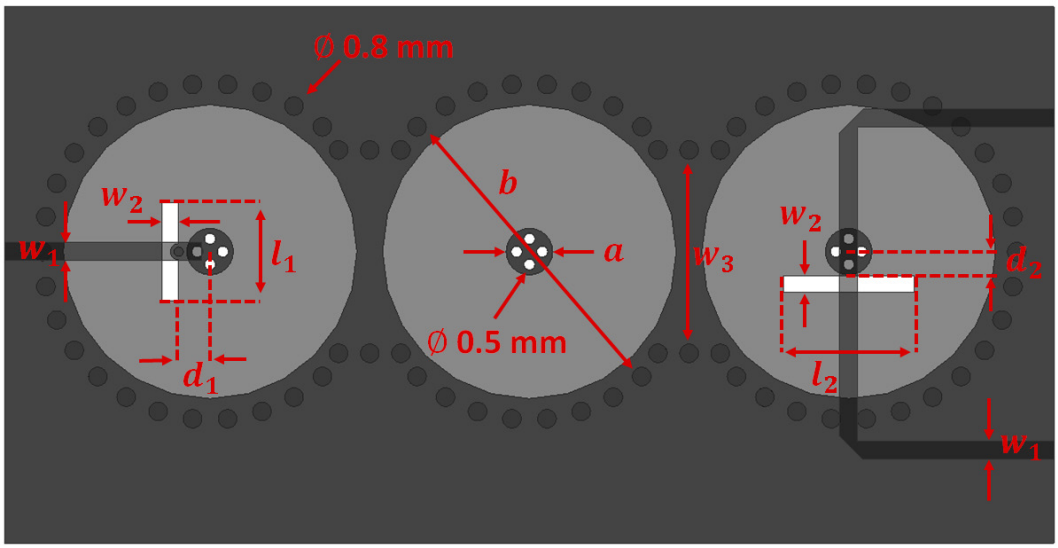

Fig. 6.7. Final dimensions of the designed balun filter. $a = 2\ mm, b = 13.6\ mm, d_1 = 1.35\ mm, d_2 = 1.05\ mm, l_1 = 4.2\ mm, l_2 = 5.6\ mm, w_1 = 0.78\ mm, w_2 = 0.7\ mm, w_3 = 8.5\ mm.$

is weaker. Fig. 6.8 plots the dependence of the external quality factors from the two coupling structures versus the length of the coupling aperture. Q_E is calculated using the

reflected group delay method [92]. In order to use this method for calculating the Q_E of the differential port, the group delay of the differential reflection coefficient S_{dd22}

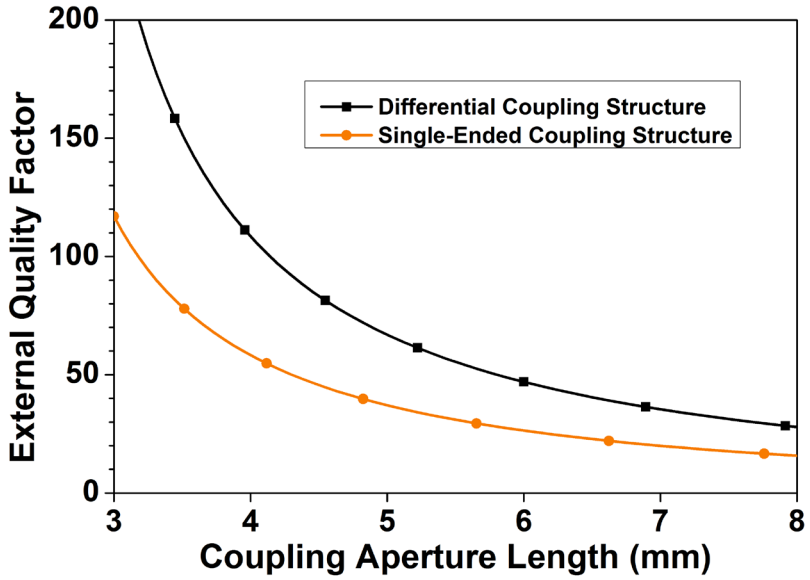

Fig. 6.8. Simulated external quality factors for the single-ended and differential coupling structures.

(equation (6.3)) is used. The required Q_E for the prescribed bandwidth and transfer function is 60, and thus the lengths of the coupling apertures for the single-ended and differential structures were chosen to be 4.2 mm and 5.6mm, respectively. An exploded view of the filter is shown in Fig. 6.6, and all final dimensions are shown in Fig. 6.7.

6.4 Experimental Validation

The filters were fabricated using a commercial PCB milling, laminating, and plating system. The signal and cavity substrates were made out Rogers 5880, and were laminated together using Rogers 2929 bondply material. 12.7 mm diameter piezoelectric disks (Piezo Systems T216-A4NO-273X) were used as the tuning elements. The disks

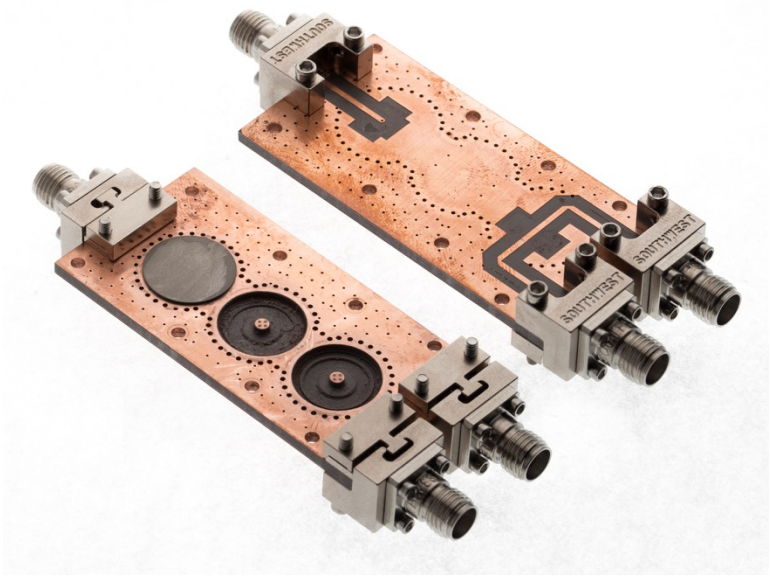

Fig. 6.9. Photograph of the fabricated filters

were metalized with thin silver membranes and attached on top of the cavities using electrically-conductive silver epoxy. The fabricated filters are shown in Fig. 6.9. Though not shown, a copper-plated lid was placed on top of the transmission-line substrate in order to increase stopband rejection by preventing parasitic coupling between the input and output microstrip lines.

3-port S-parameter measurements were conducted with a Keysight N5230C PNA, using a ± 200 V voltage source to bias the piezoelectric discs, and the mixed-mode S-parameters were calculated from these measurements. Fig. 6.10 shows the measured input reflection coefficient (S_{11}), differential transmission response (S_{ds21}), common-mode rejection (S_{cs21}), and differential output reflection coefficient (S_{dd22}) across the filter's tuning range. The mixed-mode S-Parameters are calculated as follows [117]:

$$S_{ds21} = \frac{1}{\sqrt{2}}(S_{21} - S_{31}) \tag{6.1}$$

$$S_{cs21} = \frac{1}{\sqrt{2}}(S_{21} + S_{31}) \tag{6.2}$$

$$S_{dd22} = \frac{1}{2}(S_{22} - S_{23} - S_{32} + S_{33}) \tag{6.3}$$

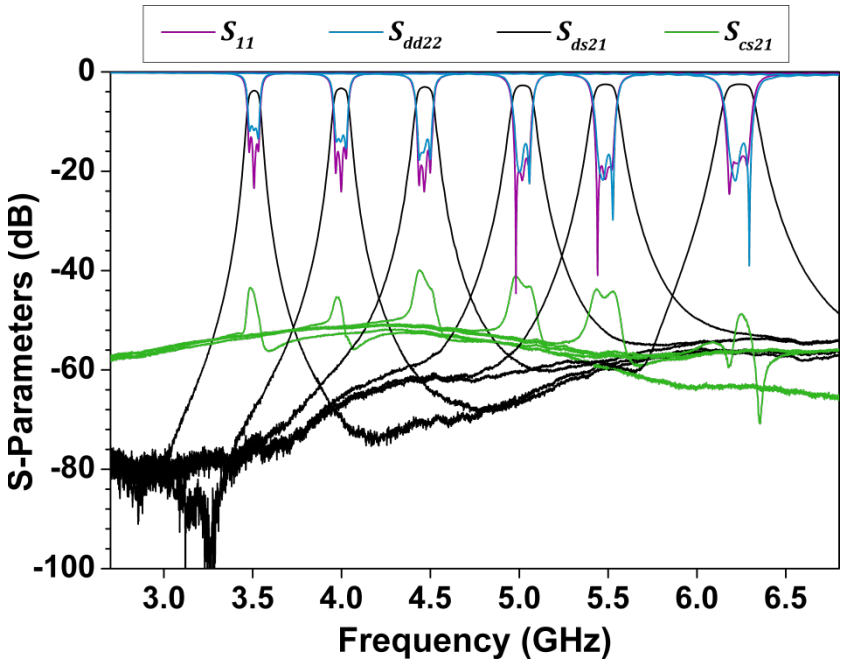

Fig. 6.10. Measured mixed-mode S-parameters of the filter without the package lid attached.

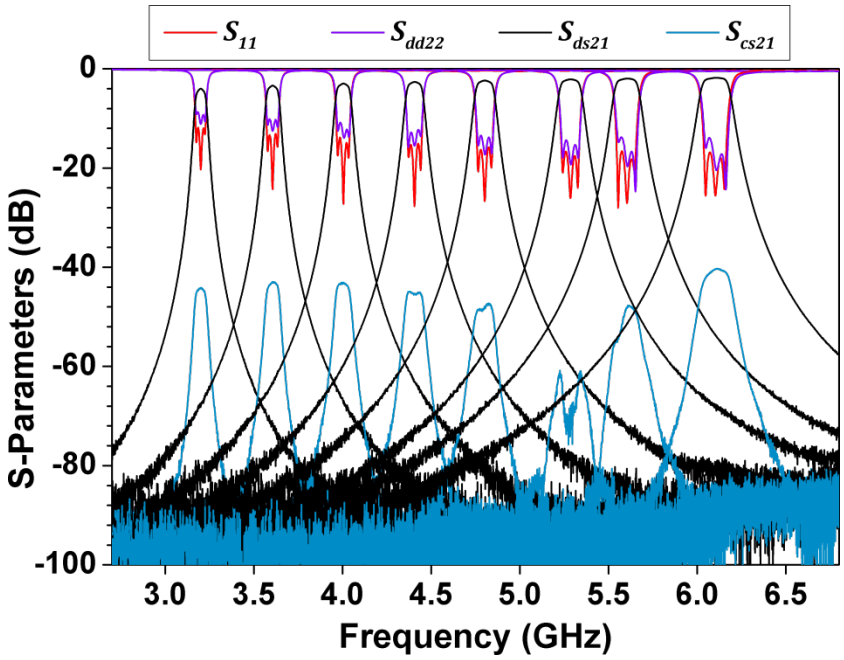

Fig. 6.11. Measured mixed-mode S-parameters of the filter with the package lid attached.

The filter tunes from 3.2 to 6.1 GHz, and its insertion loss varies from 3.9 dB to 1.8 dB (after deembedding the loss of the connectors and microstrip feed lines), its 3-dB fractional bandwidth varies from 2.0% to 2.7%. The in-band input return loss varies from 12 to 17 dB of across the tuning range. Because of its tight amplitude and phase balance,

the filter provides greater than 40 dB of common-mode rejection within its passband for all tuning states. When the filter is not packaged, the out-of-band common-mode and differential-mode rejection are limited by coupling between the input and output ports through the air. As seen in Fig. 6.10, the out-of-band common-mode rejection varies from 50 to 70 dB in the 3 to 6 GHz range, and the out-of-band differential-mode rejection varies from 60 to 80 dB across the same frequency range. The use of a package prevents this parasitic source-to-load coupling and significantly improves both the out-of-band common- and differential-mode rejection, as seen in Fig. 6.11. With the package, both the common-mode and differential-mode rejection are greater than 90 dB in the 3 to 6 GHz range, which represents a 30 to 40 dB improvement in common-mode rejection, and a 10 to 20 dB improvement in differential-mode rejection.

Two common figures of merit for baluns and balun filters are the amplitude and phase imbalance between the two ports which comprise the differential output. The amplitude imbalance, defined as $|\boldsymbol{dB}(\boldsymbol{S_{21}/S_{31}})|$, measures the balance between the magnitudes of the two output ports. Phase imbalance, defined as $|\angle \boldsymbol{S_{21}/S_{31}} - \boldsymbol{180°}|$, measures how much the phase difference between the two output ports deviates from the ideal value of 180^{o}. The amplitude and phase balance of the filter in its 5.3 GHz tuning state are shown in Fig. 6.12. It can be seen that within the filter's 10-dB bandwidth, the amplitude imbalance is less than 0.024 dB and the phase imbalance is less than 0.2^{o}. To the best of the authors' knowledge, this represents lower amplitude and phase imbalance than any other published balun bandpass filters, whether static or tunable.

The filter's maximum measured amplitude and phase balance within its 10-dB bandwidth are plotted for several tuning states across its tuning range in Fig. 6.11. Amplitude and phase imbalance measurements are not necessary outside of the filter's passband since common-mode rejection is achieved by means of the filter's stopband. The amplitude and phase imbalance vary somewhat across the filter's tuning range, but in all cases the amplitude imbalance is less than 0.2 dB, and the phase imbalance is less than 0.9^{o}. This represents state of the art performance, and the filter demonstrated in this work has less amplitude and phase imbalance than the two existing examples of tunable filtering baluns in open literature, while at the same time possessing a wider tuning range.

Table 6.1 presents a comparison of our work to prior state-of-the-art tunable and fixed balun filters.

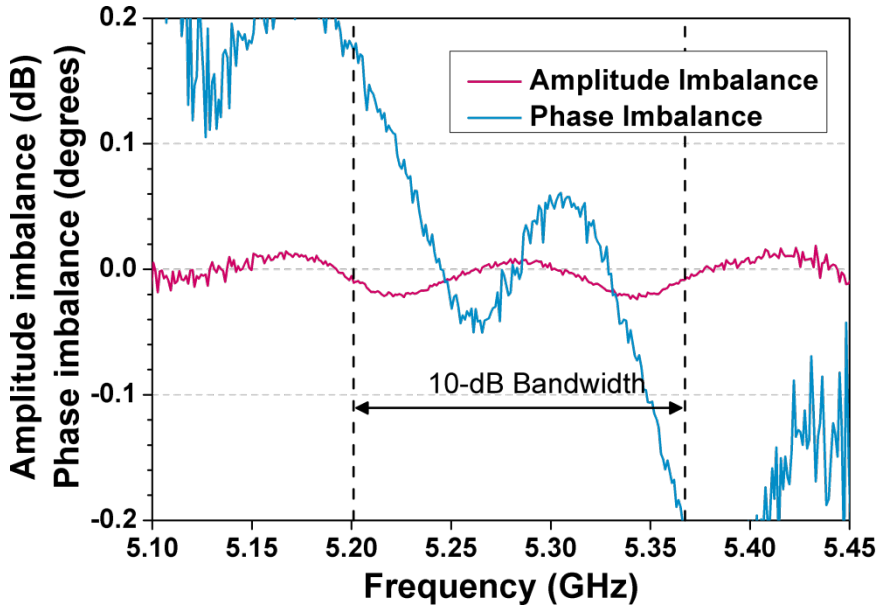

Fig. 6.12 Measured amplitude and phase balance within the 10-dB bandwidth of the filter when tuned to 5.3 GHz. The measurements are taken with the package lid attached.

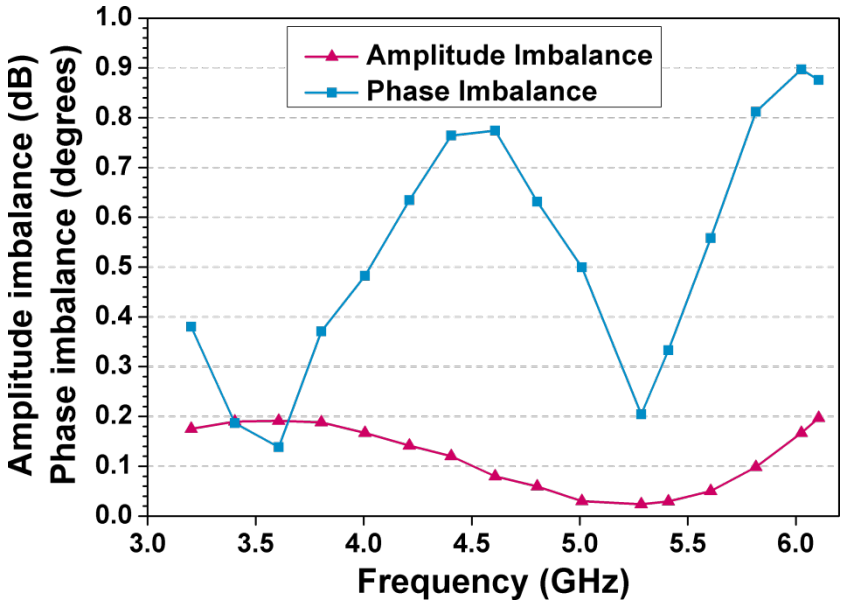

Fig. 6.13 Measured amplitude and phase balance within the 10-dB bandwidth of the filter for several tuning states across its tuning range. The measurements are taken with the package lid attached.

Table 6.1. Summary of the work demonstrated in this chapter compared to existing state-of-the-art tunable and fixed balun filters.

Ref.	f_0 (GHz)	Amplitude Imbalance	Phase Imbalance	Tunability
[118]	0.62 – 1.04	< 0.5 dB	< 5°	Tunable
[119]	1.49 – 1.55	< 0.5 dB	< 5°	Tunable
This work	**3.2 – 6.1**	**< 0.2 dB**	**< 0.9°**	**Tunable**
[117]	1.75	< 0.25 dB	< 1.1°	Fixed
[120]	12.5	< 0.35 dB	< 2°	Fixed
[116]	2.4	< 0.09 dB	< 0.25°	Fixed
This work	**5.28**	**< 0.024 dB**	**< 0.2°**	**Fixed**

6.5 Conclusion

In this chapter, we have introduced and demonstrated a new differential coupling method for evanescent-mode cavity resonators which allows high-performance tunable balun filters to be developed. To demonstrate the concept, a 3-pole tunable balun filter using high-Q evanesecent-mode cavity resonators was design and measured. The filter shows state-of-the-art performance compared to other published tunable balun filters, with less than 0.2 dB and 0.9° of amplitude and phase imbalance across its 3.5 to 6.2 GHz tuning range. Additionally, in its 5.3 GHz tuning state, the filter has state-of-the-art performance when compared to any published static or tunable balun filter, with less than 0.024 dB and 0.2° of amplitude and phase imbalance within its 10-dB bandwidth.

7. A TUNABLE BANDSTOP FILTER WITH AN ULTRA-BROAD UPPER PASSBAND

7.1 Introduction

In wideband communication systems, it is often necessary to block strong jamming signals which fall within the band of interest. One such example is the ultra-wideband (UWB) communication standard, which spans 3.1 to 10.6 GHz frequency range. Interference from WLAN systems in the 5 to 6 GHz range, as well as many other sources of interference, can severely degrade the sensitivity of an unprotected UWB receiver [121]. Another example is a receiver designed for intercepting an adversary's wireless communications without prior knowledge of the frequency of the transmission. In this case the receiver would need to be very wideband, but would suffer from the same interference problems as UWB systems. In both of these cases a tunable bandstop filter could be used to selectively reject interfering signals. However, unless the bandstop filter has a low-loss passband which extends up to the maximum frequency of the receiver, the bandstop filter itself will degrade the performance of the receiver. It can be challenging to design bandstop filters with very broad upper passbands for two main reasons. First, all practical resonators have spurious resonances which create additional stopbands at finite frequencies. Secondly, the coupling structures used to couple resonators to the filter's through-line often introduce large parasitics, which can degrade the filter's passband even at frequencies below the first spurious resonance of the resonator.

For example, the first spurious mode of a half-wave microstrip resonator is $2f_0$, where f_0 is the resonator's fundamental resonant frequency. Grounded quarter-wave resonators have spurious-free ranges up to $3f_0$, and adding capacitive loading or using structures such as stepped-impedance resonators can further increase this spurious-free range [122]. Additionally, some methods have been proposed for suppressing spurious

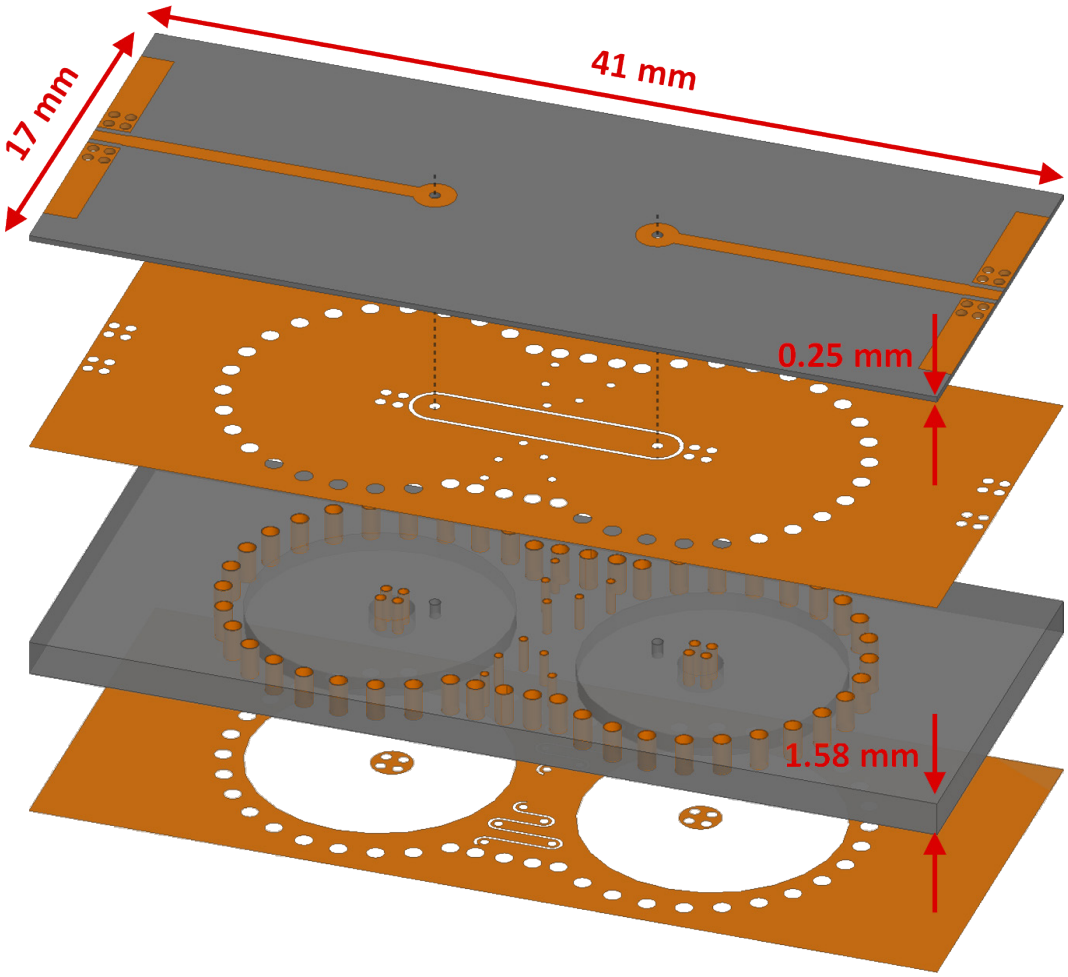

Fig. 7.1. Diagram of a two-pole bandstop filter which utilizes the proposed broadband external coupling method.

modes to enable even wider upper passbands [21]. However, tunable microstrip-based filters have limited performance in terms of quality factor and linearity, and thus are not suitable for all applications. Evanescent-mode cavity resonators [81] are an attractive alternative to varactor-tuned microstrip filters due to their wide tunability, high unloaded quality factor, and high linearity. They can also possess very large spurious-free ranges of up to 40:1. However, the upper passband of an evanescent-mode bandstop filter is typically limited by the reactances introduced by the external coupling structure [55]. This coupling is usually implemented through a coupling aperture in the resonator's ground plane, which is shared between the microstrip feeding transmission lines and the cavity resonator itself. The aperture introduces a large inductance in the ground path of

the microstrip through-line, which eventually causes high levels of reflection and limits the upper passband of the filter. A new coupling structure which mitigates this problem was introduced in [56], which routes the microstrip line through the cavity instead of coupling through an aperture. This structure avoided many of the parasitics associated with the typical coupling apertures, and enabled a 0.65 to 1.65 GHz tunable filter to have a 3-dB passband extending up to 11.1 GHz. Despite the filter's exceptional performance, the design is relatively difficult to accurately manufacture with standard printed circuit board (PCB) milling machines. This fabrication inaccuracy, along with the small but still-present parasitics associated with the coupling structure, prevent this design from being extended to higher operating frequencies. This paper introduces a new coupling structure which improves upon the design of [56] by reducing parasitics and fabrication complexity, enabling the implementation of a 3 to 6 GHz tunable bandstop filter with a 3-dB upper passband extending up to 28.5 GHz.

7.2 Broadband Coupling Structure

The proposed coupling structure is similar in concept to the one in [56], in that it consists of a section of transmission line routed through the cavity resonator instead of the more traditional method of using a coupling aperture. A diagram of the proposed coupling structure is shown in Fig. 7.2. To realize the external coupling, the microstrip transmission line which serves as the input to the filter is transferred to a coplanar waveguide (CPW) transmission line which is embedded in the ground plane of the cavity. The magnetic fields of this section of CPW line extend into the cavity and couple with its magnetic fields, allowing the desired coupling between the through-line and cavity to be realized. This structure does not have any of the resonant apertures that the traditional method does, which allows the filter to have a well-matched passband extending up to very high frequencies as long as the dimensions of the microstrip and CPW lines are chosen so that they are both have 50-Ω characteristic impedances. The proposed structure can be fabricated simply and accurately using any standard multi-layer PCB process. In contrast, the structure of [56] required copper features to be patterned at a specified depth

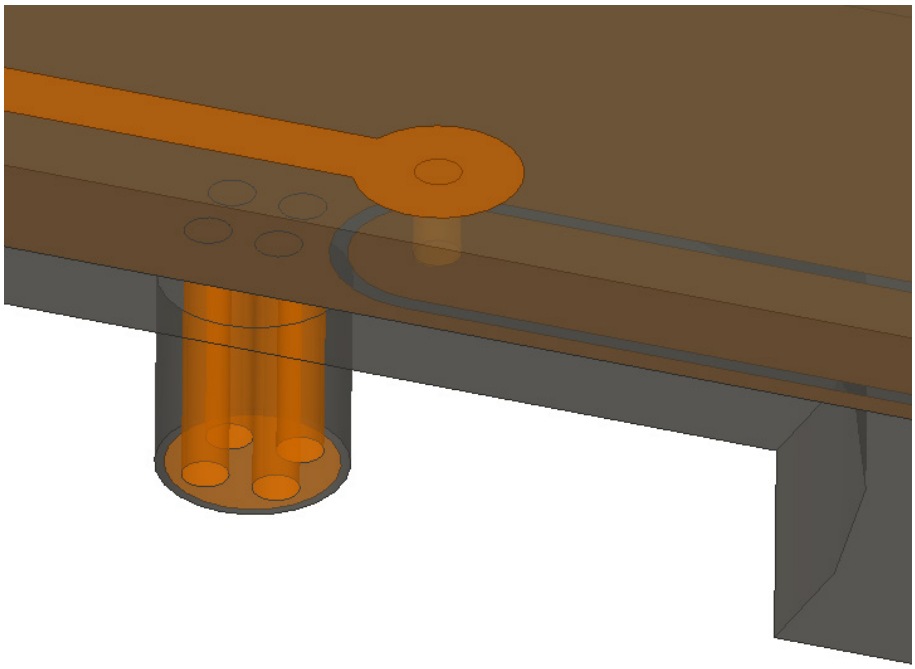

Fig. 7.2. The microstrip through-line is connected to a short section of CPW line embedded in the ground plane of the resonator.

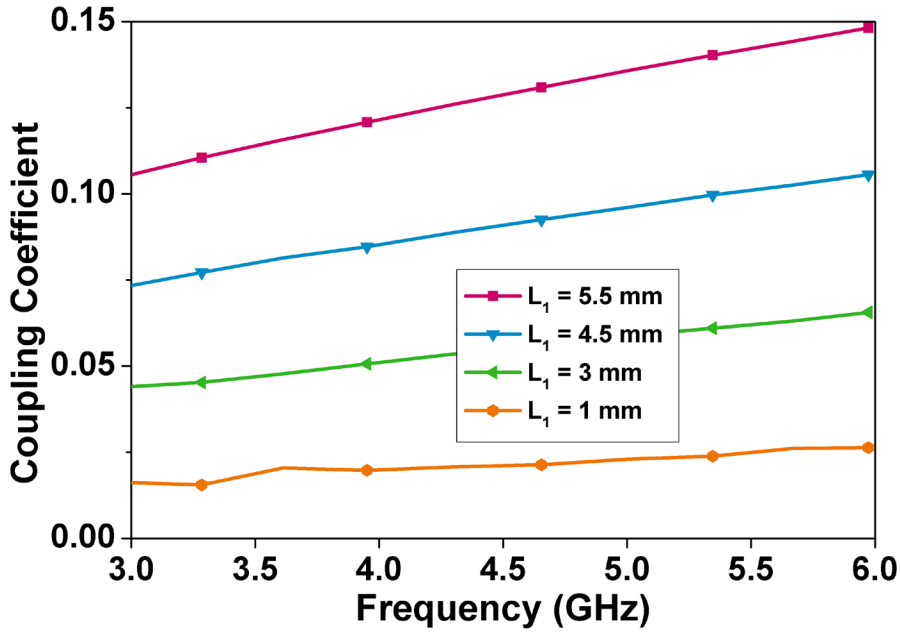

Fig. 7.3. Dependence of external coupling coefficient on the length of the CPW line.

inside of a cavity routed into the substrate, a process which is difficult to perform accurately and is not compatible with standard PCB fabrication processes.

One notable source of parasitics is the via which connects the microstrip line to the CPW line. This presents a small series inductance to the signal path, but the effect of this series inductance can be compensated by adding a small shunt capacitance. This shunt capacitance can be realized by decreasing the impedance of the transmission line near the via - in this case, by adding a circular patch to the microstrip line at the location of the via.

The strength of the coupling realized with this structure is determined by the width and length of the section of CPW line inside the cavity, as well as the distance between the CPW line and the cavity's center post. The dependence of this structure's coupling coefficient on the length of the CPW line is shown in Fig. 7.3.

7.3 Experimental Results

Using the coupling structure presented in Section II, a two-pole tunable bandstop filter was designed, as shown in Fig. 7.1. The filter was designed to have a 3 to 6 GHz tuning range, with a 1.6% 3-dB fractional bandwidth at 4.5 GHz. In order to increase the stopband rejection, the two resonators were coupled together with a small amount of interresonator coupling in order to implement an absorptive bandstop filter design [23]. The filter was fabricated using a standard PCB milling, laminating, and plating system. The signal and cavity substrates were made out Rogers 5880, and were laminated together using Rogers 2929 bondply material. Commercially-available piezoelectric disks, metalized with thin silver membranes and attached on top of the cavities using electrically-conductive silver epoxy, were used as the tuning elements. The fabricated filter is shown in Fig. 7.4.

The measured S-parameters of the filter when tuned across its 3 to 6 GHz tuning range are shown in Fig. 7.5, demonstrating that the filter can achieve more than 60 dB of stopband rejection over an octave tuning range, with a 1.25% to 2.3% 3-dB bandwidth. Passband insertion loss and return loss are both very low within the filter's tuning range, at less than 0.37 dB and better than 20 dB, respectively. The broadband frequency response of the filter is shown in Fig. 7.6. It can be seen that the filter's return loss is

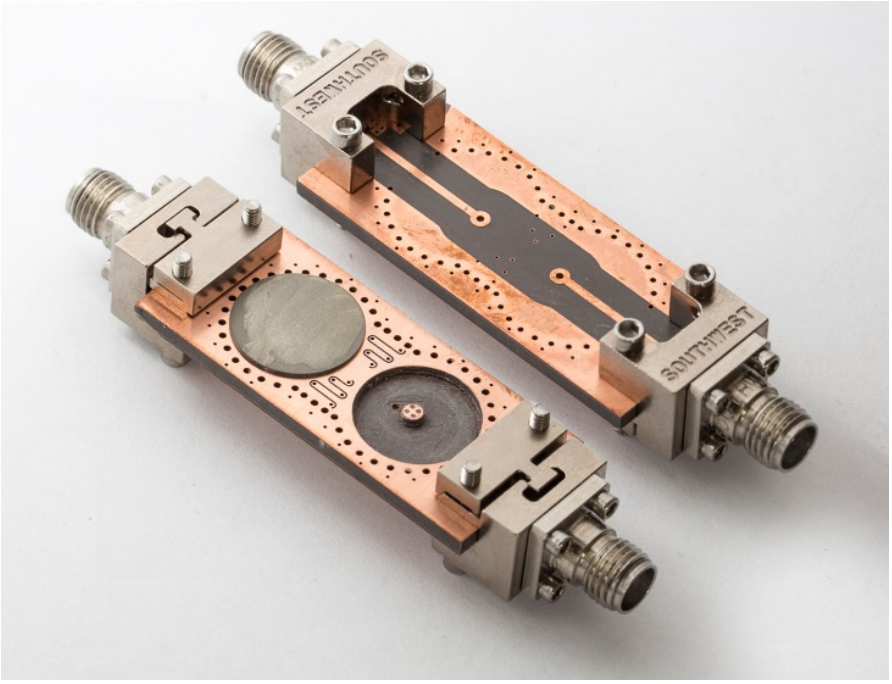

Fig. 7.4. Photograph of the fabricated filter.

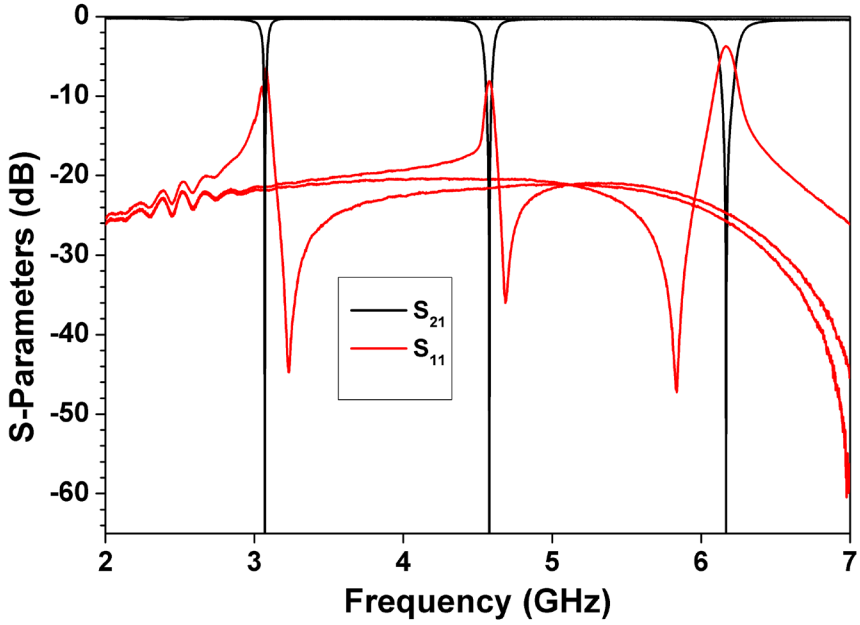

Fig. 7.5. Measured response of the filter demonstrating its octave tuning range.

better than 10 dB up to 24.2 GHz, and better than 7.5 dB up to 29.5 GHz. A close-up view of the filter's insertion loss is shown in Fig. 7.7. The insertion loss is less than 1 dB up to 17.3 GHz, less than 2 dB up to 24.9 GHz, and less than 3 dB up to 28.5 GHz. With

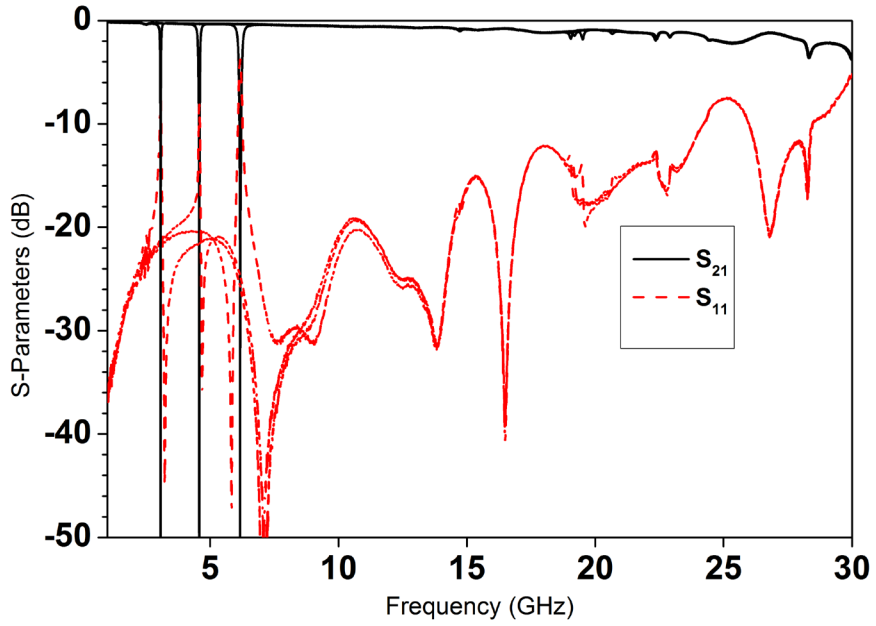

Fig. 7.6. Measured wideband response of the filter, showing its broad upper passband.

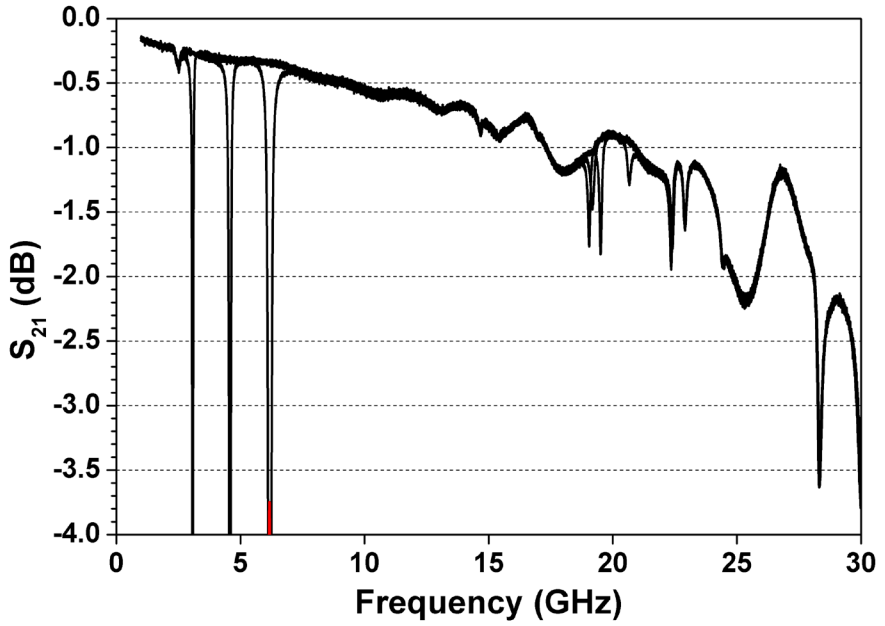

Fig. 7.7. Close-up view of the filter's measured insertion loss. The 3-dB passband extends up to 28.5 GHz.

the specific geometry of resonator used, the first spurious mode of the resonator occurs around 19 GHz. However, these spurious modes are very weakly coupled, and add less than 1 dB of insertion loss to the passband.

7.4 Conclusion

In this paper, a new broadband external coupling mechanism for evanescent-mode cavity resonators has been developed and demonstrated. This structure improves upon the design [56] by simplifying the fabrication procedure and reducing parasitics, which allows it to operate up to higher frequencies. A 3 to 6 GHz tunable bandstop filter with a 3-dB passband extending to 28.5 GHz is demonstrated. This represents a 156% improvement over the filter in [56], which had an 11.1 GHz upper passband.

8. SUMMARY AND FUTURE WORK

8.1 Dissertation Summary

This dissertation has presented a number of advances in the field of tunable microwave filters. Two main topics have been the focus of this dissertation: addressing the current limitations of tunable filters, and introducing new concepts and technologies to enable tunable filters with higher performance and versatility than previously possible.

The dissertation first addresses some of the limitations of bandstop filters utilizing lossy resonators by improving the understanding of tunable absorptive bandstop filters. This class of filter allows bandstop filters to achieve theoretically infinite stopband attenuation with finite-Q_U resonators. A unified design approach is developed for optimally designing these filters with respect to certain design criteria such as bandwidth and tuning range. A new method is also presented for addressing bandwidth variation, one of the key challenges inherent to tunable filters. This bandwidth compensation method for the first time enables tunable bandstop filters implemented with evanescent-mode cavity resonators to maintain nearly constant absolute bandwidth over wide tuning ranges, and it is shown that this method can reduce bandwidth variation over an octave tuning range by up to 95%. In order to address the fact that most tunable bandstop filters have limited upper passbands, a new broadband external coupling structure is developed. This structure is used to implement a 3 to 6 GHz tunable bandstop filter with an upper 3-dB passband which extends to 28.5 GHz.

The rest of the dissertation is devoted to introducing new enabling concepts and technologies for tunable filters. A new silicon micromachining fabrication process is developed which, in conjunction with the absorptive bandstop filter design principles developed earlier, is used to develop 22 to 43 GHz and 74 to 105 GHz tunable bandstop filters which have narrow bandwidths and provide up to 75 dB of stopband rejection. The

Ka-band filter represents state-of-the-art with respect to tuning range, bandwidth, and stopband rejection, and the W-band filter is the first-ever demonstrated tunable bandstop filter at W-band frequencies.

Lastly, a new differential coupling structure is introduced for the purpose of realizing tunable balanced-to-unbalanced (balun) filters with evanescent-mode cavity resonators. The demonstrated tunable balun filter shows state-of-the-art performance with respect to amplitude and phase imbalance at its differential output when compared to other tunable balun filters.

8.2 Contributions

The specific contributions of this dissertation are as follows.

- Chapter 2: A detailed theoretical and practical analysis of absorptive bandstop filters is presented. This chapter fills in many of the knowledge gaps associated with this type of filter by investigating and optimizing the sensitivity of the filters to process variations, the tradeoffs between selectivity and tuning range, the relative benefits and drawbacks of higher-order absorptive filters, and presents a clear design procedure for realizing such filters. Several absorptive filters realized with varactor-tuned microstrip resonators are designed and implemented to demonstrate the design process and design tradeoffs. The filters are able to achieve greater than 90 dB of stopband rejection despite using low-Q (< 100) resonators.
- Chapter 3: Using the design methodology set forth in Chapter 2 along with a newly-developed silicon micromachining fabrication process, two state-of-the-art millimeter wave tunable bandstop filters are presented: one in the K to K_a bands, and the other in the W-band. The Ka band filter is the highest-performance tunable bandstop filter in its frequency range, tuning from 22 to 43 GHz and providing up to 70 dB of stopband attenuation with a 3-dB bandwidth of less than 5%. The W-band filter, which tunes from 74 to 105 GHz, is the first-ever tunable bandstop filter demonstrated at W-band frequencies. It also provides up to 70 dB of stopband rejection, with a 1.5% 3-dB fractional bandwidth at 95 GHz. Both filters use

electrostatically-actuated MEMS diaphragm tuners, which are actuated with less than 90 V.

- Chapter 4: An intrinsically-switched dual-band filter is implemented using commercially-available RF MEMS digitally tunable capacitors. The design is highly integrated, with all power management and digital control circuitry contained on the same board as the filter. The filter consists of two 4-pole filters placed in parallel-cascade, and the intrinsic switching mechanism is realized by strongly detuning two of the resonators in the filter to be switched off. The filter has low insertion loss due to the fact that there are no switching elements in the direct signal path, and the tuning elements (RF MEMS capacitors) are very low loss and do not significantly affect the resonator quality factor when not in use.
- Chapter 5: A new type of coupling method compatible with evanescent-mode cavity resonators is presented which, for the first time, allows tunable evanescent-mode bandstop filters to have nearly constant bandwidth when tuned over wide tuning ranges. This is passive, and does not require any additional tuning elements to achieve constant bandwidth. Several filters are designed and implemented using this coupling method to demonstrate its efficacy. It is shown that when using this method to achieve constant fractional bandwidth, the 3-dB fractional bandwidth variation of an octave-tunable bandstop filter can be reduced by up to 86%. The filter demonstrated has a 1.16% to 1.3% 3-dB fractional bandwidth, whereas a filter which uses the traditional coupling method instead of the new constant-bandwidth method is shown to have a 1.25% to 2.3% fractional bandwidth. The method is also used to realize a constant absolute bandwidth filter, which has a 50.3 to 56.5 MHz 3-dB bandwidth. Compared to the uncompensated filter which has a 39 to 142 MHz bandwidth, this represents a 95% reduction in 3-dB bandwidth variation.
- Chapter 6: A novel differential coupling structure is introduced which enables the first-ever implementation of a balanced-to-unbalanced (balun) filter utilizing evanescent-mode cavity resonators to be developed. A 3-pole, 3.2 to 6.1 GHz tunable bandpass balun filter is demonstrated using this new coupling structure. In addition to the wide tunability and low insertion loss enabled by the high-Q cavity resonators, the

filter has state-of-the-art amplitude and phase imbalance at its differential output. The amplitude and phase imbalances are less than 0.2 dB and 0.9^{o} across the entire tuning range, yielding a common-mode rejection of better than 40 dB in band and 90 dB out of band for all tuning states. At 5.3 GHz, its best tuning state with respect to imbalance, the filter has less than 0.024 dB and 0.2^{o} of amplitude and phase imbalance within its 10-dB bandwidth, allowing the filter to have greater than 60 dB of common-mode rejection within its passband.. This represents state-of-the-art performance with respect to existing published static balun filters.

- Chapter 7: A broadband external coupling structure for tunable bandstop filters implemented with evanescent-mode cavity resonators is introduced. This new coupling structure enables a 3 to 6 GHz tunable bandstop filter with a 3-dB passband extending up to 28.5 GHz to be developed. This filter has the widest fractional upper passband demonstrated to date for a filter with a center frequency greater than 2 GHz.

8.3 Future Work

8.3.1 Fully-Balanced Tunable Filters

In Chapter 6 a differential coupling structure for evanescent-mode cavity resonators was introduced. The coupling structure performs a function identical to that of its single-ended counterpart, but with a differential output. The natural extension of the work in Chapter 6 is to implement this coupling structure at both the input and the output of a filter, thus creating a fully-differential filter. This concept is shown in Fig. 8.1, and an example of such a filter is shown in Fig. 8.2, which is created by implementing the differential coupling structure at the input and the output of the filter from Chapter 6. Other filtering transfer functions can also be realized with this technique. In fact, any filter which can be realized with evanescent-mode cavity resonators can be converted into either a balanced-to-unbalanced or a fully balanced filter by simply replacing the appropriate external coupling elements with the differential coupling element.

Fig. 8.3 shows the simulated performance of the filter of Fig. 8.2, as well as the performance of a 4-pole filter implemented using the same technology. In order to simulate the realistic performance of the filters, the simulations were adjusted so that the

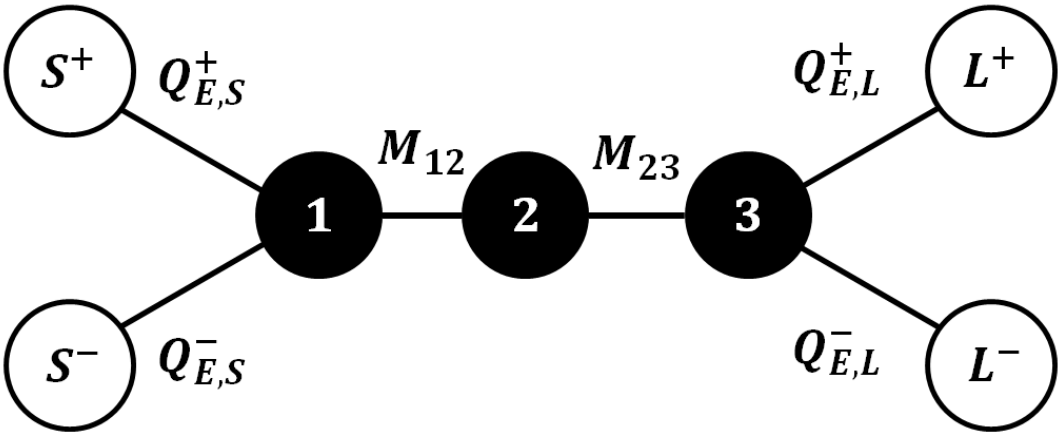

Fig. 8.1. Coupling diagram for proposed fully-differential filter. The core of the filter (that is, the resonators and all interresonator couplings) is identical to that of a single-ended filter, and differential inputs and outputs are realized by means of the coupling structure of Chapter 6.

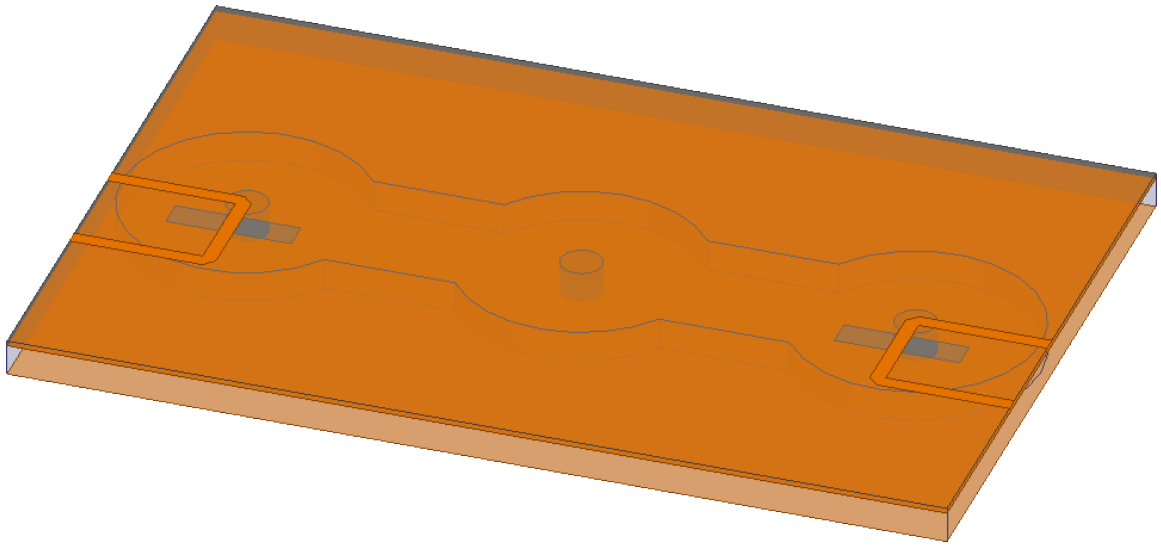

Fig. 8.2. Example of a tunable 3-pole fully-differential filter implemented by utilizing differential coupling structures at both the input and the output of the filter.

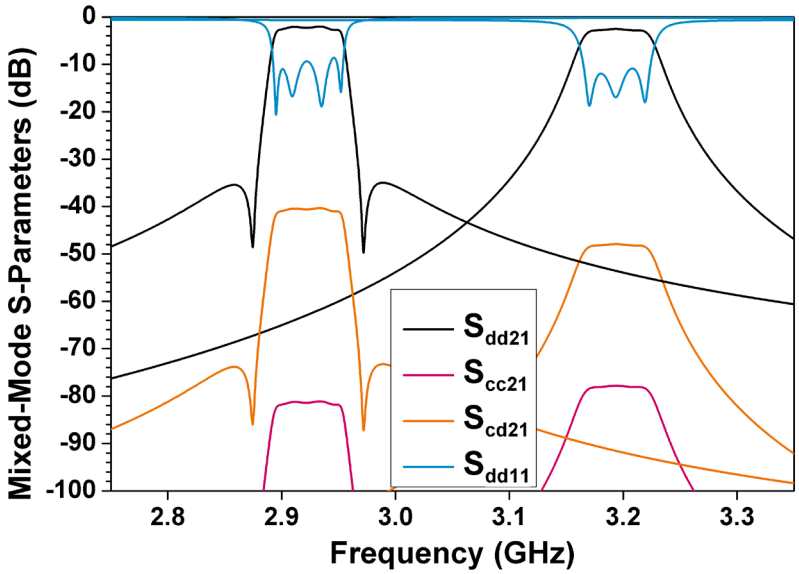

Fig. 8.3. Simulated response of the filter from Fig. 8.2

amplitude and phase balance matched the measured values from Chapter 6. It can be seen that the common-mode to differential-mode conversion (S_{cd21}) is below -40 dB - roughly the same as the measured performance of the filter in Chapter 6. The common-mode to common-mode transmission response (S_{cc21}) is even more strongly suppressed, and is less than -80 dB.

8.3.2 Future Directions for Tunable Filters

The field of tunable microwave filters has matured greatly in the past decade. Many of the practical issues related to the RF performance of tunable filters has been addressed. For example, in this dissertation we have presented ways to address the limitations of bandstop filters using finite quality factor resonators, as well as a new method for achieving constant bandwidth over wide tuning ranges. Numerous other similar examples exist in literature. Although the perfect tunable filter certainly does not exist, filters with the high performance needed for many systems exist, and are ready to be implemented into reconfigurable radio systems. Some of the primary challenges that remain are related to practically integrating these filters into systems, such packaging, reliability, manufacturability, and how to sense and control the frequency of the filter.

LIST OF REFERENCES

LIST OF REFERENCES

[1] J. H. Burgess, “Ferrite-Tunable Filter for Use in S Band,” *Proc. IRE*, vol. 44, no. 10, pp. 1460–1462, Oct. 1956.

[2] Omniyig, “YIG Filters.” [Online]. Available: http://www.omniyig.com/. [Accessed: 09-Nov-2015].

[3] “YIG Filters: the complete microwave solution.” [Online]. Available: http://www.teledynemicrowave.com/images/Brochures/Catalog_TMS%20YIG%20Filter%20Products%200507.pdf. [Accessed: 09-Nov-2015].

[4] “Technology Descriptions: YIG Tuned Filters.” [Online]. Available: http://www.microlambdawireless.com/uploads/files//pdfs/ytfdefinitions2.pdf. [Accessed: 09-Nov-2015].

[5] I. C. Hunter and J. D. Rhodes, “Electronically Tunable Microwave Bandstop Filters,” *IEEE Trans. Microw. Theory Tech.*, vol. 30, no. 9, pp. 1361–1367, Sep. 1982.

[6] I. C. Hunter and J. D. Rhodes, “Electronically Tunable Microwave Bandpass Filters,” *IEEE Trans. Microw. Theory Tech.*, vol. 30, no. 9, pp. 1354–1360, Sep. 1982.

[7] “MA46 Series Datasheet.” [Online]. Available: http://cdn.macom.com/datasheets/MA46%20Series.pdf. [Accessed: 09-Nov-2015].

[8] D. R. Jachowski, “Octave tunable lumped-element notch filter,” in *Microwave Symposium Digest (MTT), 2012 IEEE MTT-S International*, 2012, pp. 1–3.

[9] D. R. Jachowski, “Tunable lumped-element notch filter with constant bandwidth,” in *2010 IEEE International Conference on Wireless Information Technology and Systems (ICWITS)*, 2010, pp. 1–4.

[10] D. Kholodnyak, V. Turgaliev, and A. Baskakova, “A method to design lumped-element tunable bandpass filters with constant absolute bandwidth,” in *Microwave Conference (EuMC), 2014 44th European*, 2014, pp. 335–338.

[11] T.-C. Lee, J. Lee, E. J. Naglich, and D. Peroulis, “Octave tunable lumped-element notch filter with resonator-Q-independent zero reflection coefficient,” in *Microwave Symposium (IMS), 2014 IEEE MTT-S International*, 2014, pp. 1–4.

[12] Y.-C. Ou and G. M. Rebeiz, "Lumped-Element Fully Tunable Bandstop Filters for Cognitive Radio Applications," *IEEE Trans. Microw. Theory Tech.*, vol. 59, no. 10, pp. 2461–2468, Oct. 2011.

[13] J. Lee and K. Sarabandi, "An Analytic Design Method for Microstrip Tunable Filters," *IEEE Trans. Microw. Theory Tech.*, vol. 56, no. 7, pp. 1699–1706, Jul. 2008.

[14] Q. Xiang, Q. Feng, X. Huang, and D. Jia, "Electrical Tunable Microstrip LC Bandpass Filters With Constant Bandwidth," *IEEE Trans. Microw. Theory Tech.*, vol. 61, no. 3, pp. 1124–1130, Mar. 2013.

[15] M. A. El-Tanani and G. M. Rebeiz, "Corrugated Microstrip Coupled Lines for Constant Absolute Bandwidth Tunable Filters," *IEEE Trans. Microw. Theory Tech.*, vol. 58, no. 4, pp. 956–963, Apr. 2010.

[16] X. Luo, S. Sun, and R. B. Staszewski, "Tunable Bandpass Filter With Two Adjustable Transmission Poles and Compensable Coupling," *IEEE Trans. Microw. Theory Tech.*, vol. 62, no. 9, pp. 2003–2013, Sep. 2014.

[17] Y.-H. Cho and G. M. Rebeiz, "Two- and Four-Pole Tunable 0.7-1.1-GHz Bandpass-to-Bandstop Filters With Bandwidth Control," *IEEE Trans. Microw. Theory Tech.*, vol. 62, no. 3, pp. 457–463, Mar. 2014.

[18] D. R. Jachowski and A. C. Guyette, "Sub-octave-tunable microstrip notch filter," in *IEEE International Symposium on Electromagnetic Compatibility, 2009. EMC 2009*, 2009, pp. 99–102.

[19] A. C. Guyette, "Intrinsically Switched Varactor-Tuned Filters and Filter Banks," *IEEE Trans. Microw. Theory Tech.*, vol. 60, no. 4, pp. 1044–1056, Apr. 2012.

[20] A. C. Guyette, "Theory and Design of Intrinsically Switched Multiplexers With Optimum Phase Linearity," *IEEE Trans. Microw. Theory Tech.*, vol. 61, no. 9, pp. 3254–3264, Sep. 2013.

[21] A. C. Guyette, "Design of fixed- and varactor-tuned bandstop filters with spurious suppression," in *Microwave Conference (EuMC), 2010 European*, 2010, pp. 288–291.

[22] A. C. Guyette, "Varactor-tuned bandstop filters with tunable center frequency and bandwidth," in *2010 IEEE International Conference on Wireless Information Technology and Systems (ICWITS)*, 2010, pp. 1–4.

[23] D. R. Jachowski, "Compact, frequency-agile, absorptive bandstop filters," in *Microwave Symposium Digest, 2005 IEEE MTT-S International*, 2005, p. 4 pp.-pp.

[24] D. R. Jachowski and C. Rauscher, "Frequency-agile bandstop filter with tunable attenuation," in *Microwave Symposium Digest, 2009. MTT '09. IEEE MTT-S International*, 2009, pp. 649–652.

[25] A. Anand and X. Liu, "Capacitively tuned electrical coupling for reconfigurable coaxial cavity bandstop filters," in *Microwave Symposium (IMS), 2015 IEEE MTT-S International*, 2015, pp. 1–3.

[26] A. Anand, Y. Liu, and X. Liu, "Substrate-integrated octave-tunable combline bandstop filter with surface mount varactors," in *Wireless Symposium (IWS), 2014 IEEE International*, 2014, pp. 1–4.

[27] A. Anand, J. Small, M. S. Arif, M. Sinani, D. Peroulis, and X. Liu, "A novel high-Qu octave-tunable resonator with lumped tuning elements," in *Microwave Symposium Digest (IMS), 2013 IEEE MTT-S International*, 2013, pp. 1–3.

[28] A. Anand, J. Small, D. Peroulis, and X. Liu, "Theory and Design of Octave Tunable Filters With Lumped Tuning Elements," *IEEE Trans. Microw. Theory Tech.*, vol. 61, no. 12, pp. 4353–4364, Dec. 2013.

[29] A. Anand, J. Small, X. Liu, and H. H. Sigmarsson, "Tunable RF filters based on radially loaded evanescent-mode cavity resonators," in *Radio Science Meeting (USNC-URSI NRSM), 2013 US National Committee of URSI National*, 2013, pp. 1–1.

[30] V. Sekar and K. Entesari, "A Half-Mode Substrate-Integrated-Waveguide Tunable Filter Using Packaged RF MEMS Switches," *IEEE Microw. Wirel. Compon. Lett.*, vol. 22, no. 7, pp. 336–338, Jul. 2012.

[31] D. Scarbrough, C. Goldsmith, J. Papapolymerou, and Y. Li, "Miniature microwave RF MEMS tunable waveguide filter," in *Microwave Conference, 2009. EuMC 2009. European*, 2009, pp. 1860–1863.

[32] I. Reines, A. Brown, M. El-Tanani, A. Grichener, and G. Rebeiz, "1.6-2.4 GHz RF MEMS tunable 3-pole suspended combline filter," in *Microwave Symposium Digest, 2008 IEEE MTT-S International*, 2008, pp. 133–136.

[33] X. Zou, K. Chen, H. Zhang, and J. Zhang, "Design and simulation of 4-bit 10-14GHz RF MEMS tunable filter," in *4th IEEE International Conference on Nano/Micro Engineered and Molecular Systems, 2009. NEMS 2009*, 2009, pp. 21–24.

[34] C.-C. Cheng and G. M. Rebeiz, "High- 4-6-GHz Suspended Stripline RF MEMS Tunable Filter With Bandwidth Control," *IEEE Trans. Microw. Theory Tech.*, vol. 59, no. 10, pp. 2469–2476, Oct. 2011.

[35] V. Sekar, M. Armendariz, and K. Entesari, "A 1.2-1.6-GHz Substrate-Integrated-Waveguide RF MEMS Tunable Filter," *IEEE Trans. Microw. Theory Tech.*, vol. 59, no. 4, pp. 866–876, Apr. 2011.

[36] K. Entesari, K. Obeidat, A. R. Brown, and G. M. Rebeiz, "A 25-75-MHz RF MEMS Tunable Filter," *IEEE Trans. Microw. Theory Tech.*, vol. 55, no. 11, pp. 2399–2405, Nov. 2007.

[37] K.-Y. Lee and G. M. Rebeiz, "A miniature 8-16 GHz packaged tunable frequency and bandwidth RF MEMS filter," in *IEEE International Symposium on Radio-Frequency Integration Technology, 2009. RFIT 2009*, 2009, pp. 249–252.

[38] K. Entesari and G. M. Rebeiz, "A 12-18-GHz Three-Pole RF MEMS Tunable Filter," *IEEE Trans. Microw. Theory Tech.*, vol. 53, no. 8, pp. 2566–2571, Aug. 2005.

[39] M. S. Arif and D. Peroulis, "A 6 to 24 GHz continuously tunable, microfabricated, high-Q cavity resonator with electrostatic MEMS actuation," in *Microwave Symposium Digest (MTT), 2012 IEEE MTT-S International*, 2012, pp. 1–3.

[40] Z. Yang and D. Peroulis, "A 23-35 GHz MEMS Tunable All-Silicon Cavity Filter with Stability Characterization up to 140 Million Cycles," in *Microwave Symposium Digest, 2014 IEEE MTT-S International*, 2014.

[41] S. Saeedi, J. Lee, and H. Sigmarsson, "Broadband implementation of tunable, substrate-integrated, evanescent-mode, cavity bandpass filters," in *Microwave Conference (EuMC), 2014 44th European*, 2014, pp. 849–852.

[42] D. Psychogiou and D. Peroulis, "Tunable VHF Miniaturized Helical Filters," *IEEE Trans. Microw. Theory Tech.*, vol. 62, no. 2, pp. 282–289, Feb. 2014.

[43] M. Abu Khater and D. Peroulis, "Vibration mitigation for evanescent-mode cavity filters," in *Microwave Symposium (IMS), 2014 IEEE MTT-S International*, 2014, pp. 1–4.

[44] M. S. Arif and D. Peroulis, "All-Silicon Technology for High- Evanescent Mode Cavity Tunable Resonators and Filters," *J. Microelectromechanical Syst.*, vol. 23, no. 3, pp. 727–739, Jun. 2014.

[45] E. J. Naglich, A. C. Guyette, and D. Peroulis, "High-Q intrinsically-switched quasi-absorptive tunable bandstop filter with electrically-short resonators," in *Microwave Symposium (IMS), 2014 IEEE MTT-S International*, 2014, pp. 1–4.

[46] E. J. Naglich, D. Peroulis, and W. J. Chappell, “Wide spurious free range positive-to-negative inter-resonator coupling structure for reconfigurable filters,” in *Microwave Symposium Digest (IMS), 2013 IEEE MTT-S International*, 2013, pp. 1–4.

[47] E. J. Naglich, J. Lee, H. H. Sigmarsson, D. Peroulis, and W. J. Chappell, “Intersecting Parallel-Plate Waveguide Loaded Cavities for Dual-Mode and Dual-Band Filters,” *IEEE Trans. Microw. Theory Tech.*, vol. 61, no. 5, pp. 1829–1838, May 2013.

[48] K. Chen, J. Lee, W. J. Chappell, and D. Peroulis, “Co-Design of Highly Efficient Power Amplifier and High- Output Bandpass Filter,” *IEEE Trans. Microw. Theory Tech.*, vol. 61, no. 11, pp. 3940–3950, Nov. 2013.

[49] J. Small, M. S. Arif, A. Fruehling, and D. Peroulis, “A Tunable Miniaturized RF MEMS Resonator With Simultaneous High Q_U (500-735) and Fast Response Speed,” *J. Microelectromechanical Syst.*, vol. 22, no. 2, pp. 395–405, Apr. 2013.

[50] K. Chen, X. Liu, W. J. Chappell, and D. Peroulis, “Co-design of power amplifier and narrowband filter using high-Q evanescent-mode cavity resonator as the output matching network,” in *Microwave Symposium Digest (MTT), 2011 IEEE MTT-S International*, 2011, pp. 1–4.

[51] J. Lee, E. J. Naglich, H. H. Sigmarsson, D. Peroulis, and W. J. Chappell, “New Bandstop Filter Circuit Topology and Its Application to Design of a Bandstop-to-Bandpass Switchable Filter,” *IEEE Trans. Microw. Theory Tech.*, vol. 61, no. 3, pp. 1114–1123, Mar. 2013.

[52] E. J. Naglich, D. Peroulis, and W. J. Chappell, “Low-Order Filter Response Enhancement in Reconfigurable Resonator Arrays,” *IEEE Trans. Microw. Theory Tech.*, vol. 61, no. 12, pp. 4387–4395, Dec. 2013.

[53] T. Snow, J. Lee, and W. J. Chappell, “Tunable high quality-factor absorptive bandstop filter design,” in *Microwave Symposium Digest (MTT), 2012 IEEE MTT-S International*, 2012, pp. 1–3.

[54] J. Small, W. Irshad, and D. Peroulis, “A fast high-Q X-band RF-MEMS reconfigurable evanescent-mode cavity resonator,” in *Microwave Symposium Digest (MTT), 2012 IEEE MTT-S International*, 2012, pp. 1–3.

[55] E. J. Naglich, J. Lee, D. Peroulis, and W. J. Chappell, “Extended Passband Bandstop Filter Cascade With Continuous 0.85-6.6-GHz Coverage,” *IEEE Trans. Microw. Theory Tech.*, vol. 60, no. 1, pp. 21–30, Jan. 2012.

[56] E. J. Naglich, J. Lee, and D. Peroulis, “Tunable bandstop filter with a 17-to-1 upper passband,” in *Microwave Symposium Digest (MTT), 2012 IEEE MTT-S International*, 2012, pp. 1–3.

[57] H. H. Sigmarsson, E. Naglich, J. Lee, D. Peroulis, and W. Chappell, “Tunable bandpass and bandstop filter cascade for dynamic pole allocation,” in *2012 IEEE Antennas and Propagation Society International Symposium (APSURSI)*, 2012, pp. 1–2.

[58] X. Liu, E. Naglich, and D. Peroulis, “Non-linear effects in MEMS tunable bandstop filters,” in *Microwave Symposium Digest (MTT), 2012 IEEE MTT-S International*, 2012, pp. 1–3.

[59] K. Chen, H. H. Sigmarsson, and D. Peroulis, “Power handling of high-Q evanescent-mode tunable filter with integrated piezoelectric actuators,” in *Microwave Symposium Digest (MTT), 2012 IEEE MTT-S International*, 2012, pp. 1–3.

[60] E. J. Naglich, J. Lee, D. Peroulis, and W. J. Chappell, “Switchless Tunable Bandstop-to-All-Pass Reconfigurable Filter,” *IEEE Trans. Microw. Theory Tech.*, vol. 60, no. 5, pp. 1258–1265, May 2012.

[61] X. Liu, L. P. B. Katehi, W. J. Chappell, and D. Peroulis, “Power Handling of Electrostatic MEMS Evanescent-Mode (EVA) Tunable Bandpass Filters,” *IEEE Trans. Microw. Theory Tech.*, vol. 60, no. 2, pp. 270–283, Feb. 2012.

[62] E. J. Naglich, J. Lee, D. Peroulis, and W. J. Chappell, “High-Q tunable bandstop filters with adaptable bandwidth and pole allocation,” in *Microwave Symposium Digest (MTT), 2011 IEEE MTT-S International*, 2011, pp. 1–4.

[63] J. Lee, E. J. Naglich, H. H. Sigmarsson, D. Peroulis, and W. J. Chappell, “Frequency-agile field-programmable filter array (FPFA) with multiple functionalities,” in *Microwave Symposium Digest (MTT), 2011 IEEE MTT-S International*, 2011, pp. 1–1.

[64] X. Liu, K. Chen, L. P. B. Katehi, W. J. Chappell, and D. Peroulis, “System-level characterization of bias noise effects on electrostatic RF MEMS tunable filters,” in *2011 IEEE 24th International Conference on Micro Electro Mechanical Systems (MEMS)*, 2011, pp. 797–800.

[65] X. Liu, J. Small, D. Berdy, L. P. B. Katehi, W. J. Chappell, and D. Peroulis, “Impact of Mechanical Vibration on the Performance of RF MEMS Evanescent-Mode Tunable Resonators,” *IEEE Microw. Wirel. Compon. Lett.*, vol. 21, no. 8, pp. 406–408, Aug. 2011.

[66] M. S. Arif, W. Irshad, X. Liu, W. J. Chappell, and D. Peroulis, “A high-Q magnetostatically-tunable all-silicon evanescent cavity resonator,” in *Microwave Symposium Digest (MTT), 2011 IEEE MTT-S International*, 2011, pp. 1–4.

[67] J. Lee, E. J. Naglich, H. H. Sigmarsson, D. Peroulis, and W. J. Chappell, "Tunable Inter-Resonator Coupling Structure With Positive and Negative Values and Its Application to the Field-Programmable Filter Array (FPFA)," *IEEE Trans. Microw. Theory Tech.*, vol. 59, no. 12, pp. 3389–3400, Dec. 2011.

[68] W. Irshad and D. Peroulis, "A 12-18 GHz electrostatically tunable liquid metal RF MEMS resonator with quality factor of 1400-1840," in *Microwave Symposium Digest (MTT), 2011 IEEE MTT-S International*, 2011, pp. 1–4.

[69] E. E. Hoppenjans and W. J. Chappell, "A vertically integrated tunable UHF filter," in *Microwave Symposium Digest (MTT), 2010 IEEE MTT-S International*, 2010, pp. 1380–1383.

[70] H. H. Sigmarsson, J. Lee, D. Peroulis, and W. J. Chappell, "Reconfigurable-order bandpass filter for frequency agile systems," in *Microwave Symposium Digest (MTT), 2010 IEEE MTT-S International*, 2010, pp. 1756–1759.

[71] S. Moon, H. H. Sigmarsson, H. Joshi, and W. J. Chappell, "Substrate Integrated Evanescent-Mode Cavity Filter With a 3.5 to 1 Tuning Ratio," *IEEE Microw. Wirel. Compon. Lett.*, vol. 20, no. 8, pp. 450–452, Aug. 2010.

[72] X. Liu, L. P. B. Katehi, W. J. Chappell, and D. Peroulis, "High- Tunable Microwave Cavity Resonators and Filters Using SOI-Based RF MEMS Tuners," *J. Microelectromechanical Syst.*, vol. 19, no. 4, pp. 774–784, Aug. 2010.

[73] E. J. Naglich, J. Lee, D. Peroulis, and W. J. Chappell, "Tunable, substrate integrated, high Q filter cascade for high isolation," in *Microwave Symposium Digest (MTT), 2010 IEEE MTT-S International*, 2010, pp. 1468–1471.

[74] J. Lee, E. J. Naglich, and W. J. Chappell, "Frequency Response Control in Frequency-Tunable Bandstop Filters," *IEEE Microw. Wirel. Compon. Lett.*, vol. 20, no. 12, pp. 669–671, Dec. 2010.

[75] E. J. Naglich, J. Lee, D. Peroulis, and W. J. Chappell, "A Tunable Bandpass-to-Bandstop Reconfigurable Filter With Independent Bandwidths and Tunable Response Shape," *IEEE Trans. Microw. Theory Tech.*, vol. 58, no. 12, pp. 3770–3779, Dec. 2010.

[76] H. Joshi, H. H. Sigmarsson, S. Moon, D. Peroulis, and W. J. Chappell, "Tunable high Q narrow-band triplexer," in *Microwave Symposium Digest, 2009. MTT '09. IEEE MTT-S International*, 2009, pp. 1477–1480.

[77] H. Joshi, H. H. Sigmarsson, S. Moon, D. Peroulis, and W. J. Chappell, "High- Fully Reconfigurable Tunable Bandpass Filters," *IEEE Trans. Microw. Theory Tech.*, vol. 57, no. 12, pp. 3525–3533, Dec. 2009.

[78] H. H. Sigmarsson, A. Christianson, H. Joshi, S. Moon, D. Peroulis, and W. J. Chappell, “In-situ control of tunable evanescent-mode cavity filters using differential mode monitoring,” in *Microwave Symposium Digest, 2009. MTT ’09. IEEE MTT-S International*, 2009, pp. 633–636.

[79] X. Liu, L. P. B. Katehi, W. J. Chappell, and D. Peroulis, “Power handling capability of High-Q evanescent-mode RF MEMS resonators with flexible diaphragm,” in *Microwave Conference, 2009. APMC 2009. Asia Pacific*, 2009, pp. 194–197.

[80] X. Liu, L. P. B. Katehi, W. J. Chappell, and D. Peroulis, “A 3.4-6.2 GHz Continuously tunable electrostatic MEMS resonator with quality factor of 460 #x2013;530,” in *Microwave Symposium Digest, 2009. MTT ’09. IEEE MTT-S International*, 2009, pp. 1149–1152.

[81] H. Joshi, H. H. Sigmarsson, D. Peroulis, and W. J. Chappell, “Highly Loaded Evanescent Cavities for Widely Tunable High-Q Filters,” in *Microwave Symposium, 2007. IEEE/MTT-S International*, 2007, pp. 2133–2136.

[82] M. . Hickle, M. Sinani, and D. Peroulis, “Tunable High-Isolation W-Band Bandstop Filters,” in *Microwave Symposium (IMS), 2015 IEEE MTT-S International*, 2015, pp. 1–3.

[83] E. J. Naglich, M. Sinani, S. Moon, and D. Peroulis, “High-Q MEMS-tunable W-band bandstop resonators,” in *Microwave Symposium (IMS), 2014 IEEE MTT-S International*, 2014, pp. 1–3.

[84] I. F. Akyildiz, W.-Y. Lee, M. C. Vuran, and S. Mohanty, “A survey on spectrum management in cognitive radio networks,” *IEEE Commun. Mag.*, vol. 46, no. 4, pp. 40–48, Apr. 2008.

[85] Y.-H. Cho and G. M. Rebeiz, “0.7-1.0-GHz Reconfigurable Bandpass-to-Bandstop Filter With Selectable 2- and 4-Pole Responses,” *IEEE Trans. Microw. Theory Tech.*, vol. 62, no. 11, pp. 2626–2632, Nov. 2014.

[86] I. Reines, S.-J. Park, and G. M. Rebeiz, “Compact Low-Loss Tunable -Band Bandstop Filter With Miniature RF-MEMS Switches,” *IEEE Trans. Microw. Theory Tech.*, vol. 58, no. 7, pp. 1887–1895, Jul. 2010.

[87] W. D. Yan and R. R. Mansour, “Compact Tunable Bandstop Filter Integrated with Large Deflected Actuators,” in *Microwave Symposium, 2007. IEEE/MTT-S International*, 2007, pp. 1611–1614.

[88] D. R. Jachowski, “Narrow-band absorptive bandstop filter with multiple signal paths,” U.S. Patent 7323955, 29-Jan-2008.

[89] A. C. Guyette, I. C. Hunter, R. D. Pollard, and D. R. Jachowski, "Perfectly-matched bandstop filters using lossy resonators," in *Microwave Symposium Digest, 2005 IEEE MTT-S International*, 2005, p. 4 pp.-pp.

[90] M. D. Hickle, M. D. Sinanis, and D. Peroulis, "Design and implementation of an intrinsically-switched 22-43 GHz tunable bandstop filter," in *2016 IEEE 17th Annual Wireless and Microwave Technology Conference (WAMICON)*, 2016, pp. 1–3.

[91] George Matthaei, Leo Young, and E. M. Jones, *Microwave Filters, Impedance-Matching Networks, and Coupling Structures*. Norwoor, MA: Artech House, 1980.

[92] Jia-Sheng Hong, *Microstrip Filters for RF/Microwave Applications*, 2nd ed. John Wiley & Sons, Inc., 2011.

[93] D. M. Pozar, *Microwave Engineering*, 3rd Edition. John Wiley & Sons, Inc.

[94] A. C. Guyette and E. J. Naglich, "Short-Through-Line Bandstop Filters Using Dual-Coupled Resonators," *IEEE Trans. Microw. Theory Tech.*, vol. 64, no. 2, pp. 459–466, Feb. 2016.

[95] J.-S. Hong and M. J. Lancaster, "Cross-coupled microstrip hairpin-resonator filters," *IEEE Trans. Microw. Theory Tech.*, vol. 46, no. 1, pp. 118–122, Jan. 1998.

[96] D. R. Jachowski, "Passive enhancement of resonator Q in microwave notch filters," in *Microwave Symposium Digest, 2004 IEEE MTT-S International*, 2004, vol. 3, p. 1315–1318 Vol.3.

[97] H. Joshi, H. H. Sigmarsson, S. Moon, D. Peroulis, and W. J. Chappell, "High Q narrow-band tunable filters with controllable bandwidth," in *Microwave Symposium Digest, 2009. MTT '09. IEEE MTT-S International*, 2009, pp. 629–632.

[98] A. Khanna and Y. Garault, "Determination of Loaded, Unloaded, and External Quality Factors of a Dielectric Resonator Coupled to a Microstrip Line," *IEEE Trans. Microw. Theory Tech.*, vol. 31, no. 3, pp. 261–264, Mar. 1983.

[99] P. Pal, M. A. Gosálvez, and K. Sato, "Etched profile control in anisotropic etching of silicon by TMAH+Triton," *J. Micromechanics Microengineering*, vol. 22, no. 6, p. 65013, Jun. 2012.

[100] R. M. Young *et al.*, "Low-loss bandpass RF filter using MEMS capacitance switches to achieve a one-octave tuning range and independently variable bandwidth," in *Microwave Symposium Digest, 2003 IEEE MTT-S International*, 2003, vol. 3, pp. 1781–1784 vol.3.

[101] K. Ma, Q. Sun, F. Cheng, and R. M. Jayasuriya, "A 11-20GHz Switched Filter Bank for Software Defined Radio System," in *IEEE MTT-S International Microwave Workshop Series on Art of Miniaturizing RF and Microwave Passive Components, 2008. IMWS 2008*, 2008, pp. 75–78.

[102] S. F. Chao, C. H. Wu, Z. M. Tsai, H. Wang, and C. H. Chen, "Electronically Switchable Bandpass Filters Using Loaded Stepped-Impedance Resonators," *IEEE Trans. Microw. Theory Tech.*, vol. 54, no. 12, pp. 4193–4201, Dec. 2006.

[103] E. J. Naglich, J. Lee, D. Peroulis, and W. J. Chappell, "Bandpass-Bandstop Filter Cascade Performance Over Wide Frequency Tuning Ranges," *IEEE Trans. Microw. Theory Tech.*, vol. 58, no. 12, pp. 3945–3953, Dec. 2010.

[104] T.-C. Lee, J. Lee, and D. Peroulis, "Dynamic Bandpass Filter Shape and Interference Cancellation Control Utilizing Bandpass-Bandstop Filter Cascade," *IEEE Trans. Microw. Theory Tech.*, vol. 63, no. 8, pp. 2526–2539, Aug. 2015.

[105] K. W. Wong, R. R. Mansour, and G. Weale, "Compact tunable bandstop filter with wideband balun using IPD technology for frequency agile applications," in *2015 IEEE MTT-S International Microwave Symposium*, 2015, pp. 1–3.

[106] X.-Y. Zhang, C.-H. Chan, Q. Xue, and B.-J. Hu, "RF Tunable Bandstop Filters With Constant Bandwidth Based on a Doublet Configuration," *IEEE Trans. Ind. Electron.*, vol. 59, no. 2, pp. 1257–1265, 2012.

[107] A. C. Guyette, "Varactor-tuned bandstop filters with tunable center frequency and bandwidth," in *2010 IEEE International Conference on Wireless Information Technology and Systems (ICWITS)*, 2010, pp. 1–4.

[108] M. Hickle and D. Peroulis, "Octave-Tunable Constant Absolute Bandwidth Bandstop Filter Utilizing a Novel Passively-Compensated Coupling Method," in *Microwave Symposium (IMS), 2016 IEEE MTT-S International*, 2016, pp. 1–3.

[109] M. Hickle, M. Sinanis, and D. Peroulis, "Design and Implementation of an Intrinsically-Switched 22-43 GHz Tunable Bandstop Filter," in *Wireless and Microwave Technology Conference (WAMICON), 2016 IEEE 17th Annual*, 2016, pp. 1–4.

[110] D. Peroulis, E. Naglich, M. Sinani, and M. Hickle, "Tuned to Resonance: Transfer-Function-Adaptive Filters in Evanescent-Mode Cavity-Resonator Technology," *IEEE Microw. Mag.*, vol. 15, no. 5, pp. 55–69, Jul. 2014.

[111] X. P. Chen and K. Wu, "Substrate Integrated Waveguide Cross-Coupled Filter With Negative Coupling Structure," *IEEE Trans. Microw. Theory Tech.*, vol. 56, no. 1, pp. 142–149, Jan. 2008.

[112] L. K. Yeung and K.-L. Wu, "An LTCC balanced-to-unbalanced extracted-pole bandpass filter with complex load," *IEEE Trans. Microw. Theory Tech.*, vol. 54, no. 4, pp. 1512–1518, Jun. 2006.

[113] L. K. Yeung and K. L. Wu, "A Dual-Band Coupled-Line Balun Filter," *IEEE Trans. Microw. Theory Tech.*, vol. 55, no. 11, pp. 2406–2411, Nov. 2007.

[114] K. T. Chen and S. J. Chung, "A Novel Compact Balanced-to-Unbalanced Low-Temperature Co-Fired Ceramic Bandpass Filter With Three Coupled Lines Configuration," *IEEE Trans. Microw. Theory Tech.*, vol. 56, no. 7, pp. 1714–1720, Jul. 2008.

[115] L. S. Wu, Y. X. Guo, J. F. Mao, and W. Y. Yin, "Design of a Substrate Integrated Waveguide Balun Filter Based on Three-Port Coupled-Resonator Circuit Model," *IEEE Microw. Wirel. Compon. Lett.*, vol. 21, no. 5, pp. 252–254, May 2011.

[116] Y. H. Ye, Y. F. Zheng, S. C. Huang, and K. S. Chin, "Design of balun bandpass filter using doubly loaded output structure," in *2016 IEEE International Workshop on Electromagnetics: Applications and Student Innovation Competition (iWEM)*, 2016, pp. 1–3.

[117] J. X. Chen, Y. Zhan, W. Qin, and Z. H. Bao, "Design of High-Performance Filtering Balun Based on $TE01_{\delta}$;-Mode Dielectric Resonator," *IEEE Trans. Ind. Electron.*, vol. PP, no. 99, pp. 1–1, 2016.

[118] L. H. Zhou, H. Tang, J. X. Chen, and Z. H. Bao, "Tunable filtering balun with enhanced stopband rejection," *Electron. Lett.*, vol. 48, no. 14, pp. 845–847, Jul. 2012.

[119] Y. Peng, T. Wang, Y. M. Huang, W. Jiang, and G. Wang, "Electrically tunable bandpass filtering balun on engineered substrate embedded with patterned Permalloy thin film," in *2016 IEEE MTT-S International Microwave Symposium (IMS)*, 2016, pp. 1–3.

[120] J. N. Hui, W. J. Feng, and W. Q. Che, "Balun bandpass filter based on multilayer substrate integrated waveguide power divider," *Electron. Lett.*, vol. 48, no. 10, pp. 571–573, May 2012.

[121] H. Shaman and J. S. Hong, "Ultra-Wideband (UWB) Bandpass Filter With Embedded Band Notch Structures," *IEEE Microw. Wirel. Compon. Lett.*, vol. 17, no. 3, pp. 193–195, Mar. 2007.

[122] W. M. Fathelbab, "Two Novel Classes of Band-Reject Filters Realizing Broad Upper Pass Bandwidth, Synthesis and Design," *IEEE Trans. Microw. Theory Tech.*, vol. 59, no. 2, pp. 250–259, Feb. 2011.

[123] C. K. Mok, D. W. Stopp, and G. Craven, “Susceptance-loaded evanescent-mode waveguide filters,” *Proc. Inst. Electr. Eng.*, vol. 119, no. 4, pp. 416–420, Apr. 1972.

[124] D. Bharadia, E. McMilin, and S. Katti, “Full Duplex Radios,” in *Proceedings of the ACM SIGCOMM 2013 Conference on SIGCOMM*, New York, NY, USA, 2013, pp. 375–386.

[125] S. Tanaka, N. Shimomura, and K. Ohtake, “Active circulators amp: The realization of circulators using transistors,” *Proc. IEEE*, vol. 53, no. 3, pp. 260–267, Mar. 1965.

[126] C. Galland, R. Ding, N. C. Harris, T. Baehr-Jones, and M. Hochberg, “Broadband on-chip optical non-reciprocity using phase modulators,” *Opt. Express*, vol. 21, no. 12, p. 14500, Jun. 2013.

[127] C. R. Doerr, L. Chen, and D. Vermeulen, “Silicon photonics broadband modulation-based isolator,” *Opt. Express*, vol. 22, no. 4, p. 4493, Feb. 2014.

[128] I. K. Hwang, S. H. Yun, and B. Y. Kim, “Novel all-fiber-optic nonreciprocal modulator,” in *, Conference on Optical Fiber Communication. OFC 97*, 1997, pp. 253–254.

[129] S. Qin and Y. Ethan Wang, “Broadband nonmagnetic non-reciprocity in time-varying transmission lines (TVTLs),” in *Radio Science Meeting (Joint with AP-S Symposium), 2015 USNC-URSI*, 2015, pp. 173–173.

[130] Y. E. Wang, “Time-varying transmission lines (TVTL) - A new pathway to non-reciprocal and intelligent RF front-ends,” in *2014 IEEE Radio and Wireless Symposium (RWS)*, 2014, pp. 148–150.

[131] Y. E. Wang, “Non-reciprocity with time-varying transmission lines (TVTLs),” in *2012 IEEE International Conference on Wireless Information Technology and Systems (ICWITS)*, 2012, pp. 1–4.

[132] N. A. Estep, D. L. Sounas, J. Soric, and A. Alù, “Magnetic-free non-reciprocity and isolation based on parametrically modulated coupled-resonator loops,” *Nat. Phys.*, vol. 10, no. 12, pp. 923–927, Dec. 2014.

[133] N. A. Estep, D. L. Sounas, and A. Alù, “Magnetless Microwave Circulators Based on Spatiotemporally Modulated Rings of Coupled Resonators,” *IEEE Trans. Microw. Theory Tech.*, vol. 64, no. 2, pp. 502–518, Feb. 2016.

APPENDICES

A. CALCULATION OF COUPLING COEFFICIENTS

A.1 Calculating External Coupling

The methods for calculating the external coupling coefficients for bandpass filters are well documented, and can be found in references such as [92]. However, these methods do not work for calculating the external coupling coefficients for bandstop-configured resonators. One method for calculating external coupling has been described in [91], but it is somewhat cumbersome to use. In this section we will develop an alternative method for calculating the external coupling coefficient of bandstop-configured resonators.

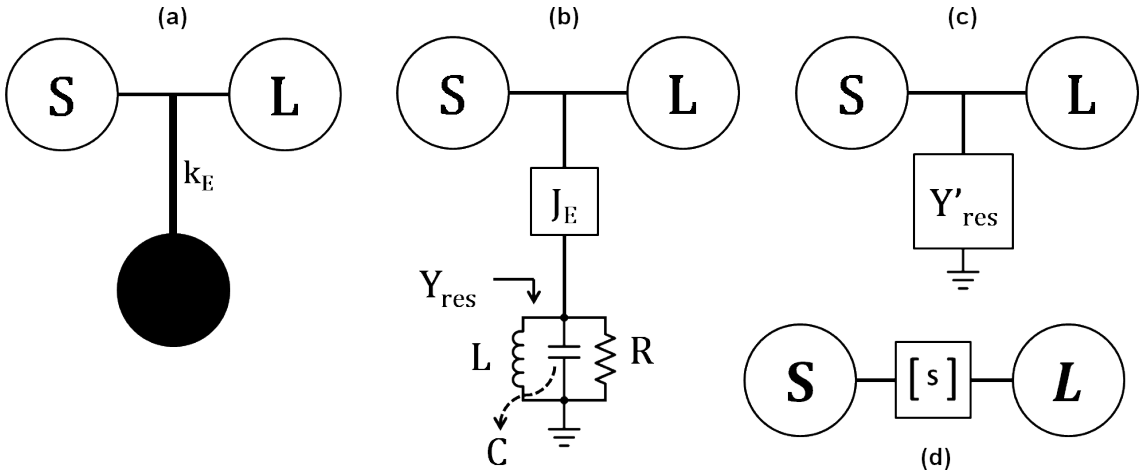

Fig A.1. (a) Coupling diagram of a single bandstop-configured resonator coupled to a source-to-load through-line. (b) Circuit representation of (a). (c) Reduced circuit of (b), with admittance inverter and resonator admittance replaced by inverted admittance. (d) Conversion of (c) to an equivalent S-parameter matrix.

A diagram of a single bandstop-configured resonator (that is, coupled to a source-to-load through-line with a coupling value of k_E) is shown in Fig A.1(a). Fig A.1(b) shows the equivalent circuit of this configuration, consisting of a parallel-RLC resonator

connected to the through-line with admittance inverter with characteristic admittance J_E. The expressions in Fig A.1(b) are defined in equations (A.1)-. Since an admittance inverter of value J transforms an admittance Y into J^2/Y, the circuit can be further reduced as shown in Fig A.1(c), with Y'_{res} defined in equation (A.6).

$$Y_{res} = \frac{1}{Z_R}\left(\frac{1}{Q_U} + j\left(\frac{\omega}{\omega_0} - \frac{\omega_0}{\omega}\right)\right) \tag{A.1}$$

$$J_E = k_E/\sqrt{Z_0 Z_R} \tag{A.2}$$

$$Z_R = \sqrt{L/C} \tag{A.3}$$

$$\omega_0 = 1/\sqrt{LC} \tag{A.4}$$

$$Q_U = \frac{R}{\omega_0 L} = \omega_0 RC \tag{A.5}$$

$$Y'_{res} = \frac{J_E^2}{Y_{Res}} \tag{A.6}$$

The S-Parameters of a single shunt admittance can easily be calculated, which yields a transmission coefficient of

$$S_{21} = \frac{2}{2 + \dfrac{k_E^2}{\dfrac{1}{Q_U} + j\left(\dfrac{\omega}{\omega_0} - \dfrac{\omega_0}{\omega}\right)}} \tag{A.7}$$

Since ω_0 can be readily identified from simulation, S_{21} depends on only two unknown variables: k_E and Q_U. The values of k_E and Q_U can be determined by recording the value of S_{21} at two values of ω.

If we designate the value of S_{21} at $\omega = \omega_0$ to be L_0, that is

$$S_{21}|_{\omega=\omega_0} = \frac{2}{2 + k_E^2 Q_U} = L_0, \tag{A.8}$$

then we can solve for k_E:

$$k_E = \sqrt{\frac{2(1 - L_0)}{L_0 Q_U}} \tag{A.9}$$

Substituting equation (A.9) into (A.7) eliminates the unknown variable k_E from the equation, and allows us to form a new expression for the magnitude of S_{21} from which Q_U can easily be extracted:

$$|S_{21}| = \sqrt{\frac{L_0^2[\omega^2\omega_0^2 + Q_U^2(\omega^2 - \omega_0^2)^2]}{\omega^2\omega_0^2 + L_0^2 Q_U^2(\omega^2 - \omega_0^2)^2}} \tag{A.10}$$

If the magnitude of S_{21} is L_A at a frequency $\omega_1 \neq \omega_0$, then rearranging equation (A.10) and solving for Q_U yields

$$Q_U = \frac{f_0 f_1}{\left|{f_0}^2 - {f_1}^2\right|} \sqrt{\frac{\frac{L_A^2}{L_0^2} - 1}{1 - L_A^2}} \tag{A.11}$$

Equation (A.11) can now be used to calculate Q_U using the measured or simulated values of S_{21} at f_0 and another frequency $f_1 \neq f_0$. After Q_U has thus been calculated, the external coupling k_E can be calculated using equation (A.9). It is important to use the magnitudes of L_0 and L_A, and not their values in decibels. Fig A.2 illustrates the measurements which are required to calculate Q_U and k_E using the method just described.

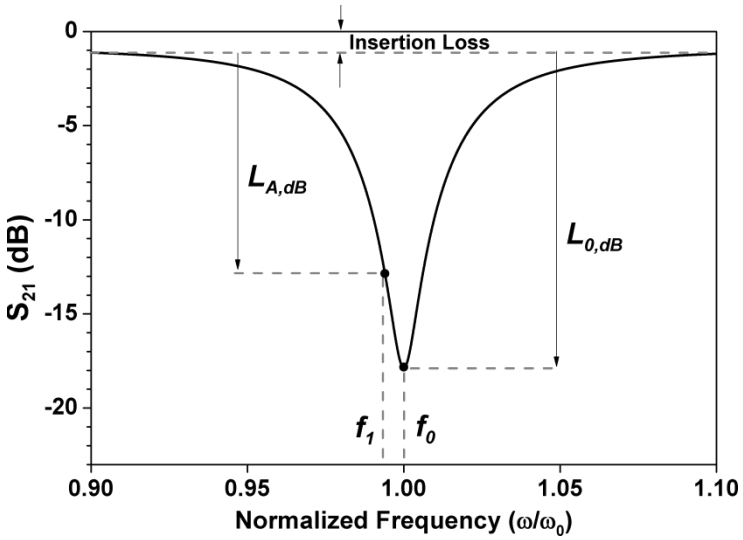

Fig A.2. Illustration of which frequencies and attenuation levels should be used when using the proposed method to calculate Q_U and k_E.

It should be noted that this method does not take into account non-ideal effects such as passband insertion loss and asymmetry of the transfer function to due mismatch in the passband. Insertion loss can be approximately taken into account by subtracting the passband insertion loss from the measured attenuation levels L_0 and L_A, as shown in Fig A.2. If there is a high level of reflection in the passband, the accuracy of this method can

be improved by calculating Q_U and k_E more than once and then averaging, using frequencies for f_1 both above and below f_0.

A.2 Polarity of External Coupling Structures

It is often necessary to know the relative polarity of the external coupling elements used to connect resonators to the source or load, particularly in bandstop filters. For example, in Chapter 2 it is shown that when designing two-pole absorptive bandstop filters, the relative signs of all couplings and transmission lines must be chosen such that the sign of the quantity $k_{E1}k_{E2}k_{12}\sin\theta$ is negative. Thus the relative signs of the two external coupling elements $k_{E1,2}$ must be known.

For a filter realized with a given resonator technology, all of the resonators generally use the same external coupling structure. This could be edge-coupled microstrip lines, coupling apertures in a ground plane, direct-tap coupling, or any number of other coupling methods. One would expect that for a given filter, all resonators using the same coupling structure would have the same relative polarity, but somewhat surprisingly this is not always the case.

Consider the filter of Fig A.3, which consists of two evanescent-mode cavity resonators coupled to a source-to-load microstrip transmission line by coupling apertures in the ground plane which is shared between the resonators and the microstrip line. Each of the resonators is excited individually, while shorting out the other resonator and deembeding the reference plane of the excitation up to the middle of the coupling aperture. It can be seen that the electric and magnetic fields in two resonators have opposite polarities, which indicates that the two external coupling elements have opposite sign. This is because the coupling apertures rely on magnetic field coupling, which causes the magnetic field of the cavity to align with the magnetic field of the microstrip line. Because the magnetic field of the cavity has opposite direction on either side of the post due to its circular pattern, the polarity of coupling realized by a given coupling aperture depends on which side of the cavity the aperture is located.

In the configuration of Fig A.3, the two coupling apertures are located on opposite sides of their respective cavities. For the left cavity, the transmission line crosses over the

coupling aperture from the inside of the cavity to the outside, whereas on the right cavity, the transmission line crosses over the coupling aperture from the outside of the cavity to the inside. As a result the two coupling apertures realize opposite polarities of coupling.

However, in the configuration of Fig A.4, the two coupling apertures are located on same relative sides of their respective cavities. In both cavities, the transmission line crosses over the coupling aperture from the outside of the cavity to the inside, and thus both cavities have the same sign of external coupling. This is reflected in the orientation of the electric fields, which both have the same polarity.

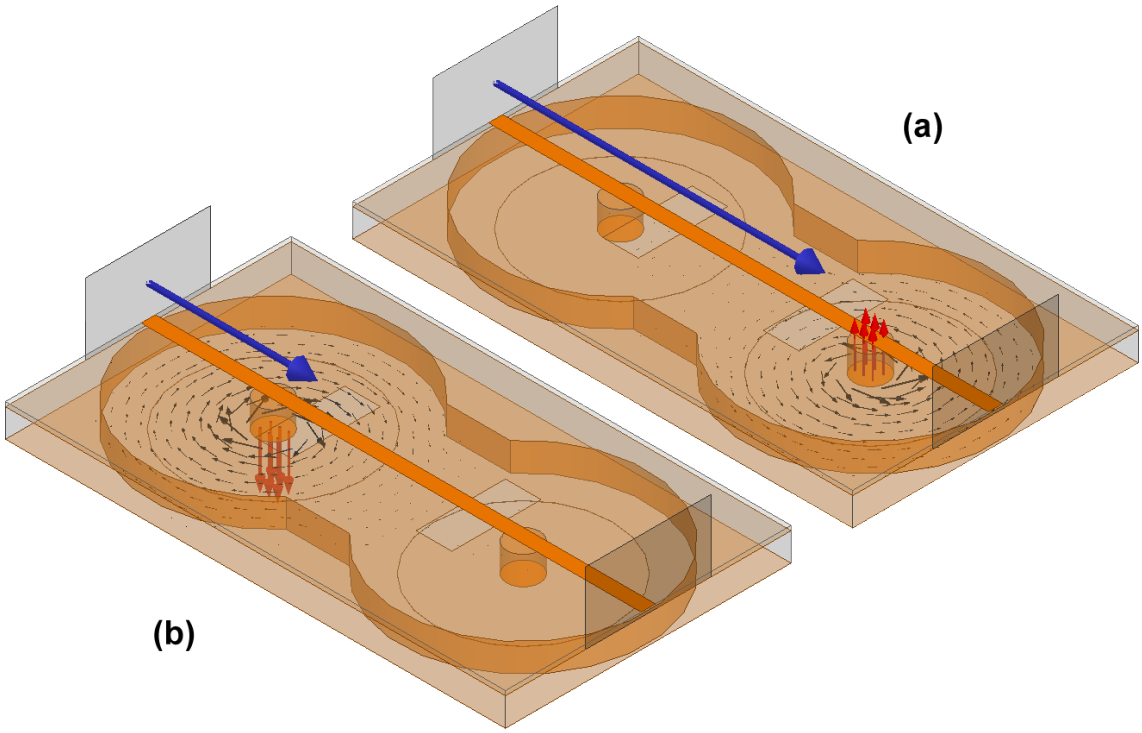

Fig A.3. An external coupling scheme for a two-pole evanescent-mode filter in which the two external coupling elements have opposite polarities.

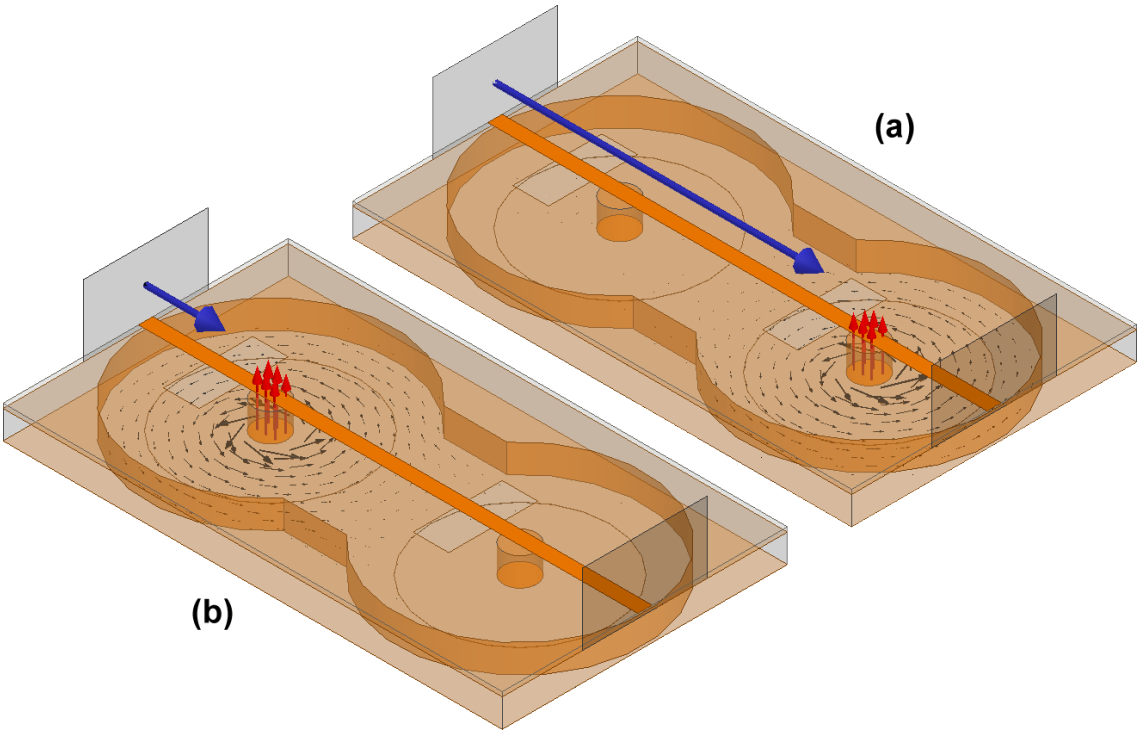

Fig A.4. An external coupling scheme for a two-pole evanescent-mode filter in which the two external coupling elements have the same polarity.

As another demonstration, a filter utilizing edge-coupled λ/4 microstrip resonators is shown in Fig A.5. Similar to the previous example, the resonators are excited separately by shorting out one resonator at a time, and deembedding the excitation to a phase of 0^o at the live resonator's coupling reference plane. The two resonators have opposite electric field polarities under identical excitations, again showing that the two external coupling elements have opposite signs.

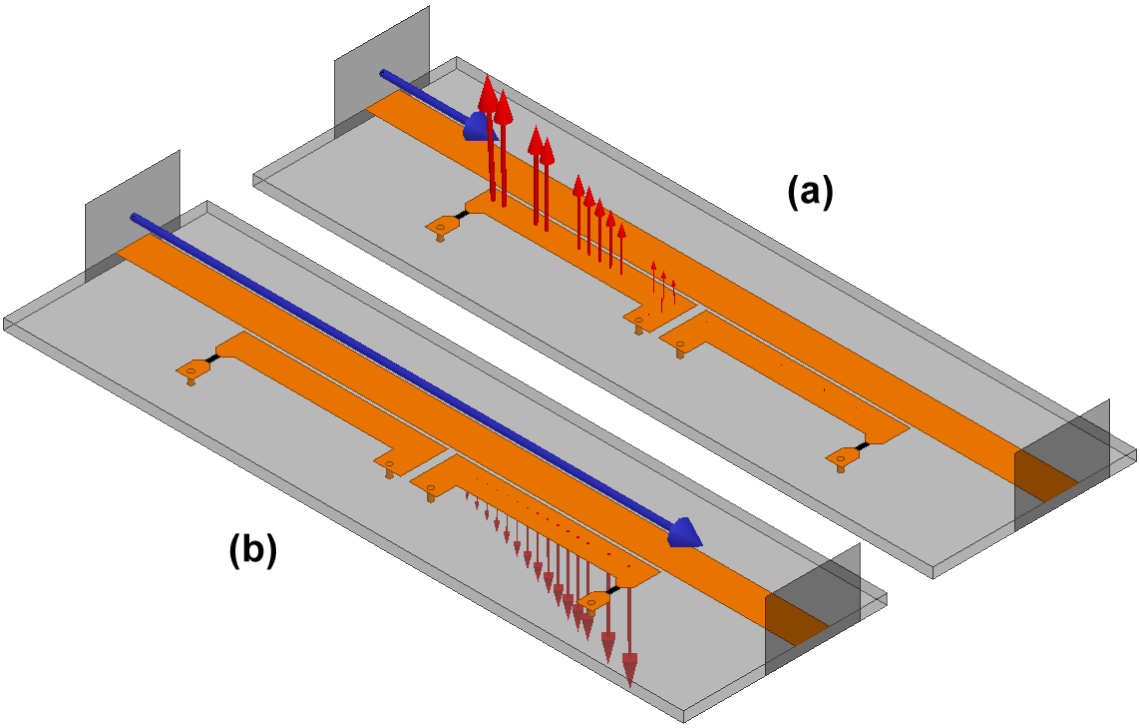

Fig A.5. An external coupling scheme for a two-pole λ/4 microstrip filter in which the two external coupling elements have opposite polarities.

A.3 Interresonator Coupling

When designing filters with cross-coupling, it is important to know the relative polarity of the interresonator coupling. For example, when designing a cross-coupled filter with transmission zeroes, a coupling with opposite polarity with respect to the rest of the coupling must be negative. Conversely, when designed a self-equalized filter with improved group-delay flatness, all of the couplings must be the same sign. It is also important to know the sign of the coupling coefficient when designing absorptive bandstop filters, as the required length of source-load transmission line depends on the sign of the interresonator coupling. In some simple cases, such as in filters implemented with lumped elements, the sign of the coupling can be analytically determined. For other technologies, such as microstrip resonators or 3-D cavities, full-wave EM simulations often must be performed in order to evaluate the sign of the coupling. This often proves difficult, however, as the coupling reference plane must be known in order to properly deembed the simulation results and accurately evaluate the phase of the coupling

structure. In the following analysis, a simple method for determining the polarity of interresonator coupling through eigenmode simulations will be proposed. It will be shown that the coupling polarity can be determined by examining the polarity of the resonator voltages for the two eigenfrequencies of a coupled resonator pair.

Consider the circuit of Fig A.6:

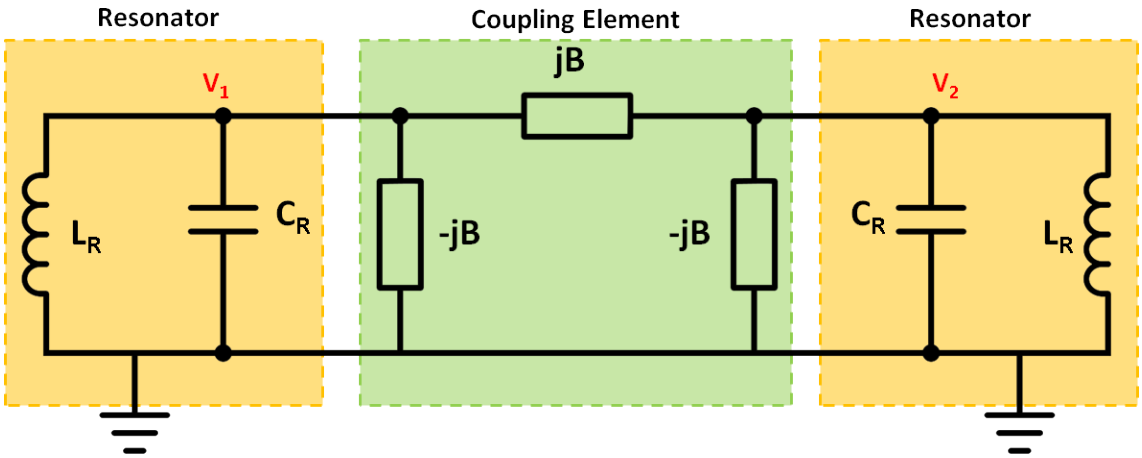

Fig A.6. Circuit diagram of two parallel L-C resonators coupled to each other with an admittance inverter, which can represent either positive or negative interresonator coupling.

It consists of two identical (and synchronously tuned) resonators coupled by an admittance inverter whose value is J = B, represented with a pi-network equivalent circuit. This inverter can be implemented as a T-network, with identical results. This can represent either capacitive (B = ωC_{coup}) or inductive (B = -1/ωL_{coup}) coupling. It can be shown that if B < 0, the admittance inverter provides a -90° phase shift, while it provides a +90° phase shift if B > 0. The resonator node voltages are designated as V_1 and V_2. Performing nodal analysis, the relationship between V_1 and V_2 can be determined:

$$V_2 = V_1 \frac{jB}{\frac{1}{j\omega L_R} + j\omega C_R} = V_1 \frac{\omega L_R B}{\omega^2 L_R C_R - 1}. \qquad \text{(A.12)}$$

We will investigate the case in which $B = -\frac{1}{\omega L_{coup}}$, representing an inductive admittance inverter which provides a -90° insertion phase if $L_{coup} > 0$ and a +90° phase shift if $L_{coup} < 0$.

Substituting $B = -\frac{1}{\omega L_{coup}}$ into (A.1) yields:

$$V_2 = V_1 \frac{L_R}{L_{coup}(1-\omega^2 L_R C_R)}. \quad \text{(A.13)}$$

The two eigenfrequencies of the circuit of Fig A.6 under the condition $B = -\frac{1}{\omega L_{coup}}$ are well known, and can be obtained through even/odd mode analysis of the circuit to be

$$\omega_{1,2} = \sqrt{\frac{L_R \pm L_{coup}}{\pm L_R L_{coup} C_R}} = \frac{1}{\sqrt{[L_R||(\pm L_{coup})]C_R}} \quad \text{(A.14)}$$

Evaluating (A.2) at the frequencies listed in (A.3) yields:

$V_2 = -V_1$ when $\omega = \frac{1}{\sqrt{[L_R||L_{coup}]C_R}}$. (A.15)

$V_2 = +V_1$ when $\omega = \frac{1}{\sqrt{[L_R||(-L_{coup})]C_R}}$. (A.16)

With a positive mutual inductance (that is $B = -\frac{1}{\omega L_{coup}}$, and L_{coup} is positive), the eigenfrequency of (A.5) is lower than that of (A.4). If L_{coup} is negative, the eigenfrequency of (A.4) is the lower of the two eigenfrequencies but the voltage polarities stated in (A.4) and (A.5) remain the same. From this we can conclude that when the interresonator coupling element provides a -90^o phase shift (usually considered to be negative coupling), the resonator voltages have the same polarity at the lower eigenmode frequency. Conversely, when the coupling element provides a +90^o phase shift (positive coupling), the resonator voltages have opposite polarity at the lower eigenmode frequency. Thus we can determine the polarity of a given interresonator coupling structure by performing an eigenmode simulation of the coupled resonator structure and observing the relative polarity of the resonator voltages at the lower eigenfrequency.

To demonstrate this concept further, eigenmode simulations of two coupled resonator structures have been performed. The first structure consists of two evanescent-mode cavity resonators coupled together with an inductive iris, as shown in Fig A.7. The coupling iris can be modeled as an inductive Pi-network [123] which corresponds to the configuration of Fig A.6, with $L_{coup} > 0$. This Pi-network provides a -90^o phase shift, which results in negative coupling. Thus the resonator voltages should have the same polarity at the lower eigenfrequency, as stated in section A.3. The electric and magnetic

fields corresponding to the lower eigenfrequency, obtained using Ansys HFSS eigenmode simulator, are shown in Fig A.7(a). It is clear that as predicted, both resonators have voltages of the same polarity.

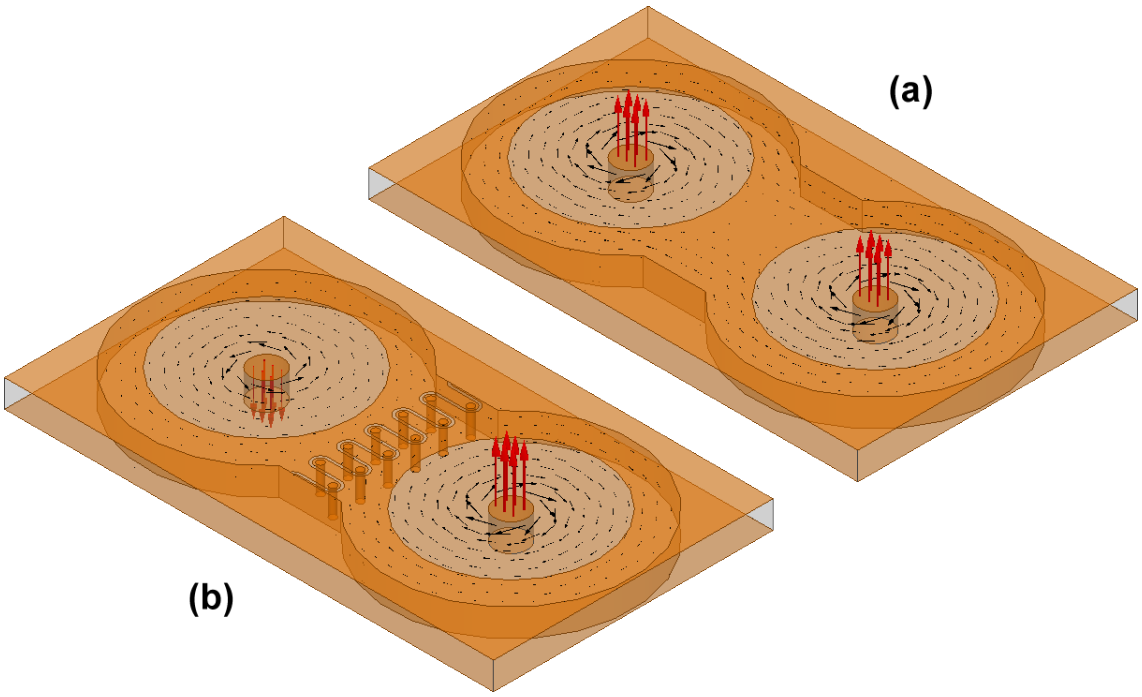

Fig A.7. Electric and magnetic fields at the lower eigenfrequency for two types of interresonator coupling in evanescent-mode cavity resonators. (a) The standard method of interresonator coupling. The inductive coupling iris provides negative coupling, and thus the resonator voltages have the same polarity. (b) An alternative coupling topology which produces positive coupling, and thus the resonator voltages have opposite polarity.

In [108], a new interresonator coupling structure which realizes positive coupling was introduced. The structure (shown in Fig A.7(b)) consists of the same coupling iris as Fig A.7(a), with the addition of an array of vias which connect the top of the coupling iris to the bottom and a meandered slot cut into the top of the coupling iris between the vias. This slot blocks the flow of current along the top of the coupling iris, and instead routes it through the vias to the bottom of the iris. This effectively reverses the flow of current in the coupling section, which reverses the polarity of the coupling. The electric and magnetic fields corresponding to the lower eigenfrequency of this coupling structure are

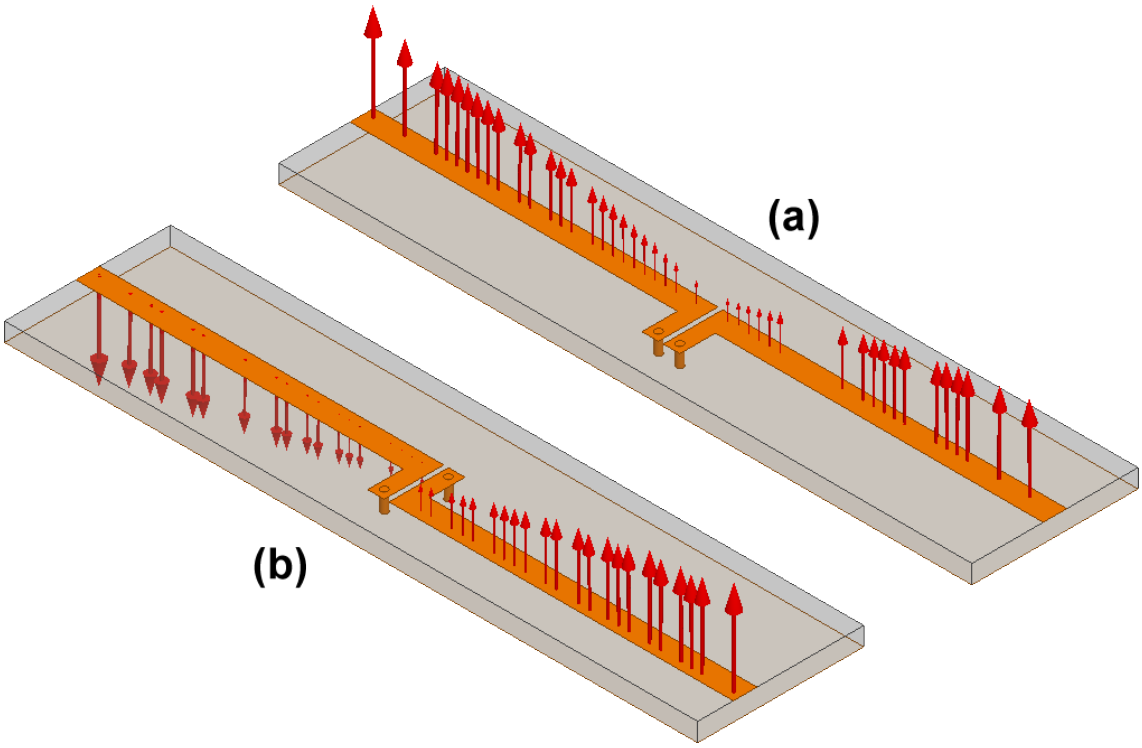

Fig A.8. Electric field distribution for two configurations of coupled λ/4 microstrip resonators at their lower eigenfrequencies. (a) The resonator voltages have the same polarity, and thus this configuration provides negative interresonator coupling. (b) The resonator voltages have the opposite polarity, and thus this configuration provides positive interresonator coupling.

shown in Fig A.7(b). It can be seen that in this case, the resonator voltages have opposite polarity, which corresponds to positive coupling as explained in section A.3

The second coupled resonator structure investigated is shown in Fig A.8(a). It consists of two quarter-wave microstrip resonators, each grounded on one end with a via. The grounded ends of the microstrip lines are placed close to each other, creating interresonator coupling which is primarily magnetic in nature. In the configuration of Fig A.8(a), where the resonators' grounding vias are symmetrically oriented, the mutual inductance between the resonators is positive. This provides a -90^{o} phase shift, which corresponds to negative interresonator coupling. This is reflected in the relative polarity of the electric fields of the two resonators, which as expected have the same polarity at the lower eigenfrequency.

If the orientation of the vias in the coupling section is reversed, as shown in Fig A.8(b), then there is effectively a negative mutual inductance between the resonators.

This results in positive coupling, and as a result the resonator voltages have opposite polarity at the lower eigenfrequency.

B. Non-Magnetic Non-Reciprocal Devices

Non-reciprocal devices, such as circulators and isolators, are very common components in microwave systems. They are often used as isolators to shield amplifiers from highly-reflective loads such as additional amplifier stages or detuned antennas, and as multiplexers to combine transmitters and receivers onto the same antenna. One such application is duplexing transmitter and receiver onto the same antenna is that of single-channel, full-duplex transceivers, as described in [124]. This design, which is designed to be able to both transmit and receive simultaneously at the same center frequency, uses a circulator to combine the transmitter and receiver onto the same antenna, while providing a small amount (around 15 dB) of isolation between transmitter and receiver. An analog signal cancellation circuit is then used to achieve an additional ~90 dB of isolation between transmitter and receiver, allowing the radio to receive weak (-100 dBm) signals while simultaneously transmitting strong (+20 dB) signals.

Circulators and isolators typically achieve their non-reciprocity through the use of magnetically-biased ferrite materials. These materials are often bulky, preventing them from being integrated on-chip into integrated circuits, and can be very expensive due to the manual fine-tuning that is often required to manufacture them. Their isolation is also limited, usually no greater than 20 to 30 dB. Because of these limitations, there has been a great deal of research interest in developing non-ferrite-based circulators and isolators. Non-linear and non-reciprocal semiconductor devices such as transistors have been used to realize non-ferrite circulators and isolators [125]. These devices can easily be integrated on-chip due to the small-size and ease of integration of modern microwave transistors. However, they suffer from severe non-linearities and high levels of noise which are both inherent to semiconductor devices. Other approaches have exploited nonlinear optical effects to achieve nonreciprocity [126]–[128], but these require the

complexities associated with converting microwave signals to/from the optical domain, and also suffer from non-linearities. Yet another recently proposed idea uses time-varying transmission lines, whose characteristic impedance is modulated by a low-frequency travelling wave [129]–[131]. This approach achieves very wide bandwidths (up to two octaves), but suffers from limited isolation (< 20 dB) and is physically large, as it is several wavelengths long.

As an alternative to these methods, a promising non-magnetic circulator based on parametrically-modulated coupled resonators was recently presented in [132], [133]. A schematic diagram of the circulator in [132] is shown in Fig B.1, consisting of three resonators, each of which is coupled to each other. The resonant frequency of each resonator is modulated at a frequency much lower than the RF frequency, with a phase progression of 120^{o} applied to each successive resonator. The result is a narrowband circulator which achieves good amounts of isolation (up to 60 dB) between isolated ports. Though the results demonstrated in [132], [133] have a number of drawbacks (namely, high levels of insertion loss), the concept is promising and warrants further investigation.

As preliminary work, the device in [132] has been replicated at a higher frequency, and several two-port non-reciprocal filters of varying order and bandwidth have been designed and simulated. Fig B.1 shows both the conceptual diagram and the schematic of the replicated circulator. The resonators' capacitors are represented as equation-based devices in Keysight ADS, and their capacitance is controlled by a sinusoidal voltage source. Harmonic balance simulations allow the circuit to be simulated. It is found that by varying the value of the coupling capacitors, the bandwidth of the circulator changes. As bandwidth is increased, however, insertion loss increases because a stronger capacitance modulation is required and more of the RF signal is converted to different frequencies.

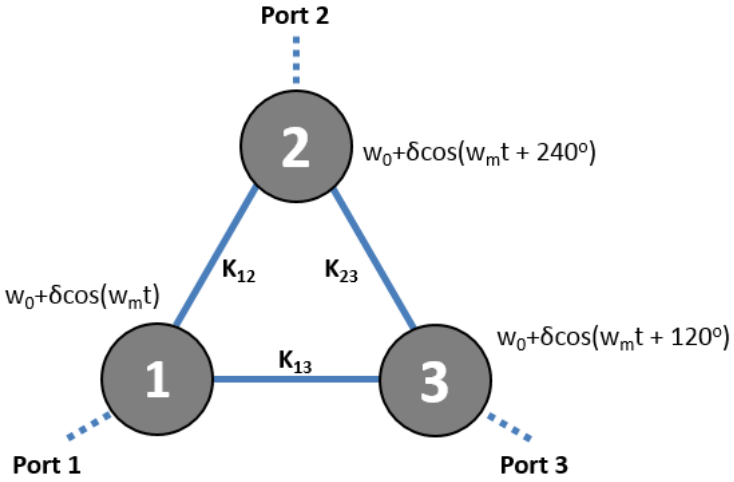

Fig B.1. Conceptual diagram of the non-magnetic circulator presented in [132].

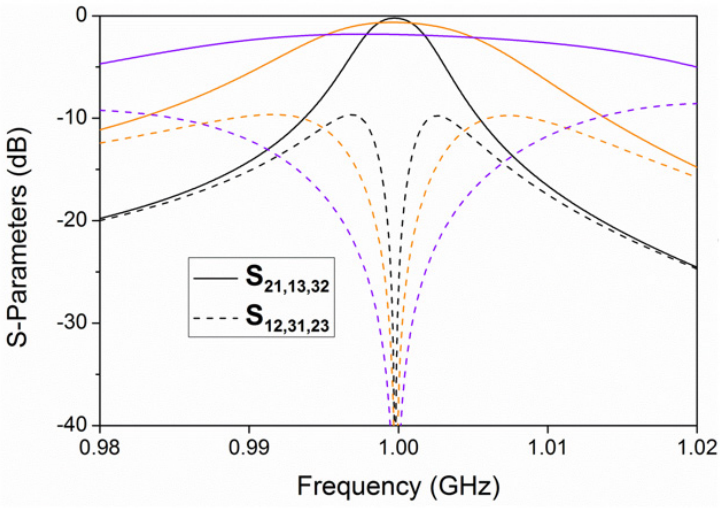

Fig B.2. Simulated performance of the circuit in Fig B.1 for different bandwidths.

Fig B.3 shows conceptual diagrams for two 4-pole non-reciprocal filters which have different bandwidths, as dictated by their coupling values.

Resonators are implemented as lossless parallel LC resonators, and coupling elements are implemented as ideal admittance inverters. It can be seen that different transfer functions can be realized with different bandwidths and different transmission and isolation characteristics.

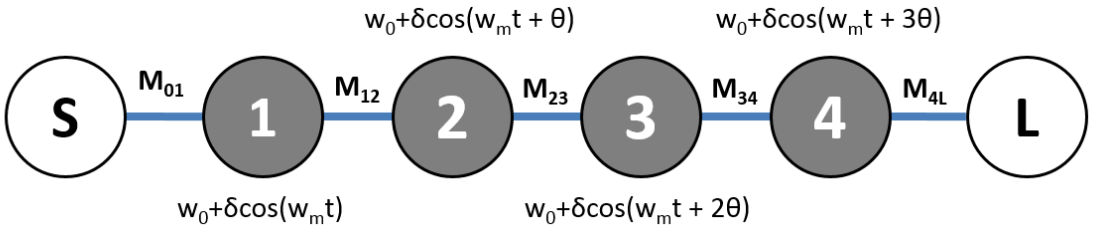

Fig B.3. A diagram of a 4-pole non-reciprocal filter.

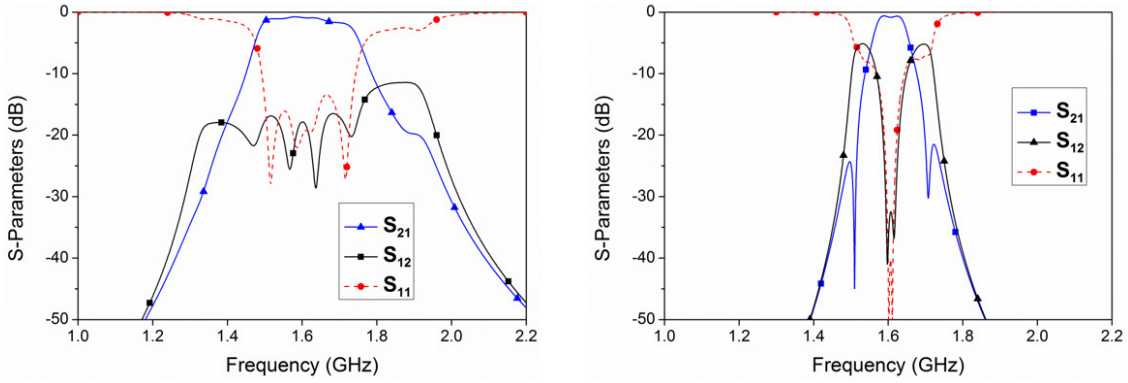

Fig B.4. Simulated performance of two different instances of the 4-pole filter of Fig B.3

For example, the first filter has a 15% 3-dB fractional bandwidth, and achieves greater than 10 dB of reverse isolation (S_{12}) over the entire passband, making the usable bandwidth of this filter/isolator 15%. The second filter, however, has a much narrower 3-dB bandwidth of approximately 3%, providing nearly 30 dB of isolation over the passband. Filters / isolators such as these, if combined into 3-port circulators, have the potential to not only replace circulators as power combiners in full-duplex receivers, but also to replace the RF filters in such systems due to their highly-selective frequency responses.

In order to fully explore the potential of this new class of non-reciprocal filter, a number of key questions must be answered.

- Can low insertion loss be achieved? It appears that there are multiple factors competing against each other with regard to insertion loss. It is well-known that a filter's insertion loss increases as its bandwidth decreases. However, simulations of the circuit in Fig B.1 show that as the bandwidth of the non-

reciprocal filter is increased, its insertion loss increases as well even with lossless resonators (Fig B.2). This is because as the bandwidth is increased, the resonators' frequencies must be modulated more heavily, which increases intermodulation products and actually converts significant amounts of signal power from the fundamental frequency to the sidebands which result from intermodulation. Thus in order to achieve low insertion loss, resonators with high quality factors must be utilized. This, however, introduces another question:

- Can this concept be implemented with high quality-factor resonators? In [132], [133], the resonators utilized were either lumped-element or microstrip resonators tuned by varactor diodes. These types of resonators are well-suited to this application because varactor diodes can be tuned very quickly, and thus can be modulated at the high frequencies required for this application (15 MHz in [132]). Even higher modulation frequencies will be required in order to scale this design up to higher frequencies of interest. For example, the design in [133] centered at 2.2 GHz requires the resonators to be modulated at 400 MHz. However, varactor diodes have relatively low quality factors ($Q < 100$), and thus are unable to realize circulators with low levels of insertion loss. The measured circulator presented in [133] has roughly 10 dB of insertion loss, for a center frequency of 130 MHz.

  It is clear that resonators with high quality factors must be used, but existing high-Q tunable resonators have much lower tuning speeds than those required for this application. Evanescent-mode cavity resonators are widely-tunable and have high quality factors, but their tunings speeds are usually on the order to 10's of microseconds to milliseconds [54], and thus cannot be modulated at MHz frequencies, as required. Other high-Q tunable resonators technologies, such as YIG resonators, have similar tuning speeds. Thus, in order to realize circulators of this type, a new type of tunable resonator which has a high unloaded quality factor but very fast tuning speed (< 100 ns) needs to be developed.

- Can the intermodulation products which result from the modulation of the resonators be reduced? All nonlinear circuits produce intermodulation distortion when excited with more than one signal. However, because the resonators in this circulator are being modulated, relatively large intermodulation terms will be generated even with a single-tone input. In [133], the output spectrum of their proposed circulator for a single-tone input is shown. The circulator achieves high levels (~ 55 dB) of non-reciprocity at its center frequency, but the intermodulation products created by the resonator modulation are orders of magnitude (30-40 dB) larger than the non-reciprocal attenuation, and thus they will spoil the performance of the circulator unless they are reduced or filtered out.

VITA

VITA

Mark Hickle received the B.S.E.E degree from Missouri University of Science and Technology, Rolla, MO, in 2012, and is currently working toward the Ph.D. degree in electrical and computer engineering at Purdue University under the direction of Prof. Dimitrios Peroulis.

He is a National Defense Science and Engineering Graduate (NDSEG) Fellow. His current research interests are in synthesis and fabrication techniques for highly-reconfigurable microwave and millimeter-wave filters.

Mr. Hickle is the past president of Purdue University's IEEE MTT-S student chapter. He was the recipient of the 1st place awards in the RF-MEMS Tunable Filter student design competitions at both the 2014 and 2015 International Microwave Symposiums, and was also the recipient of the 1st place award for the 2015 MTT-S Youtube/YouKu video competition.